

Louis-David Lord

Hertford College, University of Oxford

D.Phil Thesis

Department of Psychiatry

Supervisors

Prof. Morten Kringelbach

Prof. Renaud Lambiotte

Integration and Segregation in Whole-Brain Networks: Implications for Altered States of Consciousness

This thesis is submitted to the Department of Psychiatry, University of Oxford, in partial fulfilment of the requirements for the degree of Doctor of Philosophy

Trinity Term 2018

Abstract

Integration and Segregation in Whole-Brain Networks: Implications for Altered States of Consciousness

Louis-David Lord

Hertford College

To survive in an ever-changing environment, the brain must seamlessly integrate a rich stream of incoming information into coherent internal representations that can then be used to efficiently plan for action. The brain must also balance its ability to *integrate* information with a complementary capacity to *segregate* information into modules which perform specialized computations in local circuits.

The central focus of this Thesis is to investigate the *dynamical* properties of the integration/segregation balance in functional MRI data collected in two distinct altered states of consciousness: slow-wave sleep, and a psychedelic experience induced by intravenously administering psilocybin; the psychoactive compound in "magic mushrooms".

In Chapter 2, I implement a novel method for identifying highly integrative nodes in human brain networks from the persistent homology of fMRI data, as a complement to standard graph theoretical methods. I report that topologically central nodes in the 'persistence homological scaffold' have a combination of high betweenness-centrality and high participation coefficient, whilst simultaneously avoiding densely connected neighborhood clusters.

In Chapter 3, I investigate dynamical changes in global measures of functional integration and segregation derived from fMRI data. Synchrony, metastability and chimeraness metrics are computed separately in slow-wave sleep and in the psychedelic state. It is found that global synchrony and metastability are reduced in slow-wave sleep relative to a wakeful rest baseline, whilst chimeraness is increased. Diametrically opposite effects on each measure are observed in the psychedelic state.

Chapter 4 characterizes the brain's dynamical landscape from a system-level perspective under psilocybin by computing the fractional occupancy and transition probabilities of specific functional network states over time. An increase in the probability of occurrence of a globally coherent functional connectivity state is observed, alongside a strong decrease in the fractional occupancy of a fronto-parietal control network.

In Chapter 5, I further characterize the capacity of brain areas to dynamically broadcast regional activity signals locally or globally in both deep sleep and the psychedelic state. The results notably show that intrinsic activity perturbations in a given brain area are more likely to propagate strictly locally in slow-wave sleep than during wakeful rest. In the psychedelic state, the size of integration cascades elicited by local perturbations over time is significantly more variable than during the baseline scan.

The experimental findings presented in this Thesis indicate that alterations in consciousness level and/or contents are accompanied by temporally-dependent changes in the brain's integration and segregation balance, promoting cross-modular integration in the psychedelic state, and functionally segregated brain dynamics in slow-wave sleep.

This thesis is submitted for the degree of Doctor of Philosophy at the University of Oxford.
Trinity Term 2018

Acknowledgments

I first thank my parents whose support and understanding has been at the very root of the academic success that has led me to pursuing a doctorate at Oxford in the first place, and ultimately to the completion of this exciting and challenging research programme. I am forever grateful; and hope that my actions both within and beyond science will continue to make them proud.

My D.Phil project and overall educational experience in Oxford would of course never have materialized without my primary supervisor, Prof. Morten Kringelbach. Morten's passion for science, scientific skillset, ambition and versatility have been truly inspiring. Prof. Kringelbach has enabled me to explore the scientific questions that I found most fascinating, however methodologically or conceptually challenging, and I will look back very fondly on my doctoral training under his guidance. I also thank my co-supervisor, Prof. Renaud Lambiotte, for taking me on as a student shortly after joining Oxford as a Faculty member during my final year. I always left my meetings with Renaud with a blend of clarity, confidence in the mathematical soundness of my methods, stimulating ideas and a renewed enthusiasm towards my research, for which I am grateful.

Special thanks to my close collaborator Dr. Paul Expert whose remarkable scientific knowledge, insight and methodological rigor was pivotal to the completion of this thesis. Drs. Joana Cabral and Robin Carhart-Harris' contributions in the form of analytical tools, unique datasets and, most importantly ideas and perspectives have also been instrumental towards this sequence of studies. The state-of-the-art methodological tools provided to me by Prof. Gustavo Deco and his confidence in me to contribute an Invited Review to an excellent journal were also formative and appreciated. The continued support and guidance of Prof. Federico Turkheimer has also been instrumental to my scientific training, and I thank him for continuing to involve me on interesting and impactful theoretical papers throughout my doctorate.

I also thank all current and former members of the Hedonia Lab, including our many visitors over the years, for creating a positive and supportive environment conducive to lively discussions and scientific excellence. Special thanks to my labmates Marina Charquero-Ballester and Dr. Henrique Fernandes for their friendship and support during both the good and challenging times. I also acknowledge Dr. Angus Stevner's guidance and insights, especially in the final stages of my D.Phil.

I also wish to thank Hertford College, where I had the opportunity to migrate in my second year of study to take up the Mann Senior Scholarship. The generous grant, housing privileges and dining rights tied to this award have truly helped me enjoy Oxford to the fullest. Yet the best part about joining Hertford College was to become an active member of its Middle Common Room where I have met several exceptional individuals that I am fortunate to now call friends. To all my MCR friends and especially: Liisa, Fabrizio, Andrew, Kamille, Georgia, Rory, Kaja, Maj, Joey, Luiza, Emma, Alex, Jonny, Antonis and Mark; thank you for the amazing times we have had together, and those still to come! I also thank Senior Common Room members: Prof Martin Maiden, Prof Michael Wooldridge, Prof Fernando Alday, Prof Peter Millican, Prof Simon Brewster, Sir Martin Donnelly, Dr. Andrew Cropper, Dr. Andre Nilsen, Dr. Sam Henry and Dr. Clive Hambler for the stimulating high-table dinner discussions and for always making me and my guests feel at home at SCR events.

I finally acknowledge my sponsors: the Canadian Institutes of Health Research, Canadian Centennial Scholarship Fund, Hertford College, and the European Research Council (via Prof. Kringelbach). Thank you for believing in me and my research, and making my D.Phil studies at the University of Oxford possible.

Contents

Chapter 1: Introduction 1
1.1 Integration and Segregation in the Human Brain 1
1.1.1 Small-world brain networks: a blueprint for integration and segregation 1
1.1.2 Dynamical Integration & Segregation 5
1.1.3 Neurobiological determinants of the integration / segregation balance 7
1.2 Theoretical Accounts of Consciousness 14
1.2.1 Dynamic Core Theory 14
1.2.2 Information Integration Theory 16
1.2.3 Perturbational Complexity Index 18
1.3 Psychopharmacology and Neuroimaging of Psilocybin 21
1.3.1 History, Phenomenology & Pharmacological properties 21
1.3.2 Neuroimaging studies of psilocybin 23
1.4 Sleep Stages, Mechanisms and Neuroimaging 28
1.4.1 Neuroscience of Sleep: A brief Overview 28
1.4.2 Neuroimaging investigations of Slow-Wave Sleep 30
1.5 Summary of the Argument 35
Chapter 2: Regional contributions to global integration: novel insights from the homological scaffolds of functional connectivity networks 38
2.1 Introduction 38
2.2 Methods 40
Study Participants 40
2.2.1 Persistent Homology and Scaffolds 41
2.2.2 Graph Theoretical Analysis 44
2.2.3 Definition of *Persistence Scaffold Strength* and Functional Hubs 46
2.3 Results 47
2.3.1 Relationship between nodal PSS and standard graph metrics 47
2.3.2 Identification of functional hubs 50
2.4 Discussion 52
2.5 Chapter Summary 56
Chapter 3: Global Brain Dynamics in Altered States of Consciousness 57
3.1 Introduction 57
3.2 Methods 58
3.2.1 Participants 58
3.2.2 Experimental protocol 59
3.2.3 Neuroimaging data acquisition & processing 59
3.2.4 Dynamical functional connectivity analysis 61
3.2.5 Order Parameter, Synchrony and Metastability 62
3.2.6 Chimeraness Index 63
3.3 Results 64

3.3.1 Whole-Brain Synchrony and Metastability 64
3.3.2 Chimeraness Index 65
3.4 Discussion 66
3.5 Chapter Summary 70
Chapter 4: Altered Trajectories in the Dynamical Repertoire of Functional Network States under Psilocybin 72
4.1 Introduction 72
4.2 Methods 73
4.2.1 Participants, Experimental Protocol, Neuroimaging Data Acquisition & Processing 73
4.2.2 Dynamic Functional Connectivity Analysis & FC Leading Eigenvector 73
4.2.3 Identification of FC states 75
4.2.4 Probability of Occurrence and Switching Matrix of FC States 76
4.3 Results 76
4.3.1 Dynamical repertoire of FC states is altered by psilocybin 76
4.3.2 Psilocybin modulates the temporal expression of FC States 81
4.3.3 State-to-State switching profiles are significantly different under psilocybin 83
4.4 Discussion 85
4.5 Chapter Summary 88
Chapter 5: Local vs Global Integration in Altered States of Consciousness: System-wide consequences of intrinsic perturbations 89
5.1 Introduction 89
5.2 Methods 90
5.2.1 Participants, Experimental Protocol, Data Acquisition & Processing 90
5.2.2 Integration-Driven Integration and Variability 90
5.2.3 Surrogate Analysis 91
5.2.4 Between-Condition comparisons 92
5.3 Results 93
5.3.1 Psilocybin Study 93
5.3.2 Sleep Study 95
5.4 Discussion 96
5.5 Chapter Summary 100
Chapter 6: Conclusion 102
6.1 Original Contributions 102
6.2 Perspectives 105
References 109
Supplementary Materials 117

List of Figures

Figure 1.1. Investigating human brain connectivity with neuroimaging and graph theory..... 3
Figure 1.2. Measuring spatiotemporal integration and segregation 7
Figure 1.3. Overview of whole-brain computational modelling 9
Figure 1.4. Influences of brain structural connectivity on integration and segregation 11
Figure 1.5. Influences of the E/I balance on integration and segregation 13
Figure 1.6. Schematic representation of the Dynamic Core Theory. 16
Figure 1.7. Information Integration Theory of Consciousness (IIT) 18
Figure 1.8. Perturbational Complexity Index (PCI) in wakefulness and NREM sleep 20
Figure 1.9. Phenomenology and metabolic changes following a psilocybin infusion 24
Figure 1.10. Global communication and metastability in the psychedelic state. 27
Figure 1.11. Overview of sleep stages and NREM sleep regulation 30
Figure 1.12. Functional connectivity differences between SWS and wakefulness 32
Figure 1.13. Modularity and complexity of brain activity in slow-wave sleep (SWS). 34
Figure 2.1. Illustrations of cliques, simplices, holes and clique complex. 42
Figure 2.2. Toy example illustrating the generation of the homological scaffolds 44
Figure 2.3. Comparison between Persistence Scaffold Strength and standard graph measures. 49
Figure 2.4. Normalized Metric Values 51
Figure 2.5. Graphical Display of the Highest-Ranking Nodes 52
Figure 3.1. Computing dynamical functional connectivity (dFC) matrix from fMRI data. 62
Figure 3.2. BOLD synchrony and metastability in altered states of consciousness 65
Figure 3.3. Chimeraness index estimated from fMRI data in altered states of consciousness ... 66
Figure 4.1. Variance captured by the leading eigenvector in LEiDA analysis 75
Figure 4.2. Significant differences in FC state probability as a function of k. 77
Figure 4.3. Dynamical exploration of the repertoire of FC states altered by psilocybin 78
Figure 4.4. Probability of occurrence of FC states under psilocybin 80
Figure 4.5. 3D embedding of FC patterns 81
Figure 4.6. Psilocybin modulates the temporal expression of FC States 82
Figure 4.7. Psilocybin modifies the switching patterns between FC-states 84
Figure 5.1. Representations of ignition events from the binarization of BOLD signals 91
Figure 5.2. Schematic of the intrinsic-driven-integration (IDI) calculation 92
Figure 5.3. Global and Regional IDI & IDI-variability: Psilocybin study. 94
Figure 5.4. Nodes showing significant increases in IDI-variability under psilocybin. 95
Figure 5.5. Global and Regional IDI and IDI-variability results: Sleep study. 96
Figure 6.1. Conceptual schematic of the brain's dynamical landscape 106

Chapter 1: Introduction

1.1 Integration and Segregation in the Human Brain [1]

1.1.1 Small-world brain networks: a blueprint for integration and segregation

In order to promote survival, the brain must be capable of integrating a wide range of incoming stimuli from its environment and seamlessly 'bind' this complex stream of information into meaningful internal representations that are then used to plan for the next action. For example, a tennis player attempting to return his opponent's serve must quickly integrate visual and auditory stimuli from the tennis court (e.g. the positioning of the opponent, the racket and the incoming ball), together with proprioceptive information from the body in order to initiate the appropriate motor responses to hit a successful return. While a capacity for functional integration is undeniably important, the brain must also be able to segregate information into distinct modules, which perform specialized local computations (e.g. for individual sensory modalities). An extreme yet relevant example of excessive integration would be an epileptic seizure, where an abnormally large number of brain areas begin to fire in synchrony and the brain as a system becomes no longer capable of processing information in a meaningful way. There has recently been much interest in understanding which organizational features and brain mechanisms enable the efficient integration and segregation of information, and the emerging evidence suggests that a complex synergy between both structural and functional determinants are likely to be involved, as discussed further below (Lord, Stevner et al. 2017).

In recent years, novel measures of the brain's functional organization have emphasized the importance of temporal coding and coordinated neuronal oscillations in distributed networks. This has represented an important paradigm shift from the study of individual brain regions in isolation. While structural brain networks summarize the pattern of anatomical connections between region pairs making up the network nodes, functional brain networks are derived from estimates of statistical dependencies between inter-regional activity signals over time, typically averaged over long recording intervals (i.e. minutes). Investigations of large-scale structural and functional networks derived from neuroimaging data have revealed valuable insights about the topological organization of the human brain

[1] Some of the materials presented in this section were published in: *Lord LD, Stevner AB, Deco G, Kringelbach ML. Understanding principles of integration and segregation using whole-brain computational connectomics: implications for neuropsychiatric disorders. Phil. Trans. R. Soc. A. 2017 Jun 28;375(2096):20160283.*

in health and disease (Bullmore and Sporns 2009, Fornito, Zalesky et al. 2015). It has notably been established that both structural and functional networks in the human brain exhibit 'small-world' character (Watts and Strogatz 1998, Bassett and Bullmore 2006, Fornito, Zalesky et al. 2015). *Small-worldness* is a concept borrowed from a branch of mathematics called graph theory, which studies the mathematical structures used to model pairwise relations between large sets of interacting objects, also known as 'graphs'. As such, small-world networks are found not only in the brain, but in a vast range of complex systems across the biological, physical and social sciences (Watts and Strogatz 1998).

At the mesoscopic level, a key feature of small-world networks is the existence of 'modules' (also known as communities): sub-networks of densely interconnected nodes only sparsely connected to the rest of the network. While communities in structural networks tend to be spatially compact it should be noted that, in the case of functional brain networks, the belonging of a set of nodes to the same community does not necessarily imply anatomical proximity between them. Another defining feature of small-world networks is the presence of long-range, cross-modular connections, which enable the efficient routing of information between modules by minimizing both connection distances and wiring costs (Bullmore and Sporns 2012, Clune, Mouret et al. 2013). Other notable advantages of a small-world architecture include conferring resilience to the system by buffering the effects of randomly introduced perturbations, as well as enabling richer patterns of distribution of information than non-modular systems of equivalent size (Newman 2000, Yamaguti and Tsuda 2015, Sporns and Betzel 2016).

At the local level, graph theory also enables the characterization of individual nodes and of their contributions to the network's organization. For example, a special class of nodes commonly referred to as 'connector hubs' plays a particularly important role towards integrating information across the system by accessing different modules and coordinating their activity in both resting and task states (Sporns 2013, Bertolero, Yeo et al. 2015, Sporns and Betzel 2016). Such nodes are typically characterized by a combination of standard local graph metrics including high *degree-centrality* (i.e. total number of connections) as well as elevated scores on the *betweenness-centrality* and *participation coefficients* measures. These standard local graph metrics, respectively, reflect the tendency of a node to be involved in a high proportion of the shortest topological paths between other node pairs in the network, and of a given node's tendency to form connections to network communities other than its own. Connector nodes have indeed been postulated to enable the modules to maintain their

functional autonomy in the presence of increased processing demands on the whole system (Bertolero, Yeo et al. 2015). Conversely, 'provincial' hubs may also have high *degree-centrality*, but will link together nodes within the same module and thus have low *betweenness-centrality* and *participation coefficients*. Other nodes will play a more peripheral role in the network topology and have relatively low scores on each of these local measures (Figure 1.1).

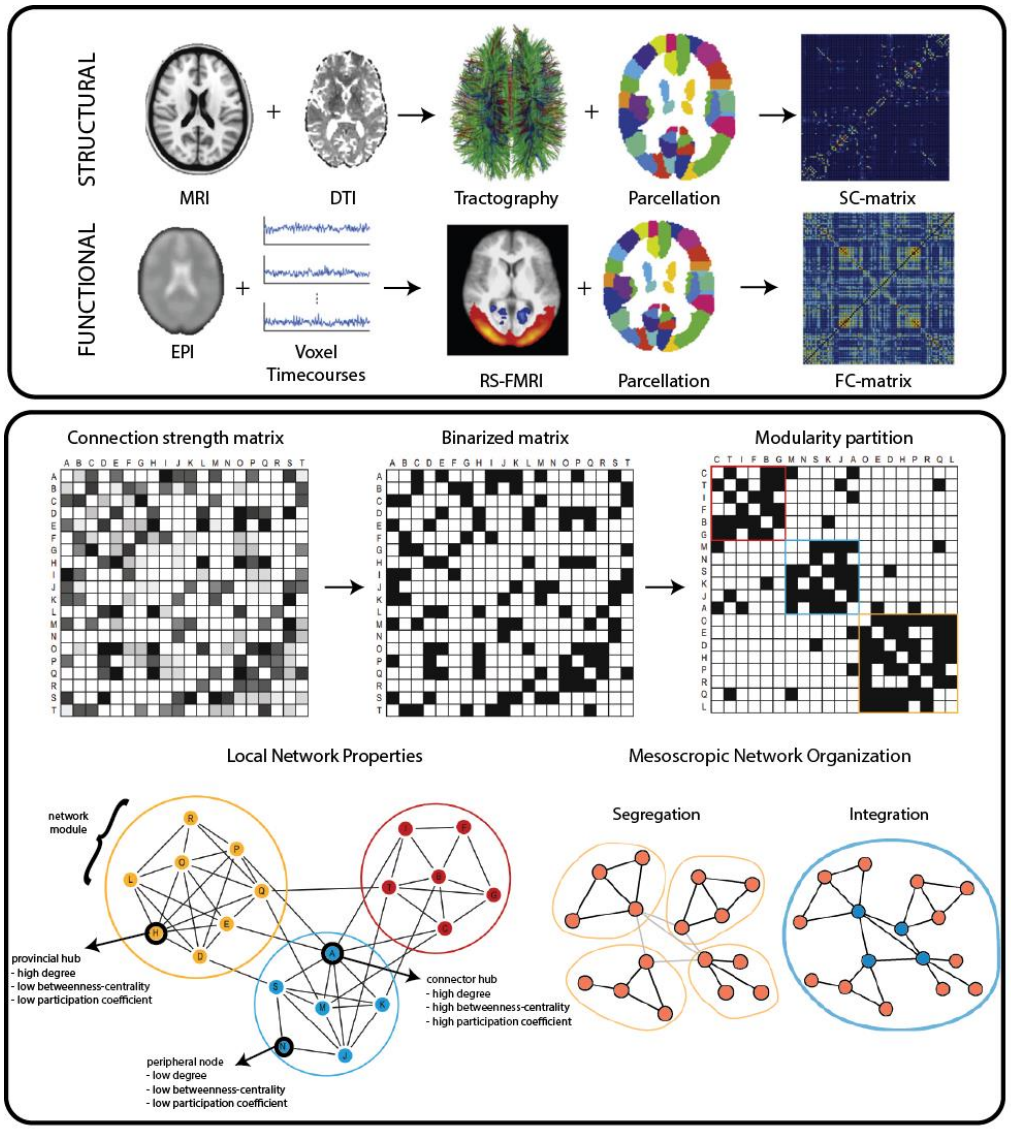


Figure 1.1. Investigating human brain connectivity with neuroimaging and graph theory. Top: *To create a structural connectivity (SC) network, MRI and DTI data are required, on which tractography analysis is then performed to uncover structural links between region pairs. These interactions are summarized in the SC matrix. To create a functional connectivity (FC) matrix, brain activity is measured; in this case using resting-state fMRI to record BOLD time courses in each voxel in the brain. This is then combined with a parcellation scheme to recreate the regional time courses for each of the regions in the parcellation. The FC matrix is then typically created from correlating inter-regional timecourses.* Bottom: *The connection strength matrices may then be thresholded to derive a binarized network representation that can in turn be used to study either the organization of brain networks. Adapted from Lord, Stevner et al. 2017.*

The initial characterization of the brain's modular organization and small-world attributes provided a promising new framework, or 'blueprint', to understand how the brain may balance the conflicting demands for the individual specialization of local sub-networks, and the long-range integration of specialized network modules, within the spatial and metabolic boundaries of the system. There are nevertheless significant limitations associated with these findings. First, some authors have argued that studies of whole-brain neuroanatomical connectivity may have underestimated the proportion of inter-areal projections, and, consequently, the cortical network density (Markov, Ercsey-Ravasz et al. 2013). These new anatomical links may have been missed notably because they link widely separated areas and tend to be sparse, therefore, requiring high imaging resolution for their detection (Vezoli, Falchier et al. 2004, Markov, Ercsey-Ravasz et al. 2013). Moreover, the study of static network representations of the brain, while undeniably informative, does not explain the spatio-temporal integration and segregation of information in the human brain at behaviorally relevant timescales. In addition, cross-sectional neuroimaging studies of functional connectivity (FC) are, by design, generally not suited to provide causal mechanistic insights into the brain's global network dynamics.

The majority of studies investigating functional brain networks conducted to date, including those presented in this Thesis, have used functional MRI (fMRI). Functional MRI is a non-invasive neuroimaging modality which *indirectly* measures neural activity by leveraging on the blood oxygen level dependent (BOLD) response. BOLD signal increases measured via magnetic resonance imaging (MRI) result from a complex cascade of physiological events leading to activity-linked local changes in the ratio of oxygenated to deoxygenated hemoglobin, which have different magnetic properties. Briefly, a local increase in neural activity leads to an increase in regional cerebral blood flow which exceeds the cerebral metabolic rate of oxygen. This overcompensation increases the oxy-to-deoxyhemoglobin ratio, which results in a higher BOLD signal (Logothetis and Wandell 2004).

The low frequency of BOLD signals (typically < 0.1Hz) from which resting-state functional connectivity networks are typically derived are therefore on a completely different temporal scale than electrophysiological recordings of brain activity collected directly from neural sources. Intracortical electrophysiological recordings in humans have shown that local BOLD signals are positively correlated with local field potentials (LFP) in the gamma-frequency range (30Hz – 100Hz) (Logothetis, Pauls et al. 2001), yet it remains

unclear whether these local relationships extend to the distributed functional connectivity networks measured with fMRI. It has notably been proposed that both very slow LFP fluctuations (i.e. sub-delta range) and slow modulations of gamma power may be plausible electrophysiological mechanisms underlying functional connectivity at the whole-brain scale (He and Raichle 2009).

BOLD time courses in each voxel in the brain are then usually combined with a parcellation scheme to extract the regional time courses for each of the areas comprised in the chosen anatomical parcellation. A range of brain parcellations developed using different methods exist for such purposes (Arslan, Ktena et al. 2018). The analyses presented in this Thesis employed the Automated Anatomical Labeling parcellation (AAL-90) which counts 90 cortical and subcortical regions (excluding cerebellum) (Tzourio-Mazoyer, Landeau et al. 2002). As its name implies, the AAL is an automated anatomical parcellation (i.e. algorithmically-driven) based on the spatially normalized single-subject high-resolution T1 volume provided by the Montreal Neurological Institute (MNI). The analysis pipeline for extracting functional connectivity networks from fMRI data is summarized graphically in the top panel of Figure 1.1.

Having now introduced the general concepts of integration and segregation in whole-brain structural and time-averaged functional networks, the remainder of the Introduction will focus on the *dynamical* aspects of the introduction/segregation balance in the human brain. I will notably discuss recent evidence from dynamical functional connectivity and whole-brain computational modelling studies highlighting the importance and neurobiological determinants of the integration/segregation balance for healthy brain functioning (Sections 1.1.2, 1.1.3) before linking these experimental findings to some influential theoretical accounts of consciousness (Section 1.2). I will then move on to describe how both time-averaged and dynamical measures of global brain activity are disrupted in altered states of consciousness, namely the psychedelic state (Section 1.3), and slow-wave sleep (Section 1.4).

1.1.2 Dynamical Integration & Segregation

Recent functional neuroimaging studies have demonstrated that the FC between brain areas is not stable over time (Calhoun, Miller et al. 2014). This can be empirically observed by considering the temporal variability of FC estimated at individual connections

(Zalesky, Fornito et al. 2014), or alternatively the transition dynamics between a small repertoire of FC patterns stable for short periods of time, known as 'FC states', which are reproducible across time and individual subjects (Allen, Damaraju et al. 2014, Baker, Brookes et al. 2014, Cabral, Vidaurre et al. 2017).

In order to flexibly integrate communication between specialized sub-networks, it has been proposed that the human brain strikes a metastable balance between the local segregation of function and the global integration of information (Varela, Lachaux et al. 2001, Kelso 2012, Deco, Tononi et al. 2015). Recent neuroimaging studies have notably considered the time-evolution of the modular organization of brain functional networks. Dynamical connectivity analyses of resting-state fMRI suggested that whole-brain functional networks alternate between periods of high and low modularity, hypothesized to represent states where segregated information processing and global integration across community boundaries, respectively, dominate the system (Betzel, Fukushima et al. 2016, Shine, Koyejo et al. 2016). Intermittent episodes of global synchronization interspersed between otherwise segregated network states might allow network elements access to a cognitive workplace needed for cognitive functioning in a metabolically efficient manner (Zalesky, Fornito et al. 2014). This is supported by observations at the local level where a "dynamic cartographic analysis" characterized the contributions of individual nodes towards balancing integration and segregation over time (Figure 1.2) and revealed that individual brain regions show significant changes in their relative within- and between-module connectivity over time (Shine, Koyejo et al. 2016). Fronto-parietal, striatal and hippocampal regions notably spent a large proportion of the time acting as 'connector hubs' promoting global integration, as estimated by high cross-modular connectivity. It was however actually another class of regions, termed 'peripheral nodes', which dominated the dynamical cartographic landscape: peripheral nodes were characterized by low-to-medium within-module connectivity and low between-module connectivity. This indicates that that the majority of brain regions are in fact topologically isolated over time, and it is thus a minority of connector hub regions that provided a functional bridge between otherwise functionally segregated communities to enable windows of global integration over time (Shine, Koyejo et al. 2016).

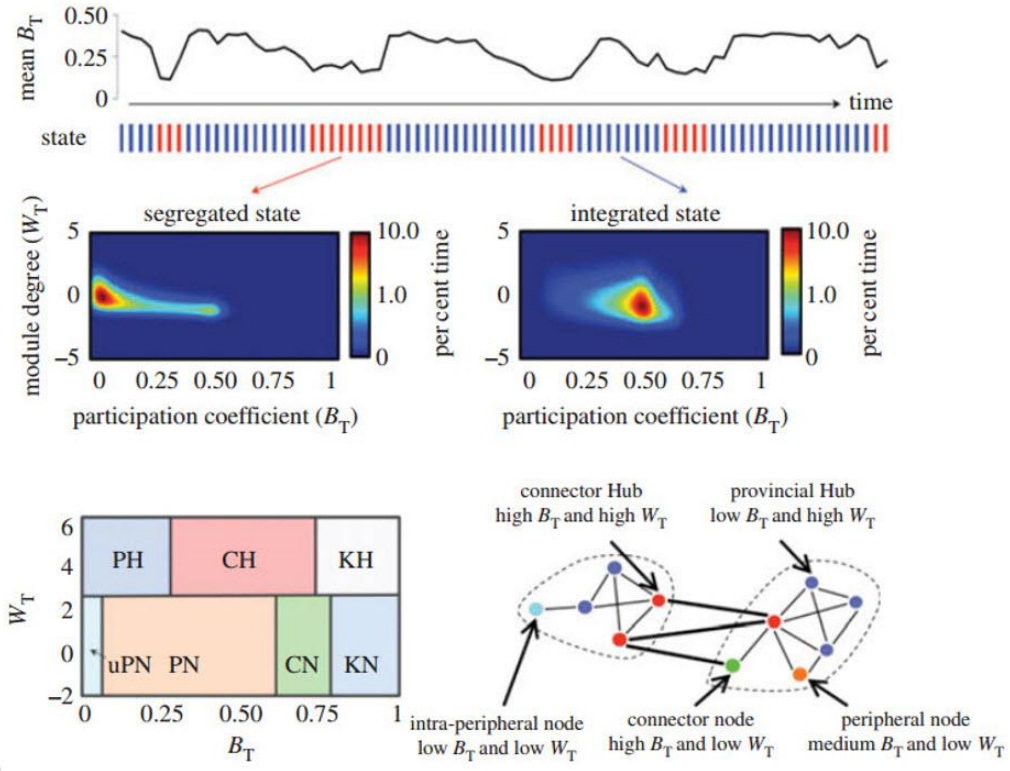


Figure 1.2. Measuring spatiotemporal integration and segregation. *Dynamic cartographic analysis performed on empirical FC data. Each time window (top) is broadly partitioned into either an 'integrated' topological state or 'segregated' topological state using* k*-means clustering. The heat maps show the mean cartographic profile of the segregated topological state (left) in which most nodes spend a high-proportion of time serving as peripheral nodes in the network topology. Conversely, the mean cartographic profile of the integrated topological state (right) comprises a significant proportion of nodes serving as hubs between different modules over the recording interval. Adapted from Shine, Koyejo et al. 2016.*

1.1.3 Neurobiological determinants of the integration / segregation balance: insights from whole-brain computational models

1.1.3.1 Overview of whole-brain computational modelling

The main premise of whole-brain computational models comes from statistical physics where it has been shown that macroscopic physical systems obey laws that are independent of their microscopic constituents. The firing dynamics of local neuronal populations may accordingly be approximated by stochastic differential equations without detailed knowledge of the behaviour and structure of individual neurons. Reduced dynamic mean field models or even simpler approximations of neural signals such as the Kuramoto oscillator (Kuramoto 1975) ignore the interactions between single neurons within a brain region and instead consider their ensemble dynamics (Cabral, Kringelbach et al. 2014, Deco and Kringelbach 2014). Whole-brain computational models may then constrain and couple the local dynamics between brain areas according to the underlying structural connectivity of the brain measured empirically with diffusion tensor imaging (DTI) (Figure 1.3). By

constraining the modelled activity according to the structural properties of the brain, the system operates within a biologically plausible space–time structure for coupling, conduction delays and noise (Cabral, Kringelbach et al. 2014). The dynamics generated by such models consist of neural time series that can be represented in space and time as functional networks and analysed using the same tools and approaches applied to empirical neuroimaging data. Recently developed whole-brain models have indeed shown promise towards replicating many features of the empirical FC and have the potential to clarify the relationship between brain structure and function on multiple timescales (Cabral, Hugues et al. 2012, Deco, Jirsa et al. 2013, Cabral, Kringelbach et al. 2014, Deco and Kringelbach 2014).

Whole-brain computational models can be used to test mechanistic hypotheses about the neural mechanisms balancing the integration and segregation of information in simulated brain networks by employing perturbational approaches (Figure 1.3). Integration and segregation can be thought of as complementary processes in the human brain: a global increase in integration will jointly lead to globally decreased segregation and vice versa (Figure 1.4). Although global integration and segregation values mirror each other, they are nevertheless computed in the models via different approaches (Deco, Tononi et al. 2015). Perturbational integration is defined by considering the length of the largest connected component of the binarized network as an estimate of the amount of integration in the system after each perturbation, and perturbational segregation is calculated through the entropy of the set of evoked patterns assuming a Gaussian distribution of stimulations (Deco, Tononi et al. 2015) (Figure 1.3).

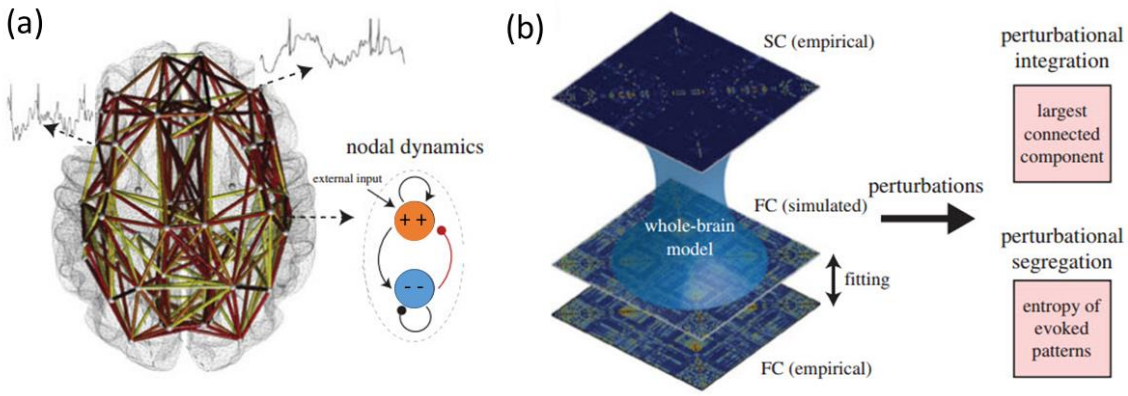


Figure 1.3. Overview of whole-brain computational modelling. (a): *Whole-brain computational modelling of functional neuroimaging data uses empirical SC data obtained from DTI tractography, and FC data on the corresponding anatomical parcellation. A whole-brain model can be constructed by coupling the simulated local node dynamics (in this exemplar case, a simple mean field model with excitatory [orange] and inhibitory [blue] neuronal populations) according to the SC. The modelled activity is thus constrained by both the strength of each anatomical coupling and the physical distance between brain regions, and further scaled according to a global conductance parameter (Cabral, Kringelbach et al. 2014, Deco and Kringelbach 2014).* (b): *A whole-brain computational model previously tuned to match the empirical data may be subjected to extrinsic perturbations* in silico. *This is done by injecting the modelled dynamics with a random set of Gaussian inputs. The amount of integration in the system can be calculated after each perturbation: perturbational integration is defined by considering the length of the largest connected component of the binarized network as an estimate of the amount of integration in the system after each perturbation. Similarly, perturbational segregation is calculated through the entropy of the set of evoked patterns assuming a Gaussian distribution of stimulations (Deco, Tononi et al. 2015). Panel* (a) *adapted from Hellyer, Jachs et al. 2016. Panel* (b) *adapted from Deco, Tononi et al. 2015.*

1.1.3.2 Contributions of neuroanatomical connectivity to Integration/Segregation

Whole-brain computational models have begun to provide insights into causal mechanisms via which the anatomical connectome shapes and constrains the brain's global dynamical repertoire in both health and disease (Honey, Sporns et al. 2009, Deco, Jirsa et al. 2013, Deco and Kringelbach 2014). Evidence suggests that the network organization of white matter fibre tracts shapes the repertoire of transient networks states explored by the simulated neural dynamics, without being its sole determinant (Deco, Jirsa et al. 2013, Hansen, Battaglia et al. 2015). The relationship between brain structural connectivity and dynamics is therefore analogous to the way in which the geological bedding of a river basin influences its flows of water; the physical structure strongly constrains the flow of water, but other factors such as atmospheric conditions and rainfalls also influence the behaviour of the system in non-trivial ways.

A natural use for whole-brain models is to thus investigate how changes in the structure of the brain may influence global brain dynamics *in silico*, especially as it pertains to the integration and segregation of information. For example, the effects of a pathological disconnection were simulated by randomly pruning anatomical connections in the network

in a stepwise manner, thereby reducing the small-world character of the original anatomical connectome (Cabral, Hugues et al. 2012). These structural disconnections resulted in simulated functional networks with altered topological attributes including an increase in global efficiency, decrease in clustering, randomization of the degree distribution, the combined effect of which led to deviations from a small-world topological organization of FC networks. This virtual experiment demonstrated that structural changes in white matter connectivity, analogous to those driven by pathological processes, can cause imbalances between integration and segregation on a functional level by altering the spatial patterns explored by the neural activity.

A recent computational study employed a complementary approach and outfitted an otherwise realistic whole-brain model with a range of artificial structural connectivities: from a structured lattice to a completely random connectome (Watts and Strogatz 1998, Deco, Tononi et al. 2015). Simulation of whole-brain dynamics on the different structural networks demonstrated that, as the structural connectivity gradually changes from an ordered lattice to a disordered graph, *perturbational integration* decreases because randomness shortens the length of the largest component in the network at a given threshold. *Perturbational segregation*, on the other hand, follows an opposite trend and increases as the structure approaches a random topology. Importantly, the optimal balance between functional integration and segregation is obtained at an intermediate structural connectivity between order and randomness (Deco, Tononi et al. 2015) (Figure 1.4).

Taken together, these findings from whole-brain computational modelling studies highlight the importance of the neuroanatomical connectome towards shaping global brain dynamics in a manner that enables both locally specialized computations and global communication.

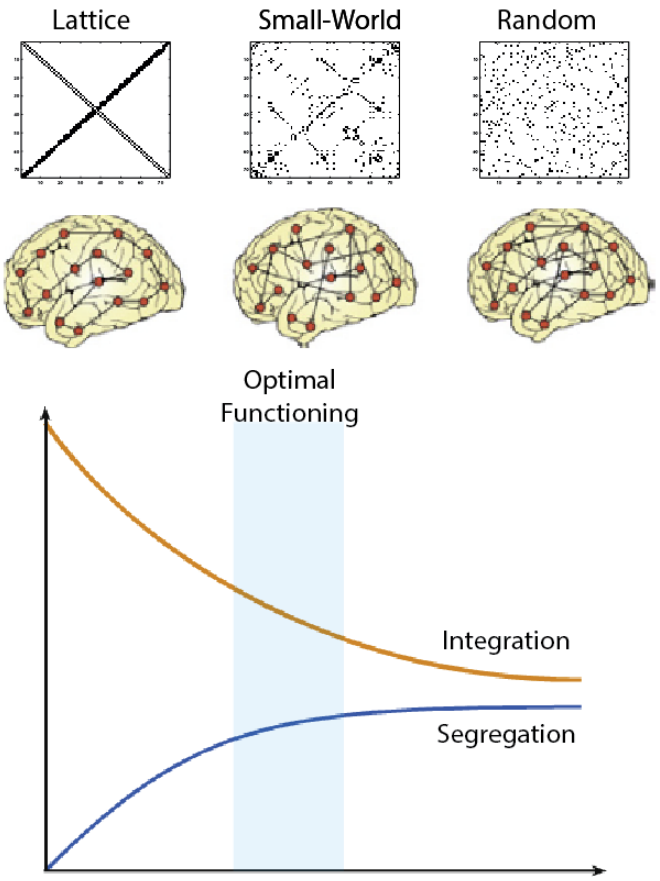


Figure 1.4. Influences of brain structural connectivity on integration and segregation. *To investigate the effect of different degrees of small-world architecture of the structural connectome on the integration and segregation of neural activity* in silico*, an otherwise realistic whole-brain model can be outfitted with different artificial structural connectomes. Simulating whole-brain dynamics on the different structural networks demonstrated that, as the structural connectivity gradually changes from an ordered lattice to a disordered graph, perturbational integration decreases because randomness shortens the length of the largest component in the network, while perturbational segregation follows the opposite trend because randomness increases the capability to distinguish between two different external inputs. The optimal balance between functional integration and segregation is obtained at an intermediate (i.e. small-world) structural connectivity between order and randomness (Deco, Tononi et al. 2015).*

1.1.3.3 Contributions of the excitatory-to-inhibitory ratio (E/I) to Integration/Segregation

A small-world structural connectome is necessary but not sufficient to enable the balanced integration and segregation of information processes in the human brain. To sustain complex mental functions, the neuroanatomical connectivity must act synergistically with another key ingredient to generate the requisite dynamical repertoire: a balanced ratio of excitation to inhibition (*E*/*I*). The *E*/*I* ratio is a form of homeostatic plasticity that maintains neuronal activity within a narrow range needed for healthy functioning; it refers to the relative levels of excitatory and inhibitory drive in a neural circuit (Haider, Duque et al. 2006, Okun and Lampl 2008). Recent experimental evidence suggests that the *E*/*I* ratio remains relatively stable in pyramidal neurons over both space and time (Figure 1.5). This

is notably achieved by continually adapting the synaptic strengths of parvalbumin-expressing inhibitory interneurons onto principal cells proportionally to their respective excitatory drive (Xue, Atallah et al. 2014). Examples of the distinct types of reciprocal interactions between principal cells and inhibitory interneurons which generate high-frequency local oscillations are schematically represented in Figure 1.5.

Evidence has been coalescing around the idea that *E*/*I* balance may be a neurobiological determinant for maintaining the brain's dynamical regime near criticality (Shew, Yang et al. 2011, Turkheimer, Leech et al. 2015). Criticality is a state characterized by the spontaneous emergence of self-similar dynamics over the spatial and temporal domains in complex physical systems poised between order and randomness (Bak 2013). Experimental evidence suggest that brain dynamics exhibit a large degree of concordance with those expected for a system near criticality (Chialvo 2010, Expert, Lambiotte et al. 2011). In the critical state, the dynamics of the system are dominated by small bursts of local (i.e. segregated) activity, yet large avalanches of globally synchronized (i.e. integrated) activity, referred to as 'neuronal avalanches', occasionally arise which cover nearly the entire system (Beggs and Plenz 2003, Beggs 2008). Operating near criticality may be ecologically advantageous for the brain by notably enabling the flexible integration (i.e. co-activation of a few large clusters) and segregation (i.e. co-activation of many small clusters) of information, thereby maximizing the system's information processing capabilities (Beggs 2008, Bak 2013). Importantly, a balanced *E*/*I* ratio is thought to be needed to sustain a critical dynamical regime, and thereby balance the processes of integration and segregation of information over the entire system (Beggs 2008, Shew, Yang et al. 2011, Tagliazucchi and Chialvo 2013) (Figure 1.5).

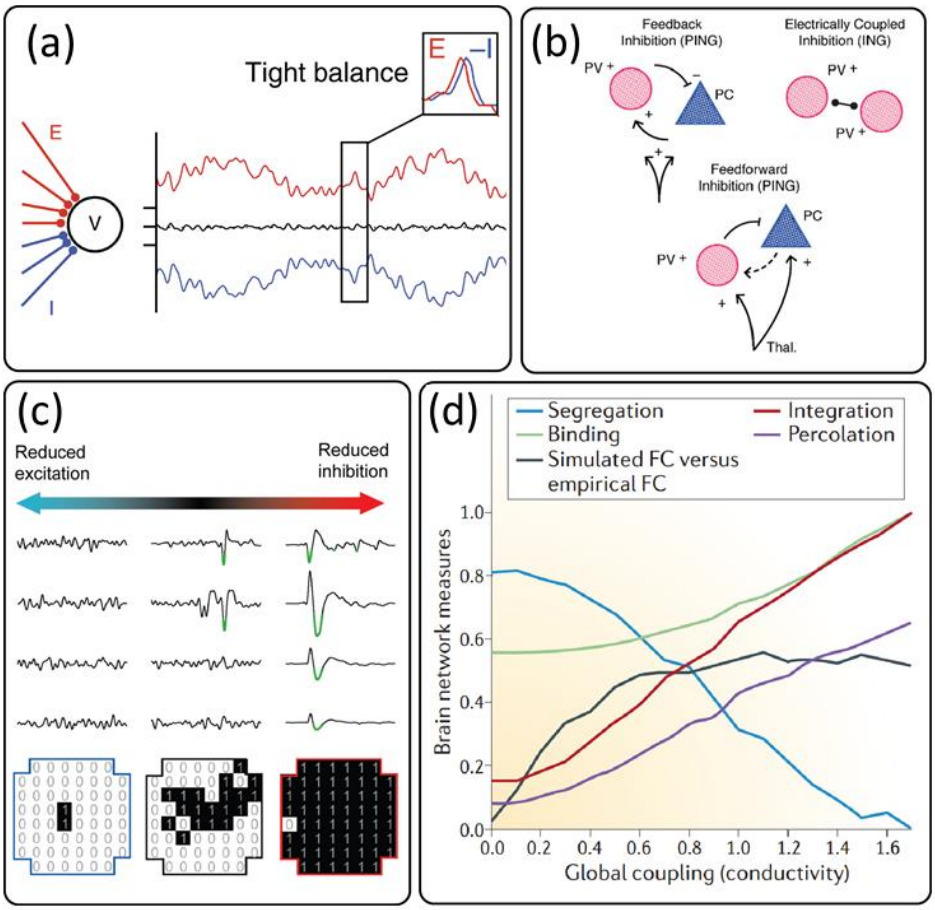


Figure 1.5. Influences of the* E/I *balance on integration and segregation. (a) *To allow for healthy brain function, excitation (red) and inhibition (blue) must be tightly balanced over both space and time. (*b*) Reciprocal interactions between excitatory pyramidal cells and inhibitory interneurons at the level of cortical microcircuits maintain the* E/I *ratio within a narrow range capable of generating high-frequency neural oscillations (Turkheimer, Leech et al. 2015). (*c*) Local field potential (LFP) recordings experimentally recorded under conditions of suppressed excitation (left), suppressed inhibition (right) or unperturbed* E/I *(middle). Population LFP events represented as binary patterns: 1 = active site; 0 = inactive. Suppressed excitation leads to a loss of integration as only the activation of isolated network clusters is possible (bottom left). Suppressed inhibition leads to a loss of segregation and co-activation of large clusters covering nearly the entire system (bottom right), reflecting excessive integration. Balanced* E/I *(bottom middle) enables the co-activation of clusters of all sizes [53].* (d) *Scaling up the global conductance parameter in a whole-brain computational model has a profound impact on the functional network dynamics. Whole-brain computational models have shown that the best fit between the simulated and empirical FC matrices is obtained when the system operates in a metastable synchronization state where excitation and inhibition are balanced. The measures of perturbational integration and segregation also become optimally balanced at these intermediate global conductance values. The percolation measure plotted refers to the probability that two neighboring nodes are functionally connected, hence reducing the probability that an imaginary 'liquid' would find an open path through the network. Percolation increases at higher global conductance values where integration is also maximized (Deco and Kringelbach 2014). Adapted from Lord, Stevner et al. 2017.*

Whole-brain computational models have recently been used to investigate the mechanistic relationships between the *E*/*I* ratio, critical dynamics, and the systemic integration / segregation balance in macroscopic brain networks. In whole-brain models, the *E*/*I* ratio would dictate the dynamical regime of local neural masses, and help shape network activity across the entire system via symbiotic interactions with the underlying structural

connectivity (Cabral, Kringelbach et al. 2014, Deco and Kringelbach 2014). A whole-brain modelling experiment has notably shown that, for a fixed structural connectome, manipulating the global conductance of the model can have a profound impact on the functional network dynamics (Deco, Tononi et al. 2015). In neurobiological terms, an increase in the model's global conductance parameter would be equivalent to scaling up the excitatory couplings between brain areas. The enhancement of global excitatory coupling would be expected to increase long-range correlations in the network. A decrease in global coupling should have the opposite effect, and effectively simulate a shift in the *E*/*I* balance favouring inhibition. Whole-brain computational models have demonstrated that the best fit between the simulated and empirical FC matrices is obtained when the system operates in a metastable synchronization state where excitation and inhibition are balanced (Cabral, Hugues et al. 2011, Cabral, Kringelbach et al. 2014, Deco and Kringelbach 2014). Importantly, the measures of perturbational integration and segregation also become optimally balanced at these intermediate global conductance values (Deco, Tononi et al. 2015). As expected from theoretical predictions of criticality, exceeding this optimal global coupling value leads to enhanced systemic integration at the expense of segregation, and reducing it results in lower perturbational integration scores and increased segregation (Figure 1.5).

Thus, in summary, the available evidence suggests that two key ingredients must act synergistically to efficiently balance functional integration and segregation in the healthy brain: i) a small-world structural connectome and ii) balanced ratio of excitation-to-inhibition in local neuronal populations.

1.2 Theoretical Accounts of Consciousness

1.2.1 Dynamic Core Theory

Since the contemporary recognition of consciousness as a neurobiological phenomenon that can be subjected to scientific study (Crick and Koch 1990), several theoretical accounts of neural mechanisms of consciousness have been put forth. For the purposes of this Thesis, I will present those models based on the phenomenology of consciousness, namely the *dynamic core theory* and *information integration theory* (IIT) and a theoretically-based index of consciousness termed the perturbational complexity index (PCI). Whilst probing the neural bases of consciousness from different viewpoints, these

models each attempt to describe neural *processes* underlying the conscious experience, and do not attribute consciousness to particular brain area(s) from a localist perspective.

Let us begin by considering two key phenomenological properties of each conscious experience, as outlined by Tononi & Edelman (Tononi and Edelman 1998). Firstly, it was proposed that each conscious experience is *integrated* irrespective of its specific content. In other words, each conscious scene is unified and fused into a unitary experience containing elements from all sensory modalities, internally generated thoughts and cognition. It is therefore undecomposable into sub-parts that could be consciously perceived independently of the whole (Tononi and Edelman 1998, Cleeremans 2003, Cavanna, Vilas et al. 2017). Secondly, it was proposed that conscious experiences are highly *differentiated* from one another. That is, while each conscious experience is an integrated whole, the possible repertoire of possible conscious experiences is extraordinarily vast and, as such, the occurrence of a given conscious state implies an extremely rapid selection among this vast repertoire of possible conscious states (Tononi and Edelman 1998). Differentiation among an extensive repertoire of possibilities constitutes information in the context of reduction of uncertainty. Each differentiated conscious scene is therefore highly informative (Shannon, Weaver et al. 1951, Tononi and Edelman 1998). This would also imply that the vast number of differentiable conscious experiences are supported by an (at least) equally large number of distinct physical brain states and the transitions between them (Cavanna, Vilas et al. 2017).

It follows that that the distributed neural process underlying conscious experience must be, at the same time, functionally integrated and highly differentiated. Tononi & Edelman therefore proposed that consciousness involves the constant shaping and re-shaping over time of an irreducible, simultaneously integrated and differentiated set of regions termed the "dynamic core" (Figure 1.6). Specifically, a group of neurons can contribute directly to conscious experience only if: i) it is part of a distributed functional cluster that achieves high integration in hundreds of milliseconds; and ii) this functional cluster is highly differentiated (i.e. its activity patterns must be selected within less than a second out of a very large repertoire) (Tononi and Edelman 1998). Importantly, the "dynamic core" theory highlights the role of functional interactions among distributed groups of neurons whose composition may change over time (and/or across individuals), and does not refer to the local properties of an invariant set of brain areas.

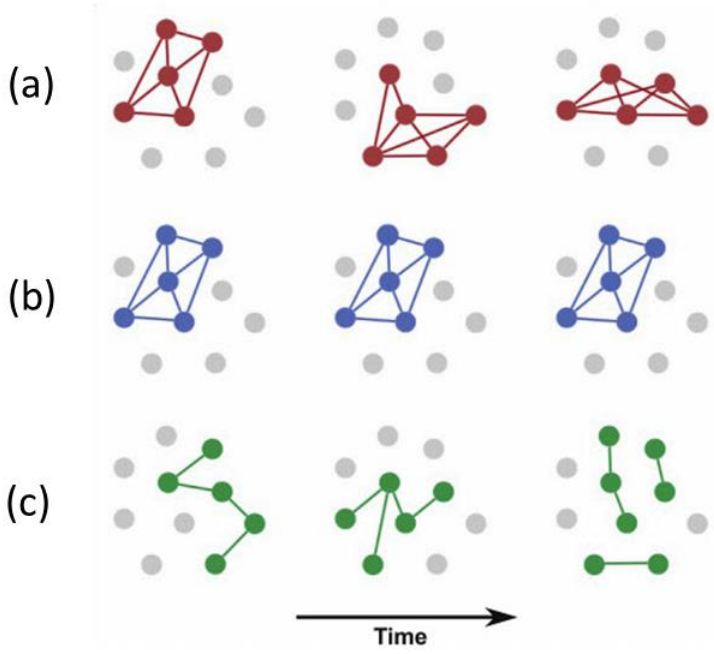


Figure 1.6. Schematic representation of the Dynamic Core Theory. (a) *The dynamic core theory proposes that* both *integration and differentiation must co-occur amongst distributed groups of neurons over time (i.e. dynamic core) in order to sustain consciousness.* (b) *Very high integration constrains the number of possible configurations to just a few synchronization patterns which cannot be sufficiently* differentiated *to enable consciousness.* (c) *Conversely, assemblies lacking integration would also not be able to support conscious experiences according to the dynamic core theory. Adapted from Cavanna, Vilas et al. 2017.*

As stated above, a dynamical competition occurs between integration and differentiation, since differentiation is maximized when all members of a system behave independently (which effectively prevents integration), whilst integration constrains the behavior of the system to a smaller repertoire of possible configurations. This competition can be quantified over time, and the simultaneous occurrence of integration and differentiation leads to patterns of the highest *neural complexity* that are in turn proposed to accompany consciousness (Tononi and Edelman 1998).

1.2.2 Information Integration Theory

The information integration theory (IIT) is rooted in the same two phenomenological considerations as the dynamic core theory, namely that each conscious scene is simultaneously unified as an *integrated* whole that cannot be reduced to non-interdependent components; and "unique" or *differentiated* (i.e. it is only one in in content and spatiotemporal grain, and not a superposition of multiple experiences) (Tononi 2004). According to IIT: "*to measure information integration, it is essential to know whether a set of elements constitute a causally integrated system, or they can be broken down into a number of independent or quasi-independent subsets among which no information can be*

integrated" (Tononi 2004). Thus, an important distinction between IIT and the dynamic core theory described earlier is that IIT concerns directed, causal interactions within a system.

The premise of IIT is to measure the information generated when a subset of elements *S* of a system X enters a particular state out of its repertoire, but only to the extent that such information can be integrated (that this state results from causal interactions within the system). A measure called ϕ was therefore introduced in order to measure a system's capacity for integrating information, where ϕ is the amount of causally effective information that can be integrated across the informational weakest link of a subset of elements (Tononi 2004). As shown for example in Figure 1.7 *(a)*, this can be calculated by first dividing a subset of elements into a bipartition and evaluating the responses of the set of elements *B* that can be caused by all possible inputs (i.e. firing patterns) originating from the set of elements *A* (and vice-versa); a measure coined as the *effective information*. The effective information is then computed for every possible bipartition within S (i.e. {1}/{2,3,4}, {1,3}/{2,4}, {3,4}/{1,2}, ...) and one may then identify the bipartition for which the effective information is minimized which is termed the *minimum information bipartition(s)* of *S.* The quantity ϕ of a subset *S* is defined as the effective information of the minimum information bipartition of S. The next step is to search for *complexes*, which are defined as a subset of elements with $\phi > 0$ *and* with no inclusive subset of higher ϕ. For example, subset {1,2} shown in Figure 1.7 *(c)*, under its only bipartition {1}/{2}, is indeed a *complex* because it has a higher ϕ than any of its inclusive subsets in this example (i.e. {1,2,3,4}, {1,2,3}, {1,2,4}). These steps are repeated for each possible subset of elements and their associated bipartitions across the entire system. Complexes can then be ranked according to their respective ϕ values, and the complex with the maximum value of $\phi(S)$ is referred to as the *main complex.* The IIT therefore characterizes consciousness as the potential differentiation of a system's responses to all possible perturbations. A key claim of IIT is that the neural substrate of consciousness is a complex of high ϕ that is capable of integrating a large amount of information (i.e. the *main complex*). The belonging of a group of neurons to the main complex therefore determines whether or not it contributes directly to a conscious scene (Tononi 2004).

Although the quantity ϕ is a theoretically appealing concept to quantify consciousness in any system (living or synthetic), the direct empirical testing of the IIT would require the repeated stimulation of innumerably large number of neural subsets using a wide range of inputs (i.e. stimulation parameters), together with the extremely detailed

mapping the repertoire of outputs for following each stimulation. Such an experiment is clearly not practically feasible with the methods available today and, even should novel neuroimaging and neuromodulation techniques eventually render this kind of investigation possible, there would remain significant ethical problems with causally interfering with the human brain to such a dramatic extent. Even the computation of ϕ in a macro-scale computational model is arguably not feasible with the computing power available today, which has motivated the use of alternative approaches to study information integration *in silico* using perturbational measures (Deco, Tononi et al. 2015).

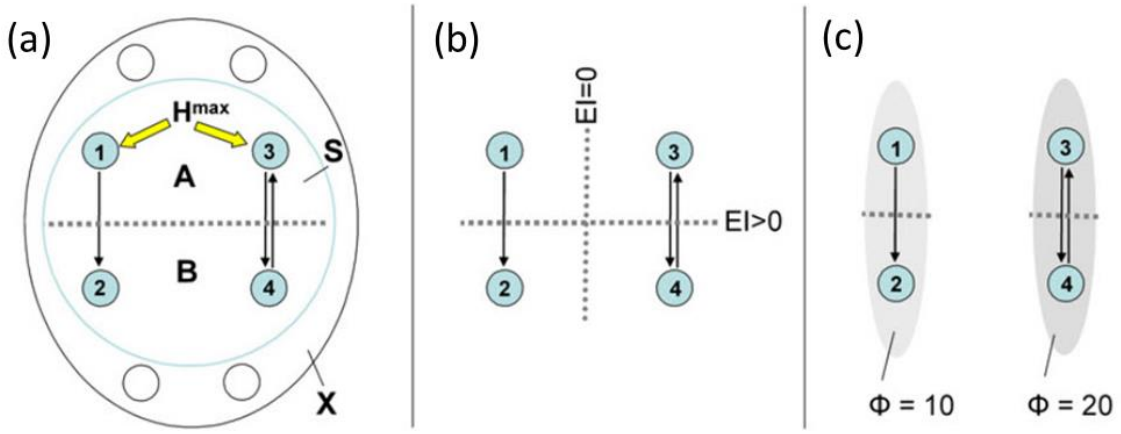


Figure 1.7. Toy example illustrating key concepts of the Information Integration Theory of Consciousness (IIT). *The quantity ϕ of a subset* S *{1,2,3,4} is defined as the effective information of the minimum information bipartition of* S. *To find the* minimum information bipartition *of* S, *one has to calculate the* effective information *(EI) of every possible bipartition of S. For example in* (a), *the EI between subsets A: {1,3} and B: {2,4} forming a bipartition of S is calculated by evaluating the responses of B that can be caused by all possible inputs (i.e. firing patterns) originating from A (i.e. the maximum entropy to the outputs from subset* A*), and vice-versa.* (b) *Here the EI of the bipartition {1,3}/{2,3} will have a positive value, but the EI of bipartition {1,2}/{3,4} will be equal to zero, because these subsets are not connected and hence inputs from {1,2} elements will not affect {3,4} (assuming they do not influence each other indirectly via the other elements making up the rest of the system system X); as such it will not be possible to distinguish the effect of different inputs from {1,2} on subset {3,4}. Repeating this procedure for every possible bipartition of* S, *the ϕ of a subset S is defined as the effective information of the minimum information bipartition of the subset* S. *The next step is to search for* complexes*, which are defined as a subset of elements of size $n \geq 2$, with $\phi > 0$* and *with no inclusive subset of higher ϕ. For example, subset {1,2} shown in* (c), *under its only bipartition {1}/{2} is indeed a* complex *because it has a higher ϕ than any of its inclusive subsets (i.e. {1,2,3,4}, {1,2,3}, etc.). This is also the case of subset {3,4}. By repeating this procedure for all possible subsets in the system, the complex with the maximum value of $\phi(S)$ can be found and neuronal populations belonging to this so-called "*main complex*" are thought to contribute to the conscious scene at this point in time. Adapted from Tononi 2004.*

1.2.3 Perturbational Complexity Index

In order to experimentally investigate whether consciousness depends on brain activity patterns that are, at once, distributed among interacting cortical areas (i.e. *integrated*) and *differentiated* in space and time, Casali and colleagues introduced a theory-driven index of the level of consciousness inspired from IIT called the perturbational

complexity index (PCI) (Casali, Gosseries et al. 2013). The PCI is calculated by first perturbing the cortex with transcranial magnetic stimulation (TMS) and assessing the complexity of the spatiotemporal cortical activation pattern elicited by the stimulation (Figure 1.8). Operationally, for each stimulation, the corresponding distributions of TMS-evoked cortical currents (over space and time) are binarized into a matrix of significant activations. The information content of this matrix is then calculated using the Lempel-Ziv complexity index, which approximates the amount of non-redundant information contained in a binary sequence by estimating the minimal number of different patterns necessary to describe the sequence (i.e. the compressibility of a sequence of information). The PCI was then defined as the Lempel-Ziv complexity index, normalized by the correspondent source entropy (Casali, Gosseries et al. 2013).

Based on this definition, the PCI should be maximized when TMS-evoked activation patterns reflect the *joint* presence of integration and differentiation. That is, if the TMS pulse evokes only local activity, the matrix of activation will be spatially restricted and the information it carries more easily compressible, leading to a low PCI due to a loss of integration. Moreover, if many interacting areas all react to the perturbation, but they do so in a stereotypic way, this loss of differentiation would also lead to a low PCI value. Conversely, the PCI would only be high when the exogenous perturbation is transmitted to a large set of integrated areas that react differently to it, giving rise to a spatiotemporal pattern of activation that cannot be easily reduced or compressed (Casali, Gosseries et al. 2013). These theoretical predictions were indeed reflected in the experimental PCI calculations associated with different states of consciousness. For example, during wakefulness, significant TMS-evoked responses were found in a distributed set of cortical areas, which became active at different latencies, resulting in an overall spatiotemporal pattern of cortical activation that was not easily compressible (i.e. high PCI). On other hand, during NREM sleep, these same stimulation parameters elicited a local, short-lasting response and lower PCI due to a loss of integration. Increasing the stimulation intensity during NREM sleep elicited a global cortical response in which many brain regions were steadily activated for a few hundred milliseconds, resulting in a lower PCI value, this time due to a loss of differentiation (Figure 1.8).

Although the PCI leverages on a sophisticated experimental setup to provide a reliable classification of one's vigilance state, there are some limitations associated with this index. Notably, whilst the PCI calculation is based on brain activity changes resulting from

a targeted manipulation of the system's dynamics *in vivo* (contrary to correlational neuroimaging investigations), it still does not reveal the actual *neural mechanisms* responsible for the different TMS-evoked activity changes in sleep versus wakefulness. Another limitation of the PCI is that, due to methodological and ethical constraints, it is only possible to perturb the activity of a single brain region at a time, whereas signals arising from several different sources are likely to differentially propagate across the brain in reality. Finally, although inspired from the IIT, the PCI calculation remains very different from that of the quantity ϕ, as described above (Tononi 2004).

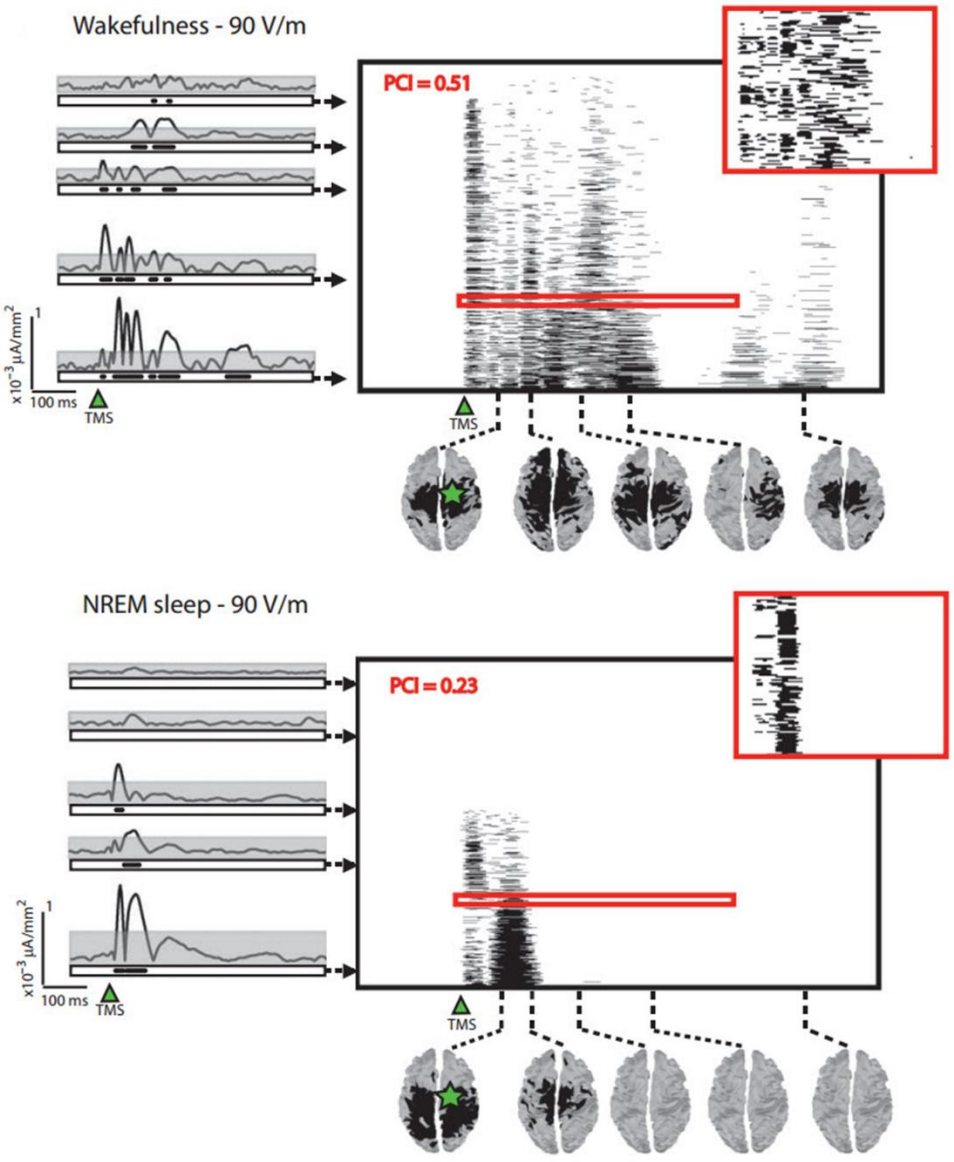


Figure 1.8. Perturbational Complexity Index (PCI) measured in wakefulness and NREM sleep. Top: *EEG reconstruction of brain activity response following TMS pulse targeting the right premotor cortex during wakefulness. The elicited activation pattern rapidly spreads to multiple cortical areas far beyond the stimulation site and lasts up to 300 ms.* Bottom: *The application of the same stimulation during NREM sleep elicits a brief activation that remains mostly localized to the area of stimulation. The Perturbational*

Complexity Index (PCI) can then be calculated from the TMS-evoked EEG spatiotemporal activation patterns described. Operationally, the PCI is derived by calculating the Lempel-Ziv complexity for the binarized matrix describing where (x) and when (t) TMS evokes significant cortical activity, and normalizing this value by the source entropy. The binarized SS(x,t) matrices following a TMS perturbation at 90 V/m are shown for wakefulness (top) and NREM sleep (bottom). PCI is maximized during wakefulness due to the co-occurrence of integration and differentiation in the TMS-evoked spatiotemporal dynamics. Adapted from Casali, Gosseries et al. 2013.

In summary, I have presented two influential theories of consciousness; the dynamic core theory and integrated information theory (IIT), as well as an experimental implementation of the latter termed the perturbational complexity index (PCI). These theoretical models are highly relevant in the context of our discussion of the *dynamical* integration and segregation balance as a key feature of information processing in the human brain. Indeed, the dynamic core theory, IIT and PCI all suggest, albeit from slightly different perspectives, that a brain dynamical landscape promoting either excessive integration or excessive segregation will not be able to support consciousness as we experience it under normal conditions. These models therefore provide a useful theoretical foundation for interpreting the experimental results pertaining to the integration/segregation balance in altered states of consciousness (i.e. psychedelic state and slow-wave sleep) that will be presented in Chapters 3, 4 and 5 respectively. Furthermore, the aforementioned theoretical accounts speak in favor of a whole-brain perspective when studying consciousness experimentally, rather than a localist approach.

1.3 Psychopharmacology and Neuroimaging of Psilocybin

1.3.1 History, Phenomenology & Pharmacological properties

Serotonergic psychedelics may well be the oldest class of psychopharmacological agents known to man (Nichols 2016). Psilocybin, the psychoactive ingredient in "magic mushrooms", has been used ubiquitously in religious ceremonies throughout history, the first record of which dates as far back as Aztec rituals (Ott 1976, Nichols 2016). Classic serotonergic psychedelics include psilocybin, mescaline, lysergic acid diethylamide (LSD), and dimethyltryptamine (DMT), all of which have agonist or partial agonist activity at the serotonin 5-HT_{2A} receptor subtype as their primary mode of action. By contrast the psychedelic drugs ketamine and 3,4-Methylenedioxymethamphetamine (MDMA) are not considered serotonergic psychedelics since the former acts as a selective antagonist of the NMDA receptor, and the latter has presynaptic releasing agent for both norepinephrine and dopamine in addition to serotonin. Psilocybin is of particular interest to the works presented in this Thesis, as I notably performed neuroimaging analyses on the first ever

fMRI dataset in which psilocybin was administered at the time of scanning (Carhart-Harris, Erritzoe et al. 2012).

Psychedelics have been described as different from other classes of drugs due to "their capacity to reliably induce states of altered perception, thought, and feeling that are not experienced otherwise except in dreams or at times of religious exaltation" (Goodman 1996). In light of these effects, it is perhaps unsurprising that the use of psychedelics has historically been central feature of religious practices in many cultures. The relative lack of research on psychedelics despite their significant historical use can largely be attributed to political influences (Nichols 2016). LSD in particular was believed to contribute to an anti-war sentiment amongst youths in the 1960's and branded a menace to society. The ensuing Controlled Substances Act of 1970 hence categorized all psychedelics as Schedule 1 drugs. This effectively prevented any scientific research into their mechanism of action and ended (legal) psychedelic-assisted therapy. However the regulatory landscape began changing in the 1990's and, since 2006, the therapeutic potential of psychedelics (especially psilocybin) for psychiatric disorders has notably been investigated in multiple trials for treatment-resistant depression, addictive disorders, and anxiety associated with end-of-life care (Rucker, Iliff et al. 2018).

The phenomenology of psilocybin was recently examined by Turton and colleagues who reported on the subjective experience of intravenous psilocybin (2 mg dose) administered during the same fMRI scans analyzed in this Thesis. To explore the effects of psilocybin, semi-structured interviews were conducted and their contents were analyzed by Interpretive Phenomenological Analysis (Turton, Nutt et al. 2014). All subjects reported rapid and intense drug effects and nine broad categories of subjective effects were identified (Figure 1.9). Perceptual changes were described as the primary effects of the drug and changes in cognition and mood were also reported by most participants. Many participants found the experience difficult to describe, yet overall pleasant.

The main pharmacological basis of these effects is thought to involve activation of the serotonin 5-HT_{2A} receptor subtype. Psilocybin is rapidly dephosphorylated in the body to psilocin, which has high affinity for the 5-HT_{2B} and 5-HT_{2C} receptors in the human brain, a slightly lower affinity for the 5-HT_{2A} receptor, and comparatively low affinity to 5-HT1 receptors (Passie, Seifert et al. 2002). Psilocybin is primarily metabolized in the liver and has a mean half-life of approximately 160 minutes when taken orally and 75 minutes when

administered intravenously (Passie, Seifert et al. 2002). The link between psilocybin's subjective psychological effects and 5-HT_{2A} receptor activation has been convincingly established by several experiments in which the compound was jointly administered with the 5-HT_{2A} receptor antagonist ketanserin (which has no psychoactive effect when given alone). This manipulation successfully blocked various effects of psilocybin including mood-enhancement, disinhibition, hallucinations, and the typically observed increase on the 5-Dimensional Altered States of Consciousness Rating Scale (Vollenweider, Vollenweider-Scherpenhuyzen et al. 1998, Kometer, Schmidt et al. 2012, Kometer, Schmidt et al. 2013). At the cellular level, evidence suggests that stimulation of the 5-HT_{2A} receptor reduces outward potassium currents in the host cell and thus increases neuronal excitation, and that these receptors show differential expression patterns in distinct pyramidal cells and interneurons classes (Andrade 2011). Finally, the distribution and densities of serotonin 5-HT_{2A} receptors in the human brain (and other 5-HT receptor subtypes) were recently estimated in a high-resolution atlas using molecular and structural neuroimaging data in a large cohort of healthy individuals in combination with postmortem human brain autoradiography (Beliveau, Ganz et al. 2017). The results showed that these receptors were widely distributed across the brain but most densely expressed in the lateral prefrontal, parietal and temporal cortices as well as midline structures including the posterior and anterior cingulate cortices. The psychoactive properties of psilocybin may therefore be due to the preferential binding of psilocin at these brain areas, although further studies are needed to confirm this.

1.3.2 Neuroimaging studies of psilocybin

Although it had long been assumed that psychedelics worked by increasing brain activity, the first fMRI study of psychedelics instead revealed widespread reductions in cerebral blood flow (CBF) measured with arterial spin labeling perfusion as well as in the BOLD signal following an intravenous psilocybin injection (Carhart-Harris, Erritzoe et al. 2012). Significant activity reductions were found in several subcortical and cortical regions including (but not limited to): bilateral thalamus and putamen, posterior cingulate cortex (PCC), retrosplenial cortex, precuneus, supramarginal gyrus, anterior cingulate cortex (ACC), medial prefrontal cortex (mPFC), frontoinsular cortex, lateral orbitofrontal cortex, precentral gyrus, and superior, middle and inferior frontal gyrus (Figure 1.9). As such, the affected regions majoritarily comprised high-level frontal and parietal association areas and/or important connector hubs such as the thalamus, ACC and PCC. The authors

reconciled these findings with the earlier observation that activation of 5-HT_{2A} receptors actually depolarizes neurons *in vitro* by suggesting that psilocybin may have mediated the observed deactivations via the 5-HT_{2A}-induced excitation of fast-spiking interneurons terminating on pyramidal cells. Interestingly, despite the relatively small sample size (n = 15), the magnitude of the percent CBF reduction (post vs pre-injection) in the thalamus, ACC and PCC each significantly correlated with the intensity of the subjective effects reported by study participants. Furthermore, the drug significantly decreased the positive coupling between the mPFC and PCC; the same two regions regions that showed the most consistent deactivations after psilocybin. It was therefore proposed that psilocybin may work by decreasing activity and connectivity in the brain's key connector hubs, enabling a state of unconstrained cognition (Carhart-Harris, Erritzoe et al. 2012).

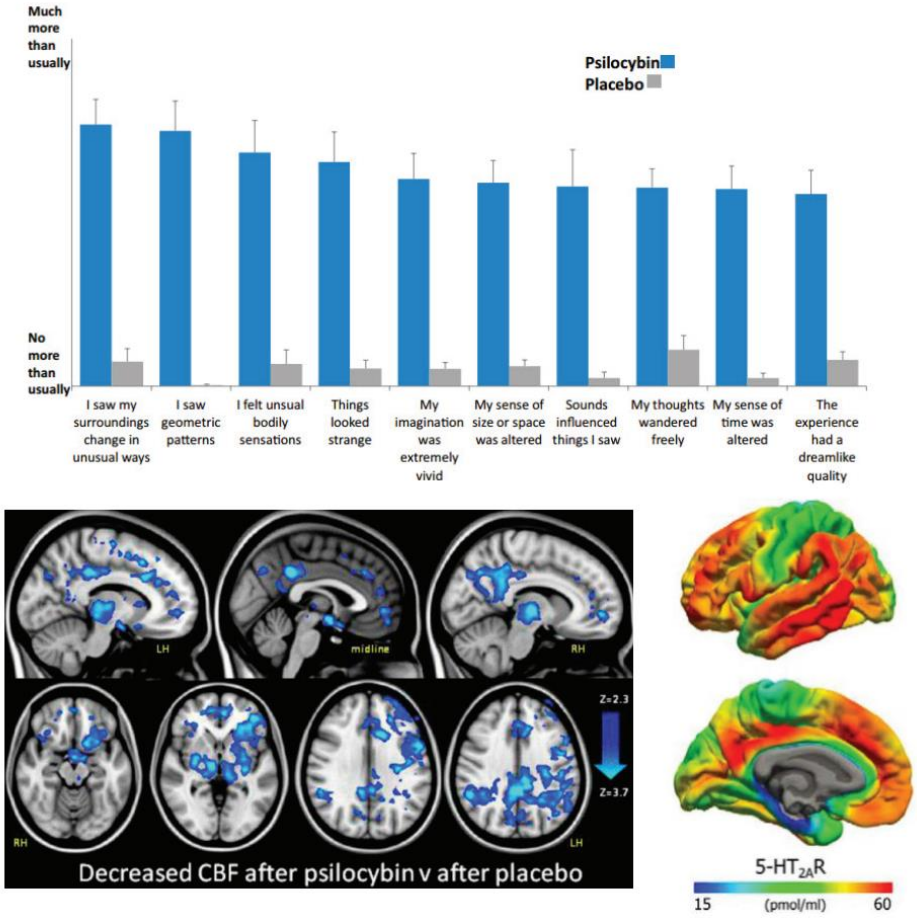


Figure 1.9. Phenomenology and metabolic changes following a psilocybin infusion. Top: *Subjective ratings of different aspects of the psychedelic experience collected shortly after subjects were injected with either psilocybin (blue) or placebo (gray) during an fMRI scan (Carhart-Harris, Erritzoe et al. 2012).* Bottom: *Left panel: Psilocybin significantly decreases cerebral blood flow (CBF) relative to placebo in a large number of brain regions including (but not limited to): bilateral thalamus and putamen, posterior cingulate cortex, retrosplenial cortex, precuneus, supramarginal gyrus, anterior cingulate cortex, medial prefrontal cortex, frontoinsular cortex, lateral orbitofrontal cortex, precentral gyrus, and superior, middle and inferior frontal gyri (adapted from Carhart-Harris, Erritzoe et al. 2012). Right panel: 5-HT_{2A} receptor map estimated from*

molecular and structural neuroimaging data in conjunction with postmortem human brain autoradiography (adapted from Beliveau, Ganz et al. 2017).

These initial results have since been complemented by further functional neuroimaging studies, which have notably investigated changes at the systems-level under psilocybin and other serotonergic psychedelics. Roseman and colleagues measured changes in resting-state functional connectivity between a standard template of canonical resting-state networks (RSNs) derived via independent components analysis (Roseman, Leech et al. 2014). Resting-state networks are highly structured patterns of co-variations in the slow component (< 0.1 Hz) of the BOLD signal. A RSN thus comprises areas distributed across the brain that are connected through statistical interdependencies of their activity timecourses (Friston 1994), derived from seed-based regression analysis, or spatial independent component analysis (ICA). Resting-state networks are traditionally categorized into primary sensory networks (i.e. visual, auditory, and somatosensory), and higher-order networks (i.e. dorsal attention, fronto-parietal, central executive, language, and default mode). In this particular study, the ICA-derived masks were back-projected into each 4D fMRI dataset using a general linear model and a single time-course was for thus extracted for each subject and for each RSN. The time course for a specific RSN was used as the dependent variable in a general linear model, with the time course of another RSN entered as an independent variable, and the procedure repeated for each RSN pair. The results revealed that between-network functional connectivity was significantly increased under psilocybin relative to the placebo, for most network pairs (Figure 1.10). These results suggested that FC networks hence become less differentiated from each other in the psychedelic state. Interestingly, a separate analysis of the same fMRI dataset showed that the mean variance of the *internal* synchrony of nine canonical resting brain networks for the sample was increased under psilocybin, suggestive of a decrease in within-network integrity (Carhart-Harris, Leech et al. 2014). Internal synchrony was in this case defined as the extent to which the mean signal in a given network is representative of the activity in its constituent voxels.

The effects of the synthetic 5-HT_{2A} receptor agonist LSD on global communication have also been studied using fMRI. In this case, the "functional connectivity density" (FCD) of 401 even-sized regions of interest was computed as the average correlation between the BOLD signal at each region of interest and the time series from all remaining ROIs (Tagliazucchi, Roseman et al. 2016). Thus, high FCD values correspond to regions whose activity is strongly correlated to that of the rest of the brain. The analysis revealed a

significant increase in global integration, and particularly strong FCD increases in high-level cortical association regions that are rich in 5-HT_{2A} receptors, as well as the thalamus. Furthermore, the increases in global integration in some cortical association regions (angular gyrus and insula) significantly correlated with subjective reports of "ego-dissolution" under the influence of the drug (Tagliazucchi, Roseman et al. 2016).

Another time-averaged functional connectivity analysis by Petri and colleagues examined changes in the *homological scaffolds* of functional brain networks under psilocybin (Petri, Expert et al. 2014). The detailed methodology for deriving scaffolds from the persistent homology of fMRI data will be described in Chapter 2; in brief, scaffolds capture the edges' contributions to closed paths in the network topology (i.e. "cycles"). This analysis revealed that the proportion of heavy functional links between network communities was much higher in the psilocybin condition compared to a placebo, suggesting greater cross-modular integration in the psychedelic state (Figure 1.10). This functional architecture could therefore support a less constrained and more intercommunicative mode of brain function, consistent with subjective reports of the nature of consciousness in the psychedelic state.

A small number of studies have also begun to examine the effects of serotonergic psychedelics on the temporal properties of brain signals and dynamical functional connectivity in small networks. Tagliazucchi and colleagues notably assessed changes dynamical functional connectivity post-psilocybin infusion within a simple *a priori* bilateral hippocampal/ACC network (i.e. four regions of interest that had showed significant increase of BOLD signal variability under the drug) using a sliding window approach with partial correlation analysis (Tagliazucchi, Carhart-Harris et al. 2014). The probability distribution of a series of 64 possible discrete connectivity states ($n = 4^4$) was generated and Shannon's entropy was then computed. Entropy in this system's dynamical behavior was significantly enhanced by psilocybin across the range of sliding window lengths under study. Furthermore, the authors reported a greater diversity of connectivity motifs was observed after psilocybin (i.e. the presence of new connectivity states unexplored in the placebo condition). Thus, while the network under consideration in this analysis purposely included only four regions of interest to limit the total possible number of combinations of FC states, the results provided preliminary evidence for an expansion of the brain's dynamical repertoire in the brain under psilocybin.

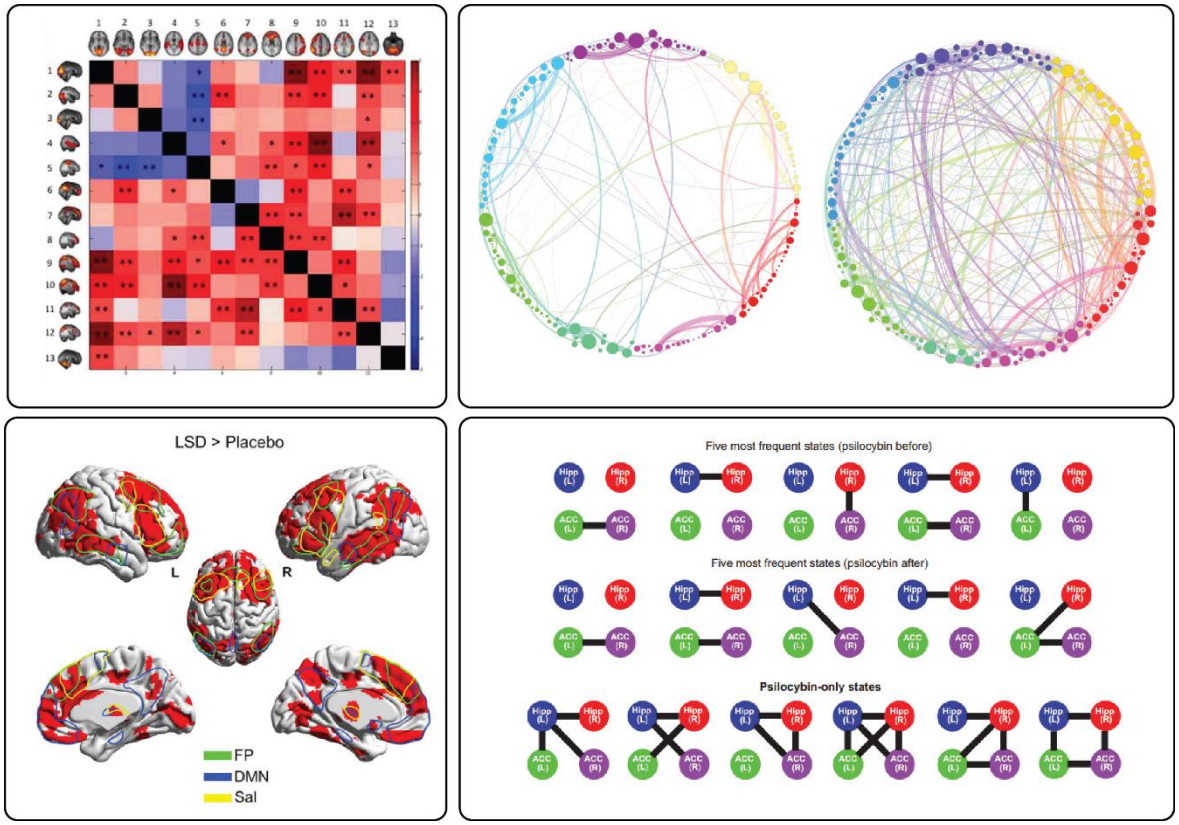


Figure 1.10. Neuroimaging evidence for increased global communication and metastability in the psychedelic state. Top left: *Between-network functional connectivity is significantly increased across most pairs of canonical resting-state networks in the psilocybin condition relative to the placebo (adapted from Roseman, Leech et al. 2014).* Top right: *Homological scaffolds of functional brain networks reveal a greater proportion of heavy links between network communities in the psilocybin condition, suggesting greater cross-modular integration (Petri, Expert et al. 2014).* Bottom left: *Functional connectivity density (FCD), defined as average correlation between the BOLD signal at each region of interest and the time series from all remaining ROIs, is significantly increased by the 5-HT$_{2A}$ receptor agonist LSD. Coloured outlines represent the bilateral frontoparietal, salience, and default-mode resting-state networks. overlaid on top of the map of FCD significant increases (Tagliazucchi, Roseman et al. 2016).* Bottom right: *Psilocybin expands and changes the dynamical repertoire within a small* a priori *network of brain areas comprising the bilateral ACC and hippocampi, as estimated by a sliding window analysis of fMRI data and partial correlation of the relevant timecourses (adapted from Tagliazucchi, Carhart-Harris et al. 2014).*

Another study recently investigated the effects of the 5-HT$_{2A}$ agonist LSD on the brain's dynamical repertoire in whole-brain networks. Atasoy and colleagues used a novel "connectome-specific harmonic decomposition" method where a succession of discrete connectome harmonics derived from the anatomical connectome (i.e. Laplacian eigenvectors of the structural connectivity matrix) served as "building blocks" of brain activity over time (Atasoy, Roseman et al. 2017). Each harmonic corresponds to a spatial pattern corresponding to a different temporal frequency oscillation on the anatomical connectome (Atasoy, Donnelly et al. 2016, Atasoy, Deco et al. 2018). This allowed for a frequency-specific decomposition of the fMRI data for the first time in the spatial domain (i.e. an approach analogous to using sine and cosine functions to decompose a signal via the

Fourier transform in the time domain). The results showed that not only did more brain states (i.e. active harmonics) contribute to neural activity under LSD leading to an expanded repertoire of dynamics, but LSD also increased the total energy of brain activity by significantly increasing the activity of high frequency harmonics. Finally, a MEG analysis investigated spontaneous signal diversity at psychoactive doses of psilocybin and LSD (Schartner, Carhart-Harris et al. 2017). Since MEG data have far higher temporal resolution than fMRI, it is therefore more amenable to signal diversity analyses. The Lempel-Ziv complexity measure was employed to study MEG signal complexity. This measure quantifies the number of distinct patterns present in the data and thus the compressibility of brain signals. Both LSD and psilocybin yielded scores of signal diversity exceeding those for normal waking consciousness (Schartner, Carhart-Harris et al. 2017)

Taken together, the aforementioned neuroimaging findings from time-averaged functional connectivity analyses of fMRI data suggest that psychedelics may work by modulating the brain's functional architecture in a manner promoting global integration at the expense of within-network integrity. From a dynamical viewpoint, the available evidence indicates that serotonergic psychedelics both expand the brain's dynamical repertoire and increase the spatiotemporal complexity of brain activity.

1.4 Sleep Stages, Mechanisms and Neuroimaging

1.4.1 Neuroscience of Sleep: A brief Overview

Arguably the most commonly experienced change in consciousness level occurs as we drift off into dreamless sleep and become unable to meaningfully interact with the external world. Sleep is medically defined as: "a natural periodic state of rest for the mind and body, in which the eyes usually close and consciousness is completely or partially lost, so that there is a decrease in bodily movement and responsiveness to external stimuli" (Stedman 1949). Historically sleep was regarded a passive state in which the brain would, "by default", promote behavioral quiescence in absence of external stimuli; however sleep is now widely accepted as an active process in the brain.

Polysomnography ("sleep study") may be used to divide sleep into distinct stages by measuring a combination of parameters during including: brain activity (scalp EEG), eye movements (EOG), skeletal muscle activation (EMG) and heart rhythm (ECG). A consensus-based classification of sleep into stages is possible due to the fact that this set of physiological variables co-vary in characteristic patterns as a function of vigilance

(Rechtschaffen 1968, Berry, Brooks et al. 2012). On the basis of these recordings, sleep may be categorized into two main components: rapid-eye-movement (REM) sleep and non-REM (NREM) sleep. As the name implies, REM sleep is characterized by random and rapid movements of the eyes, complete skeletal muscle atonia (except eye, ear and respiratory muscles) and increased respiration rate. The EEG signature of REM sleep consists of rapid, low amplitude, desynchronized neural oscillations that are theta-band dominant (4-7 Hz) with higher frequencies intermixed. This is overall similar to EEG oscillations measured during wakefulness albeit exhibiting different spatiotemporal coherence patterns (Monti, Pandi-Perumal et al. 2008). Dreaming has long been associated with REM sleep activity (Aserinsky and Kleitman 1953).

On the other hand, NREM sleep can be further divided into four stages (I-IV) associated with increasing arousal thresholds, as it becomes progressively more difficult to wake someone in the "deeper" stages of NREM sleep (i.e. stages III and IV) (Carskadon and Dement 2005). NREM stages III and IV are indeed often grouped together as "slow-wave sleep" (SWS) and characterized by slow, high-amplitude with a main frequency component in the delta range (1-4 Hz) (Pace-Schott and Hobson 2002). In SWS, eye movements, heart rate, respiration and muscle tone are all decreased relative to wakefulness, but complete muscle atonia does not occur as in REM sleep (Carskadon and Dement 2005). When polysomnography is scored over a full night, succession of sleep stages stages over time is referred to as a hypnogram, which describes the sleep architecture over time. The distribution of REM and NREM sleep stages changes over the course of sleep with SWS being more prevalent early in the night, and REM sleep epochs becoming longer near the end of sleep (Figure 1.11). Slow-wave sleep (SWS) is particularly relevant to us here, as fMRI data from a cohort of healthy adults in NREM stage III (N3) were analyzed in Chapters 3 and 5 of this Thesis. The neurobiological mechanisms underlying deep sleep (i.e. NREM stages III and IV) notably involve two nuclei of the hypothalamus (median preoptic nucleus and ventrolateral preoptic nucleus) which contain the inhibitory neurotransmitters GABA and galanin. These neuronal populations have strong sleep-inducing effects by suppressing the activity of "wake-promoting areas" in the brainstem which make up ascending arousal pathways. These wake-promoting nuclei innervate the thalamus and cerebral cortex; and include the locus coeruleus, reticular formation and raphe nucleus, all of which contain monoaminergic neurons (Saper, Fuller et al. 2010). Please note that the sleep and wake-promoting neuronal populations are intricately coupled through mutual inhibitions, which is

believed to help stabilize cortical brain dynamics into specific sleep stages as well as coordinate the transitions between them (Saper, Fuller et al. 2010).

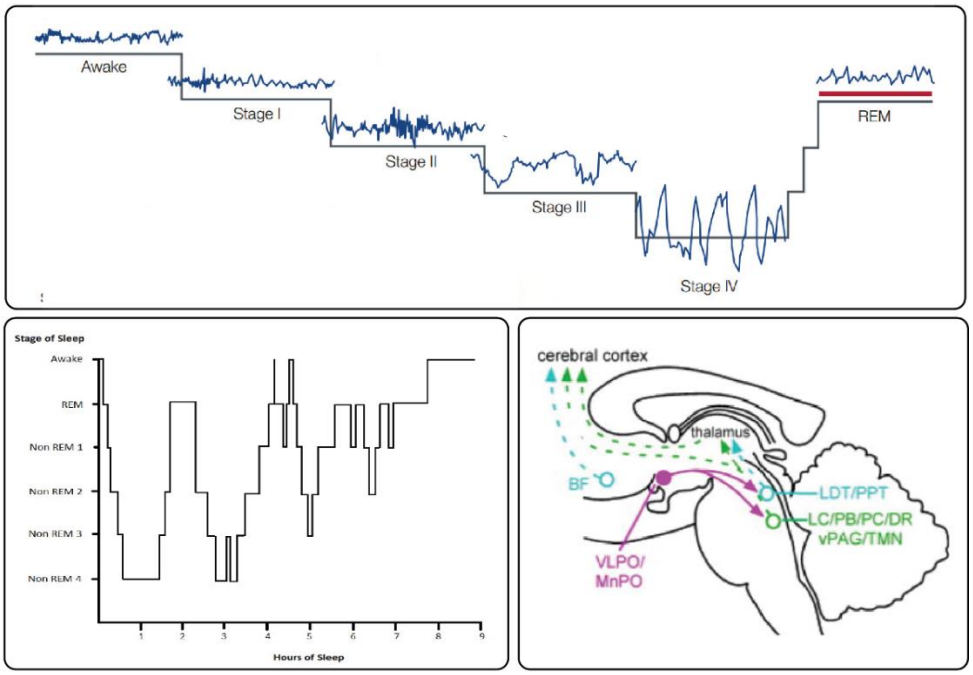


Figure 1.11. Overview of sleep stages and NREM sleep regulation. Top: *Electrophysiological signatures (EEG) of different sleep stages which make up a single sleep cycle. Of particular note, REM sleep is characterized rapid, low amplitude oscillations (theta-band dominant: 4-7 Hz) with higher frequencies intermixed) somewhat similar to those observed during wakefulness. On the other hand, the four NREM sleep stages (I-IV) are characterized by progressive dominance of the EEG by high-voltage, low-frequency wave activity with main frequencies in the delta-range (1-4 Hz) (adapted from Pace-Schott and Hobson 2002).* Bottom left: *Hypnogram readout, which describes the sleep architecture of a healthy adult by scoring polysomnography over a full night. Left undisturbed sleep typically cycle through NREM and REM about 5 times. The distribution of REM and NREM sleep changes over the course of sleep with SWS being more prevalent early in the night while REM sleep epochs are extended toward the end of the night.* Bottom right: *Summary of the neurobiology of NREM sleep promotion. Hypothalamic nuclei rich in GABAergic neurons (i.e. median preoptic nucleus and ventrolateral preoptic nucleus) inhibit the wake-promoting areas in the brainstem which make up ascending arousal pathways (adapted from Saper, Fuller et al. 2010).*

1.4.2 Neuroimaging investigations of Slow-Wave Sleep

In this section, I outline selected neuroimaging findings that are particularly relevant to our understanding of the integration/segregation balance in the deepest stages of sleep. That is, NREM stages III and IV, which are traditionally considered together as 'slow-wave sleep' (SWS).

Several PET studies have shown that brain metabolism and blood flow are overall reduced in slow-wave sleep relative to wakefulness (during some periods by as much as 40%), reflecting widespread decreases in the energetic requirements of synaptic transmission (Braun, Balkin et al. 1997, Maquet, Degueldre et al. 1997, Nir, Massimini et al. 2013). Subcortically, activity decreases are usually most pronounced in the thalamus and

to a lesser extent in the basal ganglia. At the cortical level, key hubs and association areas including the dorsolateral prefrontal cortex, orbitofrontal and anterior cingulate cortex show important reductions in activity. Moreover, the parietal cortex, precuneus and posterior cingulate cortex, as well as medial temporal cortex also show relative deactivations. By contrast, the primary sensory areas (i.e. visual, auditory, somatosensory cortices) are not deactivated compared to wakeful rest (Nir, Massimini et al. 2013) (Figure 1.12).

At the network-level, a surprising result is the relative preservation of resting-state networks (RSN's) during slow wave sleep, which seems at odds with the aforementioned metabolic decreases, electrophysiological changes and the loss of behavioral responsiveness and cognition characterizing SWS (Larson-Prior, Zempel et al. 2009, Tagliazucchi, von Wegner et al. 2013). That higher-order RSN's believed to support complex operations during wakeful cognition persist even in the deepest states of sleep was therefore unexpected. Further studies however showed that even though higher-order RSN's such as the DMN and fronto-parietal control system could be found using ICA during SWS, their internal functional connectivity strengths were significantly reduced. Notably, decreased connectivity between frontal and parietal brain regions within the DMN during SWS has been interpreted as a sign of decreased top-down communication (Baars 2005, Tagliazucchi, Behrens et al. 2013). Other studies have instead tracked changes in *whole-brain* functional connectivity during SWS relative to wakefulness using fMRI, which may be further described using graph theoretical methods. In the first study of this kind, Spoormaker and colleagues showed that widespread reductions in functional connectivity differentiated SWS from both wakefulness and the lighter NREM sleep stages across a network counting 90 cortical and subcortical brain regions (Spoormaker, Schröter et al. 2010). These findings were later corroborated by Tagliazucchi & Laufs who studied large-scale functional connectivity patterns for EEG-defined sleep stages and also found a global reduction in functional connectivity in SWS relative to wakeful rest in a slightly larger network (Tagliazucchi and Laufs 2014) (Figure 1.12). Moreover, recent unpublished analyses from our group have quantified the transition probabilities between different functional connectivity states across the vigilance spectrum using a hidden Markov model of fMRI, representing one of the first attempts at the dynamical functional connectivity mapping of neuroimaging data during sleep using unsupervised learning (Stevner 2017).

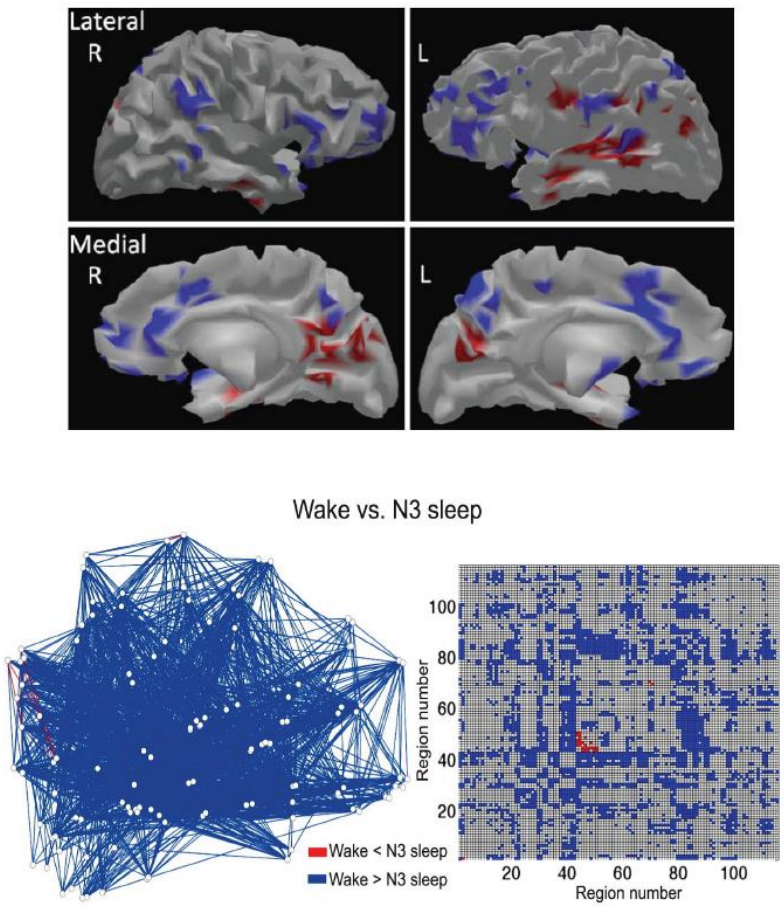


Figure 1.12. Brain metabolism and functional connectivity differences between SWS and wakefulness. Top: *A meta-analysis of PET results during SWS revealed overall decreased (blue) brain metabolism relative to wakefulness in several brain regions including (but not limited to): dorsolateral prefrontal cortex, orbitofrontal, anterior and posterior cingulate cortices. Red areas denote preserved activity in areas including visual, somatosensory, and auditory cortices (adapted from Nir, Massimini et al. 2013).* Bottom: *Significantly different (Bonferroni-corrected) functional connections between SWS and awake state shown as a graph and in matrix form. It can be observed that widespread decreases in FC occur in N3 sleep relative to baseline (adapted from Tagliazucchi and Laufs 2014).*

Particularly relevant to the integration/segregation balance are investigations of modular changes in the brain's functional architecture during SWS. Through iterative optimization, a whole-brain network may be parted into individual modules characterized by strong internal connectivity and comparatively weaker between-module connectivity (Newman 2006, Sporns and Betzel 2016). A network's modularity hence refers to the extent to which it can be split into distinct modules, and may therefore be interpreted as a measure of functional segregation. As described in Section 1.1, healthy structural and time-averaged functional brain networks display modular structure where densely connected subsets of nodes are sparsely connected between them (Sporns and Betzel 2016). Studies have therefore used fMRI to examine the relationship between measures of modularity and SWS. Boly and colleagues were the first to test the hypothesis that NREM sleep is associated with

increased modularity of brain activity. The authors notably computed the "functional clustering ratio" of six resting-state networks identified on the wakefulness data using ICA on time-averaged functional connectivity data. This measure considers the proportion of interactions within each subsystem, relative to between them (Boly, Perlbarg et al. 2012). Significant increases in functional clustering ratio were found in each of the six networks under study. An increase of functional clustering ratio suggests that the architecture of the system is modified such that individual brain modules become more independent from one another. A limitation of this analysis, however, is that all stages of NREM sleep were combined together, whereas they are characterized by distinct EEG signatures and, behaviorally, awakenings from light sleep are more frequently characterized by recollections of vivid hypnagogic hallucinations than in SWS (Siclari, LaRocque et al. 2013). A separate analysis quantified changes in brain modular structure of fMRI data during the gradual loss of vigilance which accompanies the descent into SWS (Tagliazucchi, Von Wegner et al. 2013). Time-evolving functional networks were constructed using a sliding window approach and modularity was computed for each derived FC matrix by applying the Louvain algorithm. In parallel, EEG delta power (1-4 Hz) was temporally averaged within the same sliding windows. Using this approach, the authors reported increased functional segregation with the onset of N3 sleep, which quickly decreased after awakening from deep sleep. Moreover, the breakdown of the integration between functional modules during N3 was closely paralleled by increases in EEG delta power (Tagliazucchi, Von Wegner et al. 2013) (Figure 1.13).

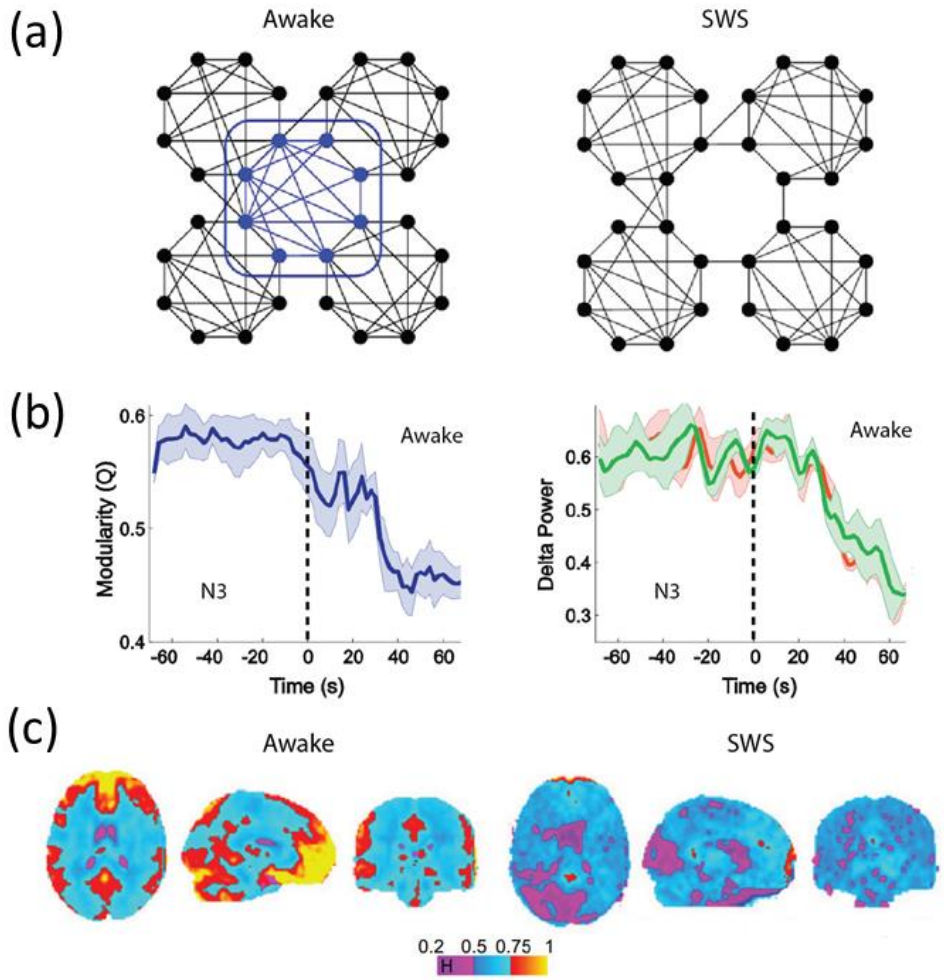


Figure 1.13. Modularity and temporal complexity of brain activity changes in slow-wave sleep (SWS). (a) *Schematic representation of the increase in FC network modularity reported in SWS relative to wakefulness; reflecting a functional architecture which promotes the segregation of information processing (Boly, Perlbarg et al. 2012, Tagliazucchi, Von Wegner et al. 2013).* (b) *During transitions between N3 sleep and wakefulness, dynamic functional connectivity networks constructed using a sliding-window approach on fMRI data show a significant decrease in modularity when study participants awake from SWS (left) with a concurrent decrease in delta band power (right) (adapted from Tagliazucchi, Von Wegner et al. 2013).* (c) *During the descent into deep sleep, global decreases in the Hurst exponent suggest that BOLD signals gradually shift to short-range temporal correlations reflecting a loss of complexity and coordination of the underlying neural dynamics, particularly in fronto-parietal areas (Tagliazucchi, von Wegner et al. 2013).*

The dynamic brain changes associated with SWS have also been investigated at the regional and voxel levels. Notably, the same measure of spatiotemporal complexity introduced earlier (Lempel-Ziv complexity) which reflects the compressibility of a binarized signal was applied to both scalp and intracranial EEG in separate studies that each found a significant reduction on this measure in SWS relative to the wakefulness baseline, providing further evidence that the level of consciousness correlates with neural dynamical complexity (Andrillon, Poulsen et al. 2016, Schartner, Pigorini et al. 2017). Furthermore, Tagliazucchi and colleagues investigated changes in the voxel-wise distribution of the Hurst exponent of

BOLD signals in NREM sleep stages and wakefulness (Tagliazucchi, von Wegner et al. 2013). The Hurst exponent is a measure of long-range temporal dependence of a signal, or "self-similarity". The Hurst exponent of a time-series ranges between 0–1 range where values between 0.5 and 1 indicate more low-frequency content, greater persistence over time, a smoother time-series and longer memory. Values between 0 and 0.5, on the other hand, indicate greater high-frequency content and a value of 0.5 indicates a random walk. Higher values of Hurst exponent and thus greater signal persistence are thought to reflect more complex and coordinated dynamics in the underlying network activities (Ball, Stokes et al. 2011). Widespread decreases were found in the Hurst exponent in N3 sleep compared to baseline. BOLD signals gradually shifted to short-range temporal correlations in the descent to deep sleep, and the reduction was particularly pronounced in fronto-parietal areas, thus reflecting a loss of signal memory and complex temporal processing during SWS (Tagliazucchi, von Wegner et al. 2013) (Figure 1.13).

Finally, another experiment described earlier in Section 1.2 investigated the integration/segregation balance during SWS using combined TMS-EEG to perturb a subset of cortical neurons and quantify the response to this initial activation across the rest the brain with millisecond temporal resolution (Massimini, Ferrarelli et al. 2005) (Figure 1.8). As explained earlier the findings suggested that, even though some canonical resting-state networks are maintained during SWS, brain networks generally lose their ability to sustain long-range causal interactions as the system breaks down into segregated modules (Massimini, Ferrarelli et al. 2005, Nir, Massimini et al. 2013).

1.5 Summary of the Argument

The neuroimaging and computational modelling studies reviewed above have provided valuable insights about the integration/segregation balance in the human brain (Section 1.1). I have notably established that functional network connectivity and associated integration and segregation measures fluctuate over both space and time. I have also presented evidence that the integration/segregation balance likely results from complex synergistic interactions between the anatomical connectome and the excitability of local neuronal populations (i.e. E/I ratio). Furthermore, I have summarized two important theoretical accounts of consciousness (dynamic core theory and information integration theory) which suggest that the co-occurrence of integration and differentiation in neural dynamics underlies the phenomenology of consciousness, thereby linking the processing of conscious scenes to the balanced integration and segregation of information in functional

brain networks (Section 1.2). This implies that behaviorally-relevant changes in consciousness level and/or content should be accompanied by dynamical changes in the brain's integration/segregation balance.

The neuroimaging literature on the rapid and reversible changes in consciousness induced by serotonergic psychedelics (Section 1.3) and slow-wave sleep (Section 1.4) has followed a similar progression. Initial studies measured changes in regional brain metabolism and in time-averaged functional connectivity within small, *a priori* networks. Later studies investigated functional connectivity at the whole-brain scale, and analyzed distributed networks using graph theoretical measures. More recently, some authors have applied spatiotemporal complexity measures to local brain signals in both sleep and psychedelics neuroimaging datasets.

Graph theoretical analyses of *time-averaged* functional connectivity networks and the application of neural signal complexity measures to functional neuroimaging data have indeed begun to reveal interesting contrasts between the integration and segregation of information in slow-wave sleep and the psychedelic state, relative to wakeful rest. Notably, NREM sleep stages III and IV have been associated with significant increases in modularity and reductions the temporal complexity of the associated brain signals relative to wakefulness (Section 1.4). Conversely, functional connectivity studies of the serotonergic psychedelics psilocybin and LSD have found that cross-modular communication is instead facilitated by these compounds, and the complexity of the source signals are enhanced.

What remains largely unclear, however, is whether and how the integration/segregation balance is *dynamically* altered in slow-wave sleep and in the psychedelic state. Importantly, such questions cannot be addressed via time-averaged functional connectivity analyses which do not account for the temporal evolution of brain network properties. Moreover, they cannot be addressed by strictly analyzing signal complexity measures at the source level as these calculations, albeit informative, do not directly capture the interactions between different brain regions over time. Therefore, the dynamical aspects of the integration/segregation balance in altered states of consciousness at the whole-brain scale have remained almost entirely unexplored, and represent the central focus of this thesis.

In Chapter 2, our exploration of the integration/segregation balance in the human brain begins by introducing a novel measure for identifying highly integrative nodes in time-

averaged brain networks based on the persistent homology of resting-state fMRI data. In Chapter 3, we move on to examine dynamical changes in the integration/segregation balance in both the psychedelic state and slow-wave sleep by examining *global* measures of functional network synchrony, metastability and chimeraness. Chapter 4 then leverages on a novel methodology for measuring the occurrence and transition probabilities of functional network states over time to reveal changes in the brain's dynamical repertoire in subjects administered with the classical psychedelic psilocybin. Finally, in Chapter 5, I employ a novel framework of "intrinsic ignition" to characterize the tendency of brain areas to dynamically broadcast regional activity signals either locally or globally in both slow-wave sleep and in the psychedelic state.

Chapter 2: Regional contributions to global integration: novel insights from the homological scaffolds of functional connectivity networks[2]

2.1 Introduction

The application of graph theoretical analysis to neuroimaging data has provided important new insights about the functional organization of the human brain in health and disease. Graph measures have notably helped shape our understanding of the system-wide functional architectures which enable the brain to balance the segregation and integration of information in macro-scale networks (see Introduction 1.1.1).

Whilst standard graph metrics are powerful descriptive means to characterize functional neuroimaging data at the whole-brain scale, they also involve significant conceptual and methodological limitations. First, these measures are exclusively based on *dyadic* (i.e. pairwise) interactions between edges and vertices. In practice, this means that the basic "unit" of the graph is an edge connecting a pair of nodes. By contrast, it is well established that neural computations performed by *distributed* ensembles of brain regions underlie higher cognitive phenomena and resting-state dynamics in the human brain. Moreover, *ad hoc* thresholding methods are commonly employed in functional connectivity studies to selectively prune connections within the graph leading to sparser, binary network representations with more naturally interpretable attributes. A majority of these strategies lead to the elimination of *weak and/or negative* connections within a network, yet it has been demonstrated that standard graph measures are unstable across the threshold ranges typically employed in functional connectivity studies (Garrison, Scheinost et al. 2015) and very few neuroimaging analysis methods actually account for the statistical significance of individual connections (Lord, Allen et al. 2011, Lord, Allen et al. 2012, Pandit, Expert et al. 2013). Thus, while neglecting weak links enhances information clarity, it may well do so at the expense of information completeness (Granovetter 1977).

[2] Some of the materials presented in this Chapter were published in: *Lord LD, Expert P, Fernandes HM, Petri G, Van Hartevelt TJ, Vaccarino F, Deco G, Turkheimer F, Kringelbach ML. Insights into brain architectures from the homological scaffolds of functional connectivity networks. Frontiers in systems neuroscience. 2016 Nov 8;10:85.*

An alternative to traditional network analysis methods is the use of the *homological scaffold* of the weighted network (Petri, Expert et al. 2014) to summarise information about the persistent homology of the data. Persistent homology is a recent technique in computational topology (Munkres 1984, Cohen-Steiner, Edelsbrunner et al. 2005, Zomorodian and Carlsson 2005) that will be described in detail below. In summary, homology characterizes a topological space by counting its *holes* of different dimensions. Persistent homology characterizes the importance and stability of the holes in the original data through a process called *filtration*, which does not rely on *a priori* thresholding of the adjacency matrix. It is accordingly a specific type of *mesoscopic organization* of the vertices and edges and their respective importance that is considered in the persistent homology analysis. This enables one to explore the network's organization from a non-dyadic perspective, consistent with the brain's large-scale ensemble coding mechanisms. Holes are the mesoscopic (anti-)structures remaining in the topological space that are not bounding a higher dimensional simplex. The case of 1-dimensional holes, or "cycles" is intuitive to visualize; a cycle is a closed loop of length greater than three (Figure 2.1). The homological scaffold summarizes the role of network edges constituting the cycles during the filtration process and therefore enables us to identify edges belonging to multiple cycles and/or highly persistent cycles along the filtration.

The network organization of the human brain is characterized by a large number of distributed network modules which perform segregated local computations (Power, Cohen et al. 2011, Sporns 2013). There has recently been much interest towards identifying the "hub" regions which enable global communication across segregated brain modules, and the integration of these local computations over space and time (see Introduction 1.1.1). The main hypothesis tested in the present analysis is that the edges supporting highly persistent cycles (and that therefore have strong weights in the persistence homological scaffold) will be well positioned to bridge together segregated functional brain modules, rather than participate in densely connected local networks. To investigate this, I generated a persistence scaffold from the whole-brain functional connectivity data of healthy subjects recorded during resting-state fMRI. I then converted edge-persistence scaffold values into a *node-level* measure termed *persistence scaffold strength* (*PSS*) which enables comparisons between the persistence scaffold and standard graph metrics computed on the original network.

2.2 Methods

Study Participants

Neuroimaging data were collected at CFIN, Aarhus University Hospital, Denmark, from 16 healthy right-handed participants (11 men and 5 women, mean age: 24.7±2.5). Participants with a history of psychiatric or neurological disorders were excluded from participation in the study. The study was previously approved by the Center of Functionally Integrative Neuroscience internal research board. The study was performed in accordance with the Declaration of Helsinki ethical principles for medical research and ethics approval was granted by the Research Ethics Committee of the Central Denmark Region (De Videnskabsetiske Komiter for Region Midtjylland). Informed consent was obtained from all participants.

MRI data acquisition & Processing

MRI data were collected in one session on a 3T Siemens Skyra scanner. The parameters for the structural MRI T1 scan were as follows: voxel size of 1 mm^3; reconstructed matrix size 256x256; echo time (TE) of 3.8 ms and repetition time (TR) of 2300 ms. The resting-state fMRI data were collected using whole-brain echo planar images (EPI) with TR = 3030 ms, TE = 27 ms, flip angle = 90^o, reconstructed matrix size = 96x96, voxel size 2x2 mm with slice thickness of 2.6 mm and a bandwidth of 1795 Hz/Px. Seven minutes of resting state fMRI data were acquired for each subject.

I used the automated anatomical labeling (AAL) template (Tzourio-Mazoyer, Landeau et al. 2002) to parcellate the entire brain into 90 cortical and subcortical regions (45 for each hemisphere) which represented the nodes in functional connectivity networks. The parcellation was conducted in the EPI native space. Linear registration was performed using the FSL toolbox (www.fmrib.ox.ac.uk/fsl, FMRIB, Oxford) (Smith, Jenkinson et al. 2004). The EPI image was co-registered to the T1-weighted structural image, and the T1-weighted image was co-registered to the T1 template of ICBM152 in MNI space. The resulting transformations were concatenated and inversed and further applied to warp the AAL template from MNI space to the EPI native space, where interpolation using nearest-neighbor method ensured that the discrete labelling values were preserved. Initial fMRI data preprocessing was carried out using FEAT (FMRI Expert Analysis Tool) Version 6.00 (part of FSL) and consisted of: motion correction using MCFLIRT; non-brain tissue removal using BET; spatial smoothing using a Gaussian kernel of FWHM 5mm; grand-mean

intensity normalisation of the entire 4D dataset by a single multiplicative factor; high pass temporal filtering (Gaussian-weighted least-squares straight line fitting, with sigma = 50.0s).

I used FSL to extract and average the time courses from all voxels within each AAL cluster. Matlab (The MathWorks Inc.) was used to compute the pairwise Pearson correlation between all 90 regions. *R*-values were transformed to *z*-values via Fisher transformation, and the resulting *z*-values composed the final 90x90 functional connectivity (FC) matrix. The FC matrices were averaged for all 16 participants to obtain a group-averaged 90x90 FC matrix.

2.2.1 Persistent Homology and Scaffolds

A *simplicial complex* can be seen as a generalization of a graph, where interactions, instead of being strictly between nodes, are between objects called *simplices* that generalize the notion of nodes. In the present context, a node is a 0-dimensional simplex, an edge a 1-dimensional simplex, (representing a binary interaction between vertices) a full triangle is a 2-dimensional simplex (representing ternary interactions), and so on for higher dimensions. A simplicial complex is thus a type of topological space that is a collection of simplices of any dimension **(Figure 2.1).**

There are many types of simplicial complexes. This study focuses on *clique complexes*, which can be constructed from any network. In graph theory, a *clique* is a subset of vertices of a graph in which every pair of vertices is adjacent. Thus a *k*-clique is a completely connected subgraph $K_k \subset G$, composed by *k* nodes containing all the possible edges among its nodes. When representing a simplicial complex, simplices are typically shaded, or filled in to identify them. Importantly, upon identifying all the simplices in a clique complex, structures called *holes* can remain, and these are the structures of interest in this analysis (Figure 2.1). A hole of dimension *k*, or *k*-hole, is a hole bounded by simplices of dimension *k*.

This analysis focuses on holes bounded by 1-dimensional boundaries, also called "cycles". In a clique complex, a cycle is a minimal closed path of length greater than 3 (Figure 2.1). This is due to the fact that each clique corresponds to a full simplex so that a triangle is filled in. The set of *k*-holes defining a space is described by the *k*-th homology group H_k. Each k-hole i is in turn represented by its generator $g_i^k \in H_k$. Informally, generators are formed of elements of H_k that identify and can be used to construct the hole.

Thus, in summary, a clique complex can be described by its holes, and a cycle is a hole of dimension 1.

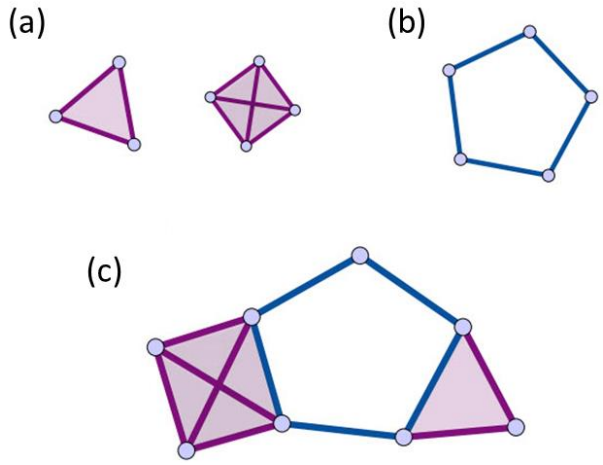


Figure 2.1. Illustrations of cliques, simplices, holes and clique complex. (a) *3 and 4-cliques, which are associated to 2 and 3-dimensional simplices.* (b) *a 1-dimensional hole, or cycle, is a closed path of edges of length greater than 3.* (c) *Combining the elements of (a) and (b) one can produce a clique complex with one 1-dimensional hole. All simplices in this figure are shaded as is customary.*

One of the most studied problems in mathematics is that of defining a notion of similarity between spaces. Intuitively, two spaces can be thought to be similar if we can transform one into the other via a well-behaved transformation. In particular, if there exists a continuous bijective map (homeomorphism) that transforms one space into the other, then the two spaces are said to be homeomorphic. Such spaces are, informally, topologically the same, and any of their properties that are conserved by homeomorphism are are thus called *topological invariants*.

The homology group, or simply *homology*, is a property of a space which is based on the counting of holes and their associated dimensions. As an analogy to homology, the reader can think of *The Hound of the Baskervilles* by Sir Arthur Conan Doyle, where the non-manifestation of the hound one night was as informative to Sherlock Holmes as its presence. Homology is a topological invariant which, as explained above, means that it is a property of a space that is preserved by homeomorphisms and keeps the same value whatever the representation of the system. Thus, if two spaces have the same homology, then they are topologically equivalent.

The process of adding simplices to form a simplicial complex is called a filtration, and the filtration used here is the *weight clique rank filtration* (Petri, Scolamiero et al. 2013).

It has been specifically designed to extract homological features from fully connected, weighted and signed networks. The filtration starts with a set of disconnected nodes. Then all the edges from the original network are sorted in *descending* order of magnitude and added one by one as 1-simplices to the complex. After each addition, the clique complex is constructed and its persistent homology computed. When a new cycle appears, it is tagged with a "birth time", β_i and when it disappears, it is tagged with a "death time", δ_i. The difference between the two time points defines its *persistence* π_i. It is important to note that when the starting network is fully connected, all the cycles eventually die along the filtration.

The homological scaffolds are secondary networks and were introduced as a mean to summarise part of the persistent homology of cycles information for the edges (Petri, Expert et al. 2014). As they localize the cycles on specific edges of the network, they can naturally be seen as edge centrality measures that characterize the importance of links in the original network through the filtration process, where the weights on the edges represent their centrality. In a *persistence* homological scaffold, the importance of an edge in the network reflects the total persistence of the cycles it belongs to. The weights of the edges are defined as:

$$\omega_e^p = \sum_{g_j | e \in g_j} \pi_{g_j}$$

for the persistence scaffold H_G^p, where the belonging of an edge e to a cycle generator g_j is weigthed according to the persistence of this particular cycle π_{g_j}. Therefore, the homological scaffold measures the importance of edges relative to the number of cycles they belong to and the persistence of these cycles. Therefore, scaffolds can be seen as an edge centrality measure, that emphasizes the role of an edge in the persistent homological characterization of the original data; but they can also be considered as network in itself and analyzed as such, as I define the *PSS* metric below.

Persistent homology and the computation of the scaffolds can be illustrated by a simple toy example, which is shown graphically in Figure 2.2. For simplicity, the edges with a weight of zero are not represented. The first step is the filtration: edges are added in decreasing order of strength. In the example, edges have five different weights. Accordingly, five filtration steps are needed, and five associated clique complexes are formed. There are two cycles: one born at step 2) and one born at step 3). By contrast, the edge added at step 4) does not define a new cycle. The aforementioned cycles are both killed by the addition of

the two edges at step 5). Their respective persistence and frequency are summarized in the barcode below the filtration. The resulting scaffolds are on the right of the barcode: the persistence scaffold (green) and frequency scaffold (blue).

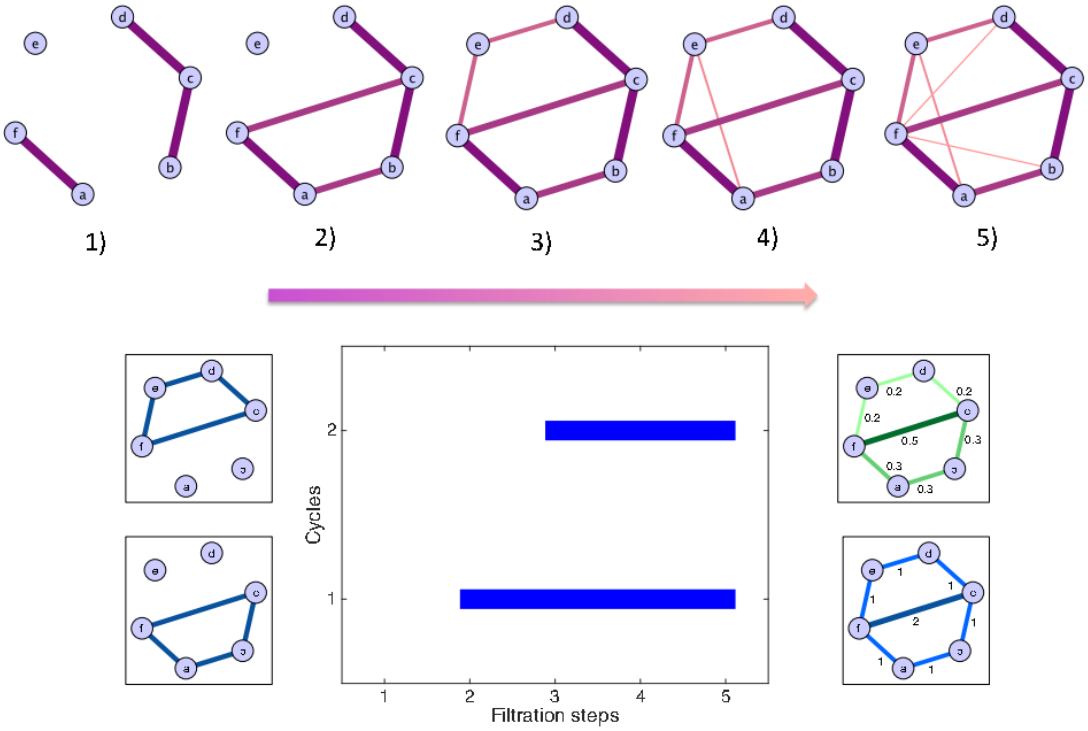


Figure 2.2. Toy example illustrating the generation of the homological scaffolds. Top***:*** *The filtration: edges are added in decreasing order of weight (thickness and colour represent the weights) to arrive at the original network at step 5).* Bottom middle: *The barcode encoding the persistence of the two cycles* $\langle abcf \rangle$ *and* $\langle cdef \rangle$. Bottom right: *The persistence (green) and frequency (blue) scaffolds, summarising the role of the edges in the cycles present during the filtration.*

2.2.2 Graph Theoretical Analysis

By construction, the networks considered for the standard graph analysis are unweighted, undirected, and do not contain self-loops. Their adjacency matrix *A* is therefore symmetric, and its elements are equal to 1 if nodes *i* and *j* are connected and zero otherwise. I applied the following standard graph metrics to the network: degree centrality (*DC*), betweenness-centrality (*BC*), local efficiency (*Eff*) and participation coefficient (*PC*). Graph theoretical analysis was performed using the *Brain Connectivity Toolbox* (BCT) in Matlab (Rubinov and Sporns 2010). These metrics each capture different aspects of the contributions of a node to the network organization. To facilitate the interpretation of standard graph metrics, functional connectivity matrices were binarized at eleven statistical thresholds that give a network link density (*D*) in the range [0.10, 0.60] in increments of 0.05, eliminating the weakest links in the network. The degree centrality is a measure of the

total number of connections that a node has. It therefore depends on the direct neighborhood of the node. For a node *j* within a binarized network comprising *N* nodes, degree centrality is defined as:

$$DC(j) = \sum_{i=1}^{N} A_{i,j}$$

The betweenness-centrality of a node measures how many of the shortest paths between all other node pairs pass through it and is a measure of its importance when routing information in the network. By contrast to the degree, *BC* is dependent of the overall topology of the rest of the network beyond the direct neighborhood of a node. For a node *k* it is defined as:

$$BC(k) = \sum_{i \neq j \neq k, i,j=1}^{N} \frac{\hat{\sigma}_{i,j}(k)}{\hat{\sigma}_{i,j}}$$

where $\hat{\sigma}_{i,j}(k)$ is the number of shortest paths going from node *i* to node *j* through node *k*, and $\hat{\sigma}_{i,j}$is the total number of shortest paths going from node *i* to node *j*.

The local efficiency (*Eff*) of a node *k* computes how well the neighbors of a node are connected together. That is, the inverse of the average shortest path length connecting the neighbors of that vertex:

$$Eff(k) = \frac{2}{Nn(n-1)} \sum_{i \in G}^{n} \sum_{i<j \in G}^{n} \frac{1}{d_{i,j}}$$

where *n* is the number of neighbors of a node *k*. In addition, a community detection algorithm based on modularity (*Louvain method with finetuning* (Blondel, Guillaume et al. 2008)) was applied to the adjacency matrix with D = 0.40, and identified six communities for the partition optimising the modularity function. The participation coefficient was then calculated for each node in this network. The participation coefficient compares the degree of a given node to nodes in all other communities with the number of links it has within its own cluster. Nodes with a high participation coefficient are therefore expected to play an important role in binding different communities together and hence contribute to global integration. This measure therefore provides additional information about a node's role in the network topology which cannot be inferred from measures of topological centrality alone. It is defined as:

$$PC_i = 1 - \sum_{c=1}^{N_C} \left(\frac{k_{C_i}}{k_i} \right)^2$$

where k_i is the degree of node i and k_{C_i} its degree limited to cluster C.

I also computed the weighted counterparts of the same three graph metrics employed in the original graph analysis described above: the nodal *strength* (weighted counterpart of degree), the weighted betweenness centrality (*wt-BC*) and the weighted local efficiency (*wt-Eff*). By definition, the computation of these measures on a fully connected weighted graph does not rely on the *ad hoc* thresholding of the FC matrix. The mathematical formulation of the weighted version of the metrics are the same as in the unweighted case. For the nodal strength, one sums up the weights of the links connected to a node:

$$SC(j) = \sum_{i=1}^{N} W_{i,j}$$

For the weighted versions of betweenness-centrality and efficiency, the difference resides in the definition of the shortest path. In the BCT implementation, the shortest path is computed via a breadth-first search algorithm that follows the links with the smallest weight.

Definition of *Persistence Scaffold Strength* and Functional Hubs

Lastly, let us define a new centrality measure for the homological scaffolds, the nodal *persistence scaffold strength* (*PSS*). It is essentially the strength of a node, i.e. the sum of the weights of its links, in the persistence scaffold H_G^p. I gave it a different name to clearly differentiate its meaning as a measure obtained from the persistent homology procedure instead of pairwise interactions between edges and vertices. It is defined as:

$$PSS(j) = \sum_{i=1}^{N} H_{G\ i,j}^{p}$$

The *PSS* thus compresses into a scalar information about the persistence of cycles passing through a given node. *The PSS thereby captures the combination of a node's central position in the network and the relative lack of connectivity amongst its local neighbourhood*. Moreover, as outlined above, the *PSS* does not rely on *ad hoc* thresholding of the functional connectivity matrix and therefore includes information from all the edges in the network (i.e. including the weakest ones). This is an important distinction between the

PSS and the topological centrality metrics traditionally measures applied to time-averaged functional neuroimaging data.

Node-level values were calculated for the *PSS* measure as well as standard graph centrality measures. As indicated above, the *PSS* does not require *a priori* thresholding of the functional connectivity matrix. However, for the computation of local graph measures (*DC*, *Eff* and *BC*), I calculated the node level metric values at each of eleven thresholds over the D = [0.10,0.60] range. First, the Pearson correlation coefficient was computed between the *PSS* and each of the aforementioned graph metrics across the FC threshold range under study. I also identified the highest ranking nodes (termed "hubs" for concision) for each of graph measure under study by taking the integral of their respective values over the threshold range. Functional hubs were defined as those nodes with a metric value larger than 1 standard deviation from the mean of their respective distribution. I then compared the hubs on each graph metric to those identified with the *PSS*.

2.3 Results

2.3.1 Relationship between nodal PSS and standard graph metrics

The main objective of this analysis was to examine the relationship between standard topological centrality measures described above; *DC*, *BC*, *Eff* and the nodal *PSS*. This was done by computing bivariate correlations between the standard graph metric values and nodal *PSS* across the threshold range applied to the functional connectivity matrix, and applying the Bonferroni correction for multiple comparisons. The Bonferroni corrected *p*-values for each analysis are listed in Table 2.1 below. It is important to note that while different FC network thresholds were used for the standard graph analysis, the input FC matrix for the persistent homology analysis did not require *a priori* thresholding, which is a potential strength of this methodology. In order to verify that the reported associations between nodal *PSS* and standard metric values at a given threshold were not simply driven by the direct connectivity of network nodes, I also examined the correlations *DC* vs *BC*, *DC* vs *Eff* and *BC* vs *Eff* as control conditions (Figure 2.3).

PSS vs DC: The positive correlation between *PSS* and *DC* was significant at all thresholds under study, although it was consistently weaker than the correlation of *PSS* vs *BC*.

PSS vs BC: The *PSS* showed strong and statistically significant positive correlations with the *BC* metric at all thresholds under study. This indicates that *PSS* is associated with a node's tendency to be part of shortest paths between node pairs in the network.

PSS vs Eff: Conversely, a strong and significant *negative* correlation was observed between the *PSS* and *Eff* metrics at all but the three lowest density thresholds, showing that high *PSS* nodes generally avoid densely connected neighborhood clusters. These results are illustrated in the top panel of Figure 2.3.

DC vs BC: By contrast to *PSS* vs *BC*, the *DC* vs *BC* correlation failed to reach statistical significance at 8 of the 11 thresholds under study. Even when the relationship did reach statistical significance, the *DC* vs *BC* correlations remained on average weaker than *PSS* vs *BC* over the same threshold range.

DC vs Eff: The *DC* vs *Eff* correlation also showed a threshold-dependent profile. Significant positive correlations were only observed at the lowest densities in the $D = [0.1, 0.15]$ range which contrasted with the *negative* correlations between *PSS* vs *Eff* observed at these same thresholds. *DC* vs *Eff* however did not reach statistical significance at any of the thresholds exceeding $D > 0.15$.

BC vs Eff: Finally, the negative correlation between the *BC* and *Eff* metrics was qualitatively similar to the *BC* vs *PSS* correlation over the threshold range. However, *BC* vs *Eff* did not reach statistical significance at the lowest network densities of $D = [0.1, 0.15]$ and the negative correlation strengths at higher densities were overall stronger for *BC* vs *Eff* than *PSS* vs *BC*. These results are graphically represented in the bottom panel of Figure 2.3.

As a follow-up analysis, the relationships between the *PSS* and the weighted counterparts of the metrics used in the original analysis were also studied. These included the nodal *strength*, weighted betweenness-centrality (*wt-BC*) and weighted efficiency (*wt-Eff*).

strength vs PSS: There was a borderline significant positive correlation between the nodal strength in the weighted network and the *PSS*: $R = 0.21$, $n = 90$, $p = 0.046$.

wt-BC vs PSS: The positive correlation between *wt-BC* vs *PSS* was stronger than *strength* vs *PSS* and highly significant: $R = 0.39$, $n = 90$, $p < 0.01$; consistent with the results of the binary graph analysis.

wt-Eff vs PSS: There was a significant *positive* correlation between *PSS* vs *wt-Eff*: $R = 0.23$, $n = 90$, $p = 0.03$. This relationship was opposite to that observed in the binary network analysis where *PSS* vs *Eff* instead showed a strong *negative* association at all thresholds under study.

For the network with an intermediate density of $D = 0.40$, a community detection algorithm was applied to the data and the participation coefficient (*PC*) was computed for each node in the network. A significant positive correlation was revealed between *PC* and *PSS*, $R = 0.32$, $n = 90$, $p < 0.01$. This indicated that the *PSS* measure also reflects the tendency of a node to act as a bridge across communities in distributed brain networks.

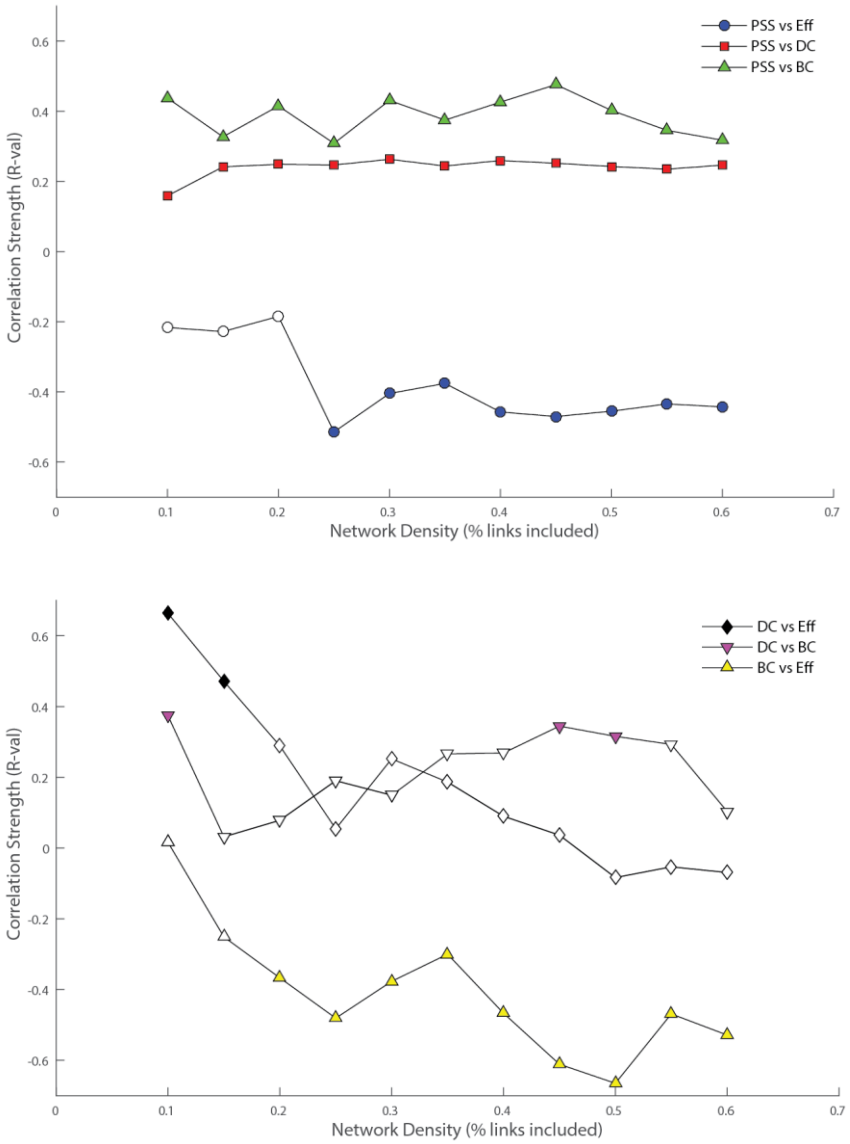


Figure 2.3. Comparison between PSS and standard graph measures. Top*: At each threshold under study, the value of the bivariate correlation coefficient (*R*) between* PSS *and each of: degree-centrality (*DC*), betweenness-centrality (*BC*) and local efficiency (*Eff*) is plotted.* Bottom*: Relationship between standard topological measures. The same procedure as above is repeated for correlations between:* DC *vs* BC, DC *vs* Eff, *and* BC *vs* Eff *as control conditions. Filled shapes indicate the presence of a statistically significant correlation between the two variables, surviving Bonferroni correction for multiple comparisons (*$p < 0.05$*).*

	PSS vs DC	PSS vs Eff	PSS vs BC	DC vs BC	DC vs Eff	BC vs Eff
D = 0.10	1.763E-04	4.452E-01	1.763E-04	3.079E-03	1.155E-11	9.671E+00
D = 0.15	1.811E-02	3.369E-01	1.811E-02	8.436E+00	3.016E-05	1.865E-01
D = 0.20	5.235E-04	8.928E-01	5.235E-04	5.087E+00	6.290E-02	4.129E-03
D = 0.25	3.403E-02	2.386E-06	3.403E-02	7.970E-01	6.724E+00	1.768E-05
D = 0.30	2.464E-04	8.412E-04	2.464E-04	1.763E+00	1.819E-01	2.767E-03
D = 0.35	3.009E-03	2.873E-03	3.009E-03	1.240E-01	8.642E-01	4.470E-02
D = 0.40	3.104E-04	6.441E-05	3.104E-04	1.149E-01	4.399E+00	3.853E-05
D = 0.45	2.320E-05	3.216E-05	2.320E-05	9.654E-03	8.061E+00	1.745E-09
D = 0.50	9.299E-04	7.299E-05	9.299E-04	2.678E-02	4.774E+00	9.661E-12
D = 0.55	9.355E-03	2.075E-04	9.355E-03	5.586E-02	6.811E+00	3.455E-05
D = 0.60	2.524E-02	1.370E-04	2.524E-02	3.665E+00	5.682E+00	9.352E-07

Table 2.1. Statistical testing results. *Corrected p-values for biavariate correlations between persistence scaffold score (PSS) and standard graph theoretical mesures across the network density range D = [0.10, 0.60], reported graphically in Figure 2.3. Bonferonni correction for multiple comparisons is applied and the reported p-values have been multiplied by the number of comparisons (11) for a given pair of metrics. Blue text indicate that a corrected p-value survives the $\alpha = 0.05$ statistical threshold, whilst red values are above this threshold.*

2.3.2 Identification of functional hubs using the *PSS* and standard graph measures

I now explain the results shown in Figure 2.4 and Figure 2.5. Functional hubs were identified on each of the *PSS*, *DC*, *Eff* and *BC* measures using the procedure outlined in section 2.3.4. Fourteen AAL regions (out of 90) were identified as hubs on the *PSS* measure. The most important overlap was observed between the *PSS*-hubs and the *DC*-hubs (5/14) and the second-most important overlap was between the *PSS*-hubs and *BC*-hubs (4/14). Please note that this was the case despite the presence of a stronger positive correlation between *PSS* vs *BC* than *PSS* vs *DC* at all the thresholds under consideration. As expected, *Eff*-hubs showed the least amount of overlap with the *PSS*-hubs, consistent with the strong negative correlation between these two measures.

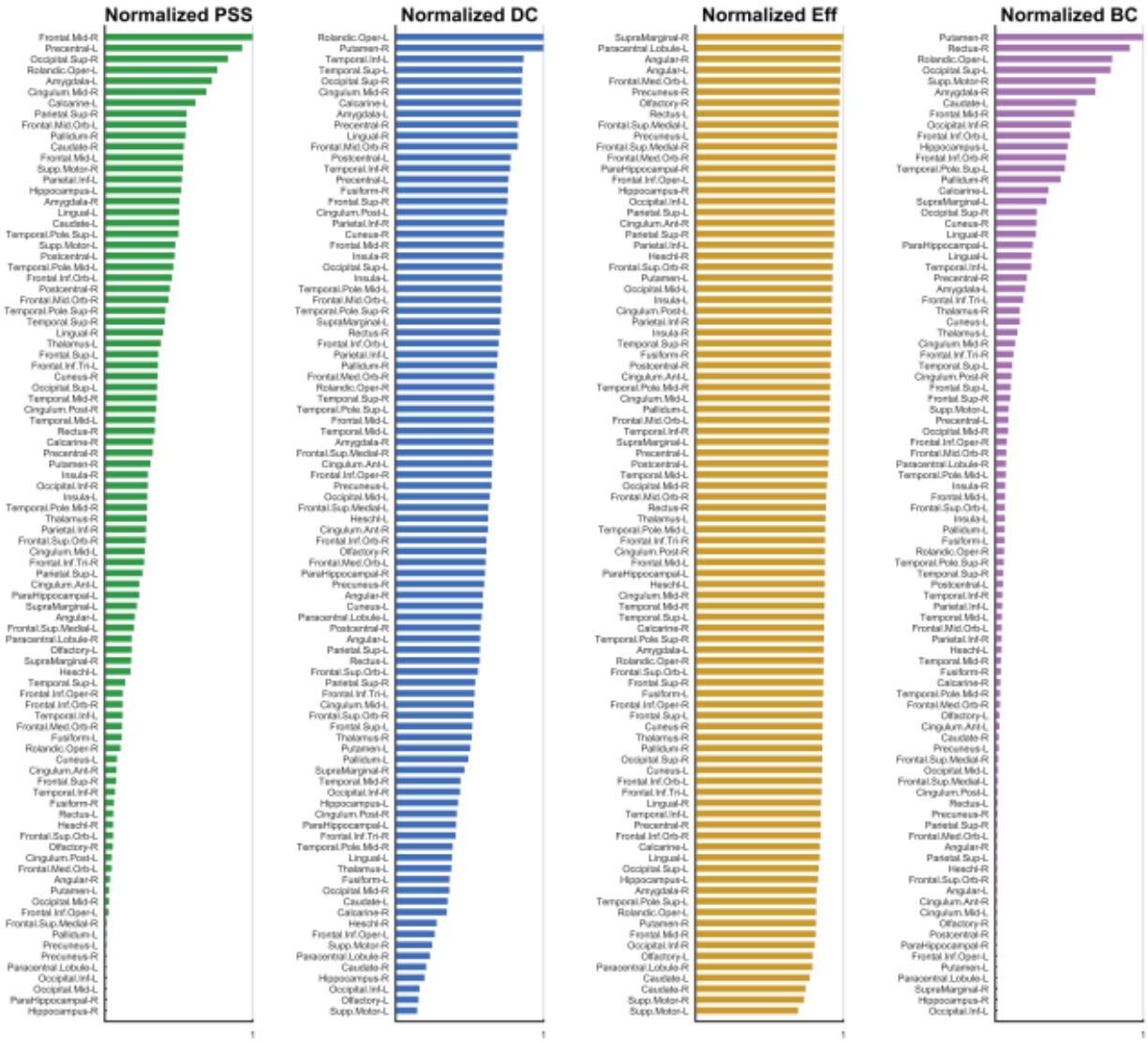


Figure 2.4. Normalized Metric Values. *The normalized nodal values are displayed for each graph measure under study. The values for* PSS, BC, DC *and* Eff *are respectively depicted from left to right. While computation of the* PSS *does not require* ad hoc *thresholding, the* BC, DC *and* Eff *metrics are threshold-dependent and nodal metric values have thus been integrated over the threshold range under study to generate a single value for each node, as described above.*

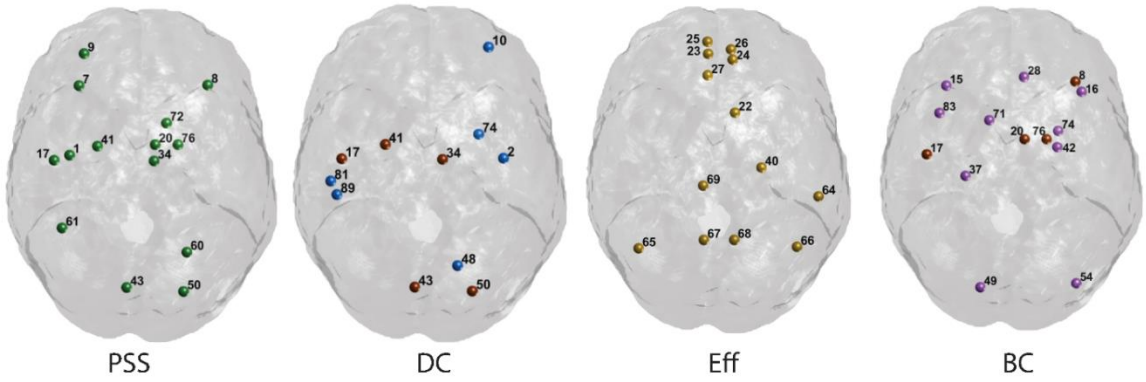


Figure 2.5. Graphical Display of the Highest-Ranking Nodes. *Functional hubs identified on the* PSS *measure and three standard topological centrality metrics (*BC, DC, Eff*). Hubs on each measure are defined as having a value >1 S.D. of the mean of their respective distribution. Nodes overlapping with the* PSS *hubs are shown in brown. The corresponding AAL labels for each numerical index are included in Supplementary Table 1.*

2.4 Discussion

Persistent homology provides a window into the global organization of the edges' weight fabric of a graph. The present results indicate that persistence homological scaffolds may be useful mathematical objects to consider in functional neuroimaging research. The persistence scaffold notably circumvents the need for *ad hoc* thresholding of the functional connectivity matrix and is constructed using the data of all the edges present in the original network. Moreover, the concept of *simplicial complexes* upon which the persistence scaffold is built allows one to describe relations between distributed sub-populations of network elements consistent with the brain's encoding of information in distributed networks, and is not restricted to dyadic associations between region pairs. Importantly, the results suggest that the unique mathematical attributes of the persistence homological scaffold may be useful for identifying nodes supporting the global integration of information processing in the human brain.

In order to study the relationship between standard network metrics and the persistence homological scaffold, I calculated the strength of each node in the persistence scaffold and termed this novel measure the persistence scaffold strength (*PSS*). I then examined how *PSS* relates to some of the local binarized and weighted graph theoretical metrics typically employed in neuroimaging studies. Of the binary graph metrics under study, *PSS* showed the strongest positive correlation with the betweenness-centrality metric (*BC*) across the entire threshold range. Even when controlling for the node degree by means of a partial correlation analysis, the positive association between *PSS* and *BC* remained

highly significant. This suggested that high *PSS* nodes are likely to contribute to the binding of information across different sources in the brain by creating shortest paths between node pairs. Conversely, a strong negative correlation was observed between *PSS* and local efficiency (*Eff*), and indicates that nodes with a high *PSS* are unlikely to participate in strongly integrated local networks. To further explore the association between the *PSS* measure and functional integration, I conducted a modularity analysis and computed the participation coefficient (*PC*) of network nodes. A strong positive correlation between *PC* and *PSS* was found in the network under study. Nodes with a high participation coefficient preferentially make connections to network communities other than their own, consistent with network roles in global integration.

Taken together, these observations lead to an understanding of the meaning of this new centrality measure and on the interpretation of persistent homological scaffold. The tendency of high *PSS* nodes to bind topologically remote modules in the brain whilst simultaneously avoiding clustered neighbourhood reflects the significance of persistent homology in resting-state fMRI data. *PSS* therefore captures different aspects of global network organization in a natural index that does not rely on any weighted average of classic graph metrics, and that extracts this information directly from the data. When bypassing the thresholding step and instead comparing the *PSS* to the *weighted* counterparts of the standard graph measures computed on the fully connected network, the results for *strength* and *wt-BC* were broadly consistent with those of the binarized networks. As in the binary network analysis, the *strength* vs *PSS* correlation was positive and significant, but weaker than the *wt-BC* vs *PSS* correlation. Moreover, the nodal *PSS* does not merely recapitulate the betweenness-centrality metric. Although the correlation between *PSS* and *BC* measures was significant at all thresholds under study in the binary networks analyses, only 4 of the 14 highest ranking *PSS* nodes overlap with the hubs identified on the *BC* metric (Figure 2.5). This may be explained by the fact that some nodes ranking highly on the betweenness-centrality metric concurrently participate in strongly connected neighborhood clusters; their respective edges would thus form clique complexes at an early stage in the filtration, leading to low *PSS* value. Moreover, the value of the correlation between *PSS* and *BC* was around $R = 0.4$ in both the binarized and weighted network analyses, which further suggests that the *PSS* and *BC* do not reflect identical network attributes.

The highest-ranking regions on the *PSS* measure were distributed across the brain (Figure 2.5), consistent with potential roles in the global integration of local networks. There

was nevertheless a tendency for the *PSS* hubs to belong to frontal cortical areas (middle & superior frontal gyri, precentral gyrus, rolandic operculum, cingulate), and subcortical structures (amygdala, globus pallidum, caudate nucleus). In the posterior brain, *PSS*-hubs within the parietal lobe included the inferior and superior divisions of the parietal gyrus but did not include midline parietal structures. Interestingly, no subdivision of the temporal cortices were included amongst *PSS*-hubs, despite several of these regions ranking highly on the *DC* measure. I also paid attention to the special case of high-ranking *PSS* nodes which did *not* qualify as "hubs" on any of the three standard topological centrality measures (*DC*, *Eff*, *BC*). This subset of nodes was anatomically restricted to the lateral frontal and parietal cortices. They included the middle and superior frontal gyri, as well as inferior and superior sections of parietal gyri. These findings would suggest that, relative to standard topological centrality metrics, the *PSS* may be particularly sensitive to the network activity of frontal and parietal association areas located on the lateral surface of the brain. This would be consistent with the established role of these regions towards supporting high-level cognitive and behavioral functions requiring the large-scale coordination of network elements.

It has now become well recognized that the brain performs local computations in segregated modules that become seamlessly integrated over space and time to support high-level functions necessary for survival. Some brain regions are likely to play a more critical role than others towards enabling the global integration of information. The exact identities of these regions and the optimal experimental approaches for identifying them remain unclear. Previous research has employed diffusion tensor imaging (DTI) and graph theoretical analysis to identify a subset of hubs which forms a central core or "rich-club" that has been suggested to be important for global brain integration by linking together spatially remote network communities (Van Den Heuvel and Sporns 2011). Yet, the mapping of a structural network architecture that can plausibly support segregation and integration does not describe the causal mechanisms and/or activity dynamics that actually underlie functional segregation and integration of information (Sporns 2013, Deco, Tononi et al. 2015). The identification of integrator hubs directly from *functional* neuroimaging data using the persistence homological scaffold may be particularly valuable in this regard.

The application of computational topology analysis to functional neuroimaging data is a novel avenue of research, and the physiological significance of homological scaffolds and measures derived from them remains unclear. Given that high *PSS* nodes participate in a large proportion of cycles along the filtration, such nodes may be well positioned to

contribute to a specific type of integration where, for example, a given neural pathway diverges than re-converges. Examples of such pathways include the dorsal/ventral visual streams and the well-defined cortico-basal loops between the basal ganglia and motor cortex. Further studies will be needed to test these hypotheses with specificity, but the identification of both visual areas as well as basal ganglia and cortical motor areas amongst the *PSS* hubs in the present analysis nevertheless supports this idea. Whilst the present results suggest that high-ranking *PSS* nodes could be well positioned to support the integration of information across segregated brain modules, further studies will be needed to confirm this observation. A possibility would be to investigate changes in *PSS* hubs assignment and distributions in clinical syndromes characterized by disordered functional integration at the whole-brain scale, such as schizophrenia (Alexander-Bloch, Gogtay et al. 2010, Lynall, Bassett et al. 2010). This could help determine to what extent *PSS*-hubs support the integration of network elements, and potentially provide useful insights into the neurobiological attributes of topologically central brain regions in the homological scaffold.

A methodological limitation of this study is the choice of the representative cycles for homology classes, which could result in selecting edges that do not belong to the shortest cycle around a certain hole. During the filtration process, a cycle will shrink due to the addition of an edge. Although the shrinking has no topological meaning for the hole itself as it remains the same, its representation changes, i.e. the specific edges forming its boundary change (see Supplementary Figure 1). The question "what is the best representative of a cycle" is an open problem and the definition of *best* likely depends on the problem at hand. One could consider employing computationally cumbersome techniques to track the shortest path across the filtration and then update the scaffold accordingly (Dey, Hirani et al. 2011). Further work is needed to establish which protocol would be most suited to the specific case of fMRI networks. Our results on network communities nevertheless suggest that the cycle choice issues might not be so critical in this study and potentially lead to a stronger *PSS* interpretation. Indeed network communities, being densely connected internally and strong information integrators, likely constitute the network regions where connected triangle components reside and thus the regions where different representative cycle choices are possible. Moreover, scaffold hubs already tend to have large participation coefficients suggesting that they behave as information brokers between these communities and are therefore, although imperfectly, capturing the large-scale homological structure.

2.5 Chapter Summary

In summary, the present Chapter has explored the relationship between standard network metrics in a functional brain network and the persistence homological scaffold derived from the same fMRI dataset. The computation of a novel local centrality measure on the persistence homological scaffolds termed "persistence scaffold strength" differs from standard applications of graph theory to functional neuroimaging data as the scaffolds are not derived from dyadic interactions between network elements, and also consider information from all edges in the network. The results suggest that topologically central nodes in the persistence scaffold may play important roles towards supporting the functional integration of information across brain modules. This demonstrates that the study of functional connectivity networks from a non-dyadic perspective based on the homology of the data can provide useful insights into the brain's functional architecture.

Chapter 3: Global Brain Dynamics in Altered States of Consciousness

3.1 Introduction

In the previous Chapter, a novel application of algebraic topology was used to analyze time-averaged (i.e. "static") functional connectivity data from healthy subjects with the aim of identifying brain areas well-positioned to promote cross-modular integration in the human brain. The present Chapter marks the beginning of our investigation of the dynamical integration/segregation balance in altered states of consciousness.

Toward this aim I have analyzed two separate fMRI datasets. The first dataset consists of a cohort of healthy adults scanned during wakeful rest and then deep sleep (NREM stage III) throughout the same scanning session. As described earlier, NREM stage III (N3) is one of two stages of slow-wave-sleep ("deep-sleep") (see Introduction 1.4.1). As such, the behavioral output (or lack thereof) of a person in N3 sleep is drastically different from wakeful rest, and associated changes in the brain's functional organization occur (see Introduction 1.4.2). The second dataset was the first ever acquired neuroimaging dataset of healthy individuals administered with a psychedelic compound (Carhart-Harris, Erritzoe et al. 2012). In this fMRI experiment, healthy volunteers underwent a resting-state fMRI scan at baseline and intravenously infused with either psilocybin or a saline placebo halfway through the session, immediately after which a second resting-state scan of the same duration was acquired. Psilocybin is a serotonergic psychedelic compound, and the active ingredient in "magic mushrooms" (see Introduction 1.3.1). The limited number of functional connectivity investigations of psilocybin's effects in humans suggest that the compound may enhance cross-modular integration (see Introduction 1.3.2).

Importantly, the analyses presented in this Chapter shift the focus away from regional contributions to the integration/segregation balance and instead consider changes in the global brain dynamics in the psychedelic state and deep sleep relative to wakeful rest. Moreover, rather than employing time-averaged approaches to functional network connectivity, the analyses presented here leverage on methods which enable us to characterize whole-brain dynamical functional connectivity on much shorter time intervals (i.e. individual TR's) by computing the instantaneous phase of the BOLD signal.

The parallel analysis of slow-wave sleep and psychedelics fMRI datasets provides the exciting opportunity to investigate global brain dynamical changes associated opposite changes in the consciousness level relative to wakeful rest in healthy volunteers using a data-driven approach. There is currently no gold-standard methodology for characterizing the neural correlates of the conscious experience. The available evidence however suggests that the level of neural signal diversity and/or synchrony over time, as well as changes in the brain's modular organization may be especially informative in terms of characterizing consciousness level and/or contents (see Introduction 1.3.2 & 1.4.2). The measures under study in this Chapter, described in detail in the Methods section below, were chosen because of their direct relevance towards investigating of the dynamical integration/segregation balance in the human brain. I first examine the mean amount of synchrony (order parameter) and variability between different metastable FC configurations in whole-brain networks constructed from fMRI data. I then investigate the extent to which synchronization and desynchronization coexist in the network at a mesoscopic level by analyzing the "chimeraness" of the dynamics, which quantifies the variance in the order parameter across distinct network communities at fixed time points.

3.2 Methods

3.2.1 Participants

3.2.1.1 Psilocybin study:

Functional MRI data from nine healthy subjects were included in this study. Study inclusion criteria were: at least 21 years of age, no personal or immediate family history of a major psychiatric disorder, substance dependence, cardiovascular disease, and no history of a significant adverse response to a hallucinogenic drug. All of the subjects had used psilocybin at least once before, but not within 6 weeks of the study.

3.2.1.2 Sleep study:

Neuroimaging data of sufficient quality were collected from 18 healthy participants (10 males, 8 females aged 23.1 ± 2.6 years). The experimental protocol was approved by the local ethics committee "Ethik-Kommission des Fachbereichs Medizin der Goethe-Universität Frankfurt am Main, Germany" with the ethics application title "Visualisierung von Gehirnzuständen in Schlaf und Wachheit zum Verständnis der Abnormitäten bei Epilepsie und Narkolepsie" and the assigned number: 305/07.

3.2.2 Experimental protocol

3.2.2.1 Psilocybin study:

All subjects underwent two 12 min eyes closed resting state fMRI scans over separate sessions, at least 7 days apart. In each session, subjects were injected intravenously with either psilocybin (2 mg dissolved in 10 ml saline, 60s intravenous injection) or a placebo (10 ml saline, 60s intravenous injection) in a counterbalanced design. Injections were given manually by a doctor within the scanning suite. The infusions began exactly 6 min after the start of the 12 min scans and lasted 60 seconds. The subjective effects of psilocybin were felt almost immediately after injection and sustained for the remainder of the scanning session.

3.2.2.2 Sleep study:

Participants entered the scanner in the evening and underwent a resting state fMRI session with simultaneous EEG acquisition and polysomnograpy lasting for 52 minutes. Participants were asked to relax, close their eyes and not to fight sleep. Lights were dimmed in the scanner room and subjects were shielded from scanner noise using earplugs. All participants reported a wake up time between 5:00 AM and 11:00 AM on the day of the scan, and a sleep onset time between 10:00 PM and 2:00 AM on the previous night. In the present study, I only considered data from wakefulness and deep sleep (N3). All of the 18 participants included in the present analysis reached N3 sleep during the fMRI scan. Sleep staging was determined via simultaneously acquired polysomnography data according to the standard guidelines of the American Academy of Sleep Medicine. The mean durations of contiguous sleep epochs were 12.4 ± 6.6 minutes for wakefulness, 8.5 ± 2.8 minutes for N1, 14.7 ± 5.7 minutes for N2 and 16.5 ± 8.4 minutes for N3 sleep.

3.2.3 Neuroimaging data acquisition & processing

3.2.3.1 Psilocybin imaging:

Neuroimaging data were acquired using a 3T GE HDx system. Anatomical scans were performed before each functional scan and thus prior to administering either the drug or placebo. Structural scans were collected using a 3D fast spoiled gradient echo scans in an axial orientation, with field of view = 256×256×192 and matrix = 256×256×192 to yield 1 mm isotropic voxel resolution (repetition time/echo time TR/TE = 7.9/3.0 ms; inversion time = 450 ms; flip angle = 20°). BOLD-weighted fMRI data were acquired using a gradient echo planar imaging sequence, 6 TR/TE 3000/35 ms, field-of-view = 192 mm, 64 × 64 acquisition

matrix, parallel acceleration factor = 2, 90° flip angle. Fifty-three oblique axial slices were acquired in an interleaved fashion, each 3 mm thick with zero slice gap (3 × 3 × 3 mm voxels).

Functional MRI were processed data using MELODIC (Multivariate Exploratory Linear Decomposition into Independent Components) (Beckmann and Smith 2004), part of FSL (FMRIB's Software Library, www.fmrib.ox.ac.uk/fsl). The default parameters of this imaging pre-processing pipeline were used on all participants: motion correction using MCFLIRT (Jenkinson, Bannister et al. 2002), non-brain removal using BET (Smith 2002), spatial smoothing using a Gaussian kernel of FWHM 5mm; grand-mean intensity normalization of the entire 4D dataset by a single multiplicative factor and linear de-trending over 50 second intervals. Tools from FSL were then used to extract and average the time courses from all voxels within each cluster in the AAL-90 atlas (Tzourio-Mazoyer, Landeau et al. 2002).

3.2.3.2 Sleep imaging:

T2*-weighted echo planar images were acquired on a 3T Siemens Trio system with TR/TE = 2080 ms/30 ms, matrix 64 × 64, distance factor 50% and field of view of 192 mm^2 to yield a voxel size of 3 × 2 × 2 mm^3. A total of 1505 volumes were collected. fMRI processing: Using Statistical Parametric Mapping (SPM8,www.fil.ion.ucl.ac.uk/spm) Echo Planar Imaging (EPI) data were realigned, normalized (MNI space) and spatially smoothed (Gaussian kernel, 8 mm3 full width at half maximum). Data was re-sampled to 4 x 4 x 4 mm resolution to facilitate removal of noise and motion regressors. BOLD signals are finally averaged over cortical and sub-cortical regions of interest to construct functional networks. Cardiac, respiratory (both estimated using the RETROICOR method (Glover, Li et al. 2000) and motion-induced noise were regressed out. Data was band-pass filtered in the range 0.01-0.1 Hz using a sixth order Butterworth filter. BOLD timeseries were extracted into AAL-space as outlined above for the psilocybin fMRI data.

An optimised polysomnographic setting for EEG was employed (chin and tibial EMG, ECG, EOG recorded bipolarly) with 30 EEG channels recorded with FCz as the reference (sampling rate 5 kHz, low pass filter 250 Hz). Pulse oxymetry and respiration were recorded via sensors from the MR scanner compatible devices (BrainAmp MR+, BrainAmpExG; Brain Products, Gilching, Germany) to facilitate sleep scoring during fMRI acquisition.

3.2.3.3 DTI acquisition and processing:

Because DTI data were not collected in the aforementioned sleep and psilocybin studies, I used DTI data collected in 16 healthy right-handed participants from a separate study conducted at Aarhus University, Denmark (11 men and 5 women, mean age: 24.8 ± 2.5). The imaging data were recorded in a single session on a 3 T Siemens Skyra scanner at CFIN, Aarhus University, Denmark. The following parameters were used for the structural MRI T1 scan: voxel size of 1 mm^3; reconstructed matrix size 256 × 256; echo time (TE) of 3.8 ms and repetition time (TR) of 2300 ms. DTI data were collected using TR = 9000 ms, TE = 84 ms, flip angle = 90°, reconstructed matrix size of 106 × 106, voxel size of 1.98 × 1.98 mm with slice thickness of 2 mm and a bandwidth of 1745 Hz/Px. Furthermore, the data were recorded with 62 optimal nonlinear diffusion gradient directions at b = 1500 s/mm^2. One of the DTI images was collected applying anterior to posterior phase encoding direction and the other acquired in the opposite direction. The automated anatomical labelling (AAL) template was used to parcellate the entire brain into 90 regions and generate the structural connectivity (SC) maps for each participant. The two recorded datasets were processed, each with different phase encoding to optimise signal in difficult regions. These structural connectivity maps were constructed using a three-step process. First, the regions of the whole-brain network with the AAL template as used in the functional MRI data were defined. Secondly, probabilistic tractography was used to estimate the connections between nodes in the whole-brain structural network. The individual SC matrices were averaged across participants to yield a group-level SC matrix. A community detection algorithm based on modularity (Louvain method with finetuning (Blondel, Guillaume et al. 2008)) was applied to the group-averaged SC, and identified 10 communities for the partition optimizing the modularity function. These network modules were used for the chimeraness index analysis described further below.

3.2.4 Computation of dynamical functional connectivity (dFC)

For each subject and in each dataset/experimental condition, I computed a phase coherence matrix (90 x 90) to capture the amount of interregional BOLD signal synchrony at each time point (TR). To compute the phase coherence between each pair of AAL regions, first the BOLD phases, $\theta(n,t)$, were estimated using the Hilbert transform for each BOLD regional timecourse. The Hilbert transform expresses a given signal x in polar coordinates as: $x(t) = A(t) * \cos(\theta(t))$. Upon calculating the phases (angles) of the BOLD signals over time, the phase coherence $\mathrm{dFC}(n,p,t)$ between brain areas n and p at time t is estimated:

$$\mathrm{dFC}(n,p,t) = \cos(\theta(n,t) - \theta(p,t))$$

Using the cosine function, two areas n and p with temporarily aligned BOLD signals (i.e. with similar angles) at a given TR will have a phase coherence value $\mathrm{dFC}(n,p,t)$ close to 1 (since cos(0°)=1). On the other hand, time points where the BOLD signals are orthogonal (for instance, one increasing at 45° and the other decreasing at 45°) will have $\mathrm{dFC}(n,p,t)$ close to 0 (since cos(90°) = 0). The resulting dFC for each subject in each condition is a thus three-dimensional tensor with size NxNxT, where N=90 is the number of brain areas and T=100 is the total number of time points. Note that the phase coherence matrix is undirected and, as such, for each time *t*, the NxN $\mathrm{dFC}(t)$ matrix is symmetric across the diagonal (See Figure 3.1).

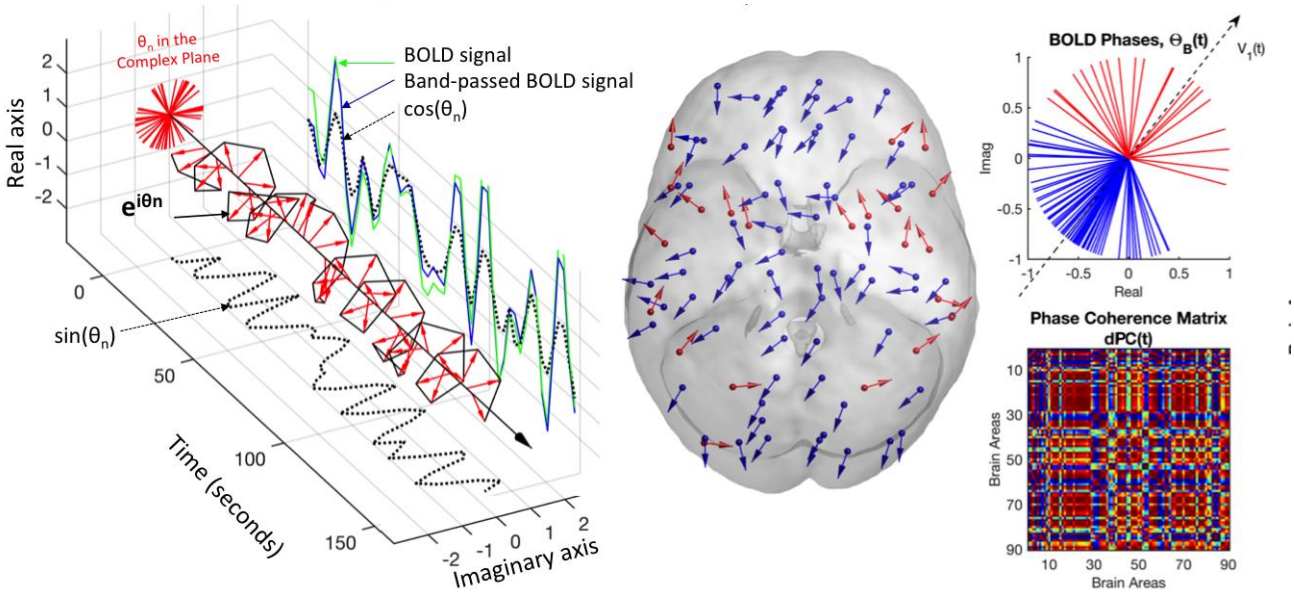


Figure 3.1. Summary of method for computing dynamical functional connectivity (dFC) matrix from fMRI data. Left: *BOLD timeseries for each AAL region first undergo a Hilbert transform, converting the signal amplitude into a phase value at each TR.* Right: *The alignment between phases is then calculated for each pair permutation of nodes in the network. The resulting dFC matrix (sometimes called Phase Coherence matrix) provides an estimate of the extent to which phase angles are coherent (or not) between region pairs across the whole network at a specific time point (adapted from Cabral, Vidaurre et al. 2017).*

3.2.5 Order Parameter, Synchrony and Metastability

I investigated how the psilocybin injection and N3 sleep respectively altered the order and stability of BOLD signals over time. At each instant of time, the degree of order between BOLD phases $\theta(n,t)$, n=1,..,90, can be quantified using the Kuramoto Order Parameter, $OP(t)$, which can range between 0 (when all BOLD signals are out of phase) and 1 (when all BOLD signals are in phase):

$$OP(t) = \frac{1}{N}\left|\sum_{n=1}^{N} e^{i\theta(n,t)}\right|$$

The variability of the Order Parameter over time (standard deviation) is typically used to infer the degree of meta-stability in a system, whereas its mean informs whether the system is incoherent, partially synchronized or fully synchronized, on average (Cabral, Hugues et al. 2011, Deco and Kringelbach 2016). In other words, if the order parameter is constant over time, it means that the system is in a stable equilibrium, be it synchronized or not. When several attractors exist, and the system switches from one to another, then the variance of the order parameter will grow with the metastability of the dynamics. To investigate the effects of psilocybin and N3 sleep on the order and stability of BOLD activity, I therefore calculated the mean and the standard deviation of the order parameter over time, in each subject and experimental condition. Between-condition differences on these measures were assessed using a paired, two-sided t-test ($\alpha = 0.05$).

3.2.6 Chimeraness Index

The chimeraness index (χ) provides an estimate of the extent to which the internal synchrony of individual communities varies across the entire network (Shanahan 2010). This measure was originally developed to study synchronization behavior in community-structured oscillator networks *in silico* and, to our knowledge, has yet to be applied to empirical neuroimaging data. The level of internal synchrony between the instantaneous BOLD phases in a specific community can be expressed as:

$$\phi_c(t) = |\langle e^{i\theta_r(t)}\rangle|_{r\in_c}$$

where $\theta_r(t)$ is the phase of the BOLD signal in a brain region r at time t. Note this is equivalent to taking the mean of the instantaneous dFC matrix constructed for this particular community. In this case the community structure was derived from the anatomical connectome of a separate cohort of healthy subjects because DTI data were not collected as part of neither the psilocybin or sleep study. By sampling $\phi_c(t)$ at each time point (i.e. TR) in the recording interval, the prevalence of chimera-like states in the system can be quantified. To do so, we fix the time t and compute the variance $\sigma_{chi}(t)$ of $\phi_c(t)$ over all the communities in the network, which gives an indication of how chimera-like the system is at a specific time point. The average of this variance across the entire recording interval (T) yields the chimera index (χ), which provides an estimate of how chimera-like a typical state of the system is:

$$\chi = \langle \sigma_{chi} \rangle_T$$

The chimeraness index was computed for each study participant and experimental condition, and between-condition differences was assessed using a paired t-test.

3.3 Results

3.3.1 Whole-Brain Synchrony and Metastability

A significant reduction (-16.5%) in the global synchrony (mean of the order parameter over time) was observed in the N3 sleep condition relative to wakeful rest; $t(16) = 2.79$; $p = 0.013$. In the psilocybin study, a higher global synchrony value was observed following the psilocybin infusion relative to baseline (+8.1%). Although not meeting the significance threshold ($\alpha = 0.05$), statistical testing reflected a notable trend for this measure; $t(8) = 1.79$; $p = 0.11$. In the psilocybin experiment, I found a significant *increase* (+11.1%) in the temporal variability of the order parameter (metastability) at the whole-brain scale following the psilocybin injection relative to the pre-injection state; $t(8) = 2.41$, $p = 0.028$. In contrast the metastability measure was significantly decreased (-11.7%) in N3 sleep compared to wakeful rest $t(16) = 3.49$, $p = 0.003$ (Figure 3.2).

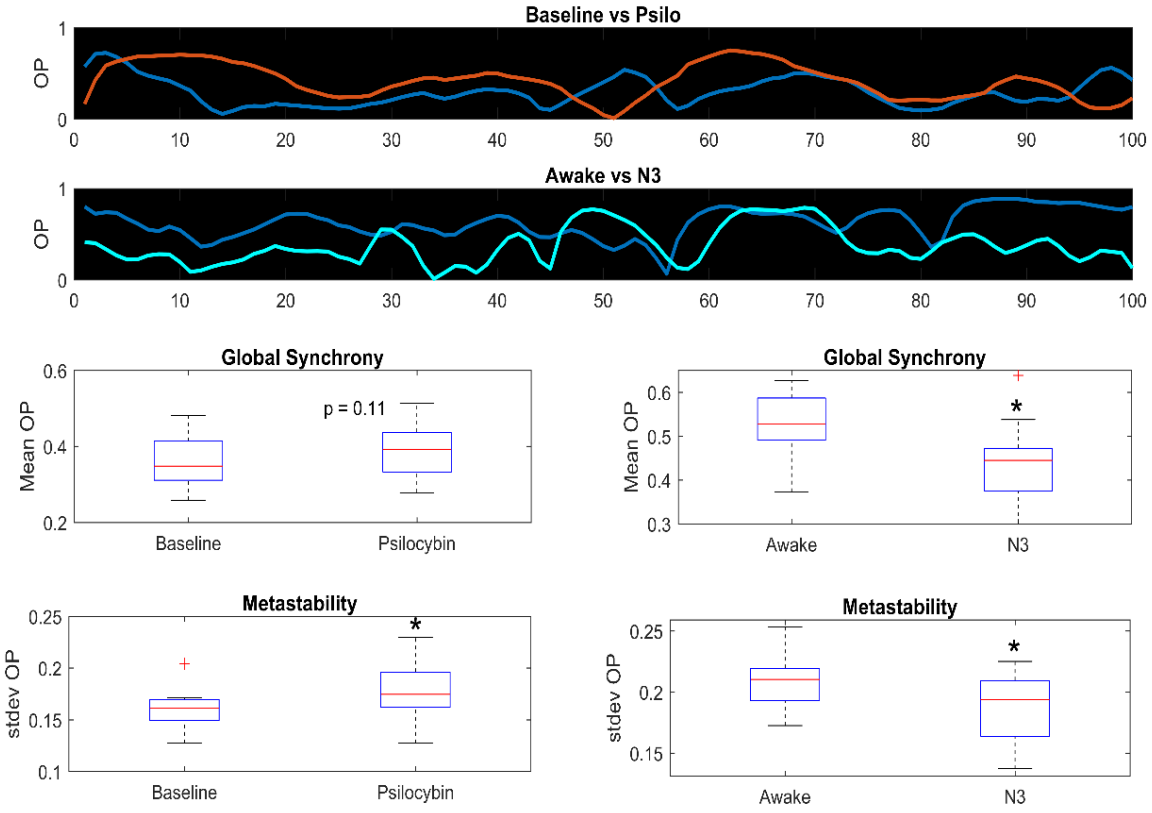


Figure 3.2. Whole-Brain measures of BOLD synchrony and metastability in altered states of consciousness. Top (i): *Example of the fluctuations of the order parameter (OP) of the system over time at baseline (blue) and post-psilocybin injection (red) for a study participant.* Top (ii): *OP during wakeful rest (blue) and N3 sleep (teal) for a single subject.* Middle: *Comparison of global synchrony measure pre vs post psilocybin infusion (left), and during wakeful rest vs N3 sleep (right).* Bottom: *Comparison of global metastability measure pre vs post psilocybin (left) and during wakeful rest vs N3 sleep (right). Asterisks denote statistically significant differences between conditions (α = 0.05).*

3.3.2 Chimeraness Index

The chimeraness index (χ) was significantly decreased (-3.7%) following the psilocybin infusion relative to baseline; t(8) = 2.47 p = 0.039, reflecting a reduced tendency for synchronization and desynchronization to co-occur across network communities at any given time. Conversely, an increase in χ was observed in N3 sleep relative to wakeful rest (+8.1%) reflecting an increase in the presence of chimera-like states in the system; t(17) = 3.65, p = 0.002 (Figure 3.3).

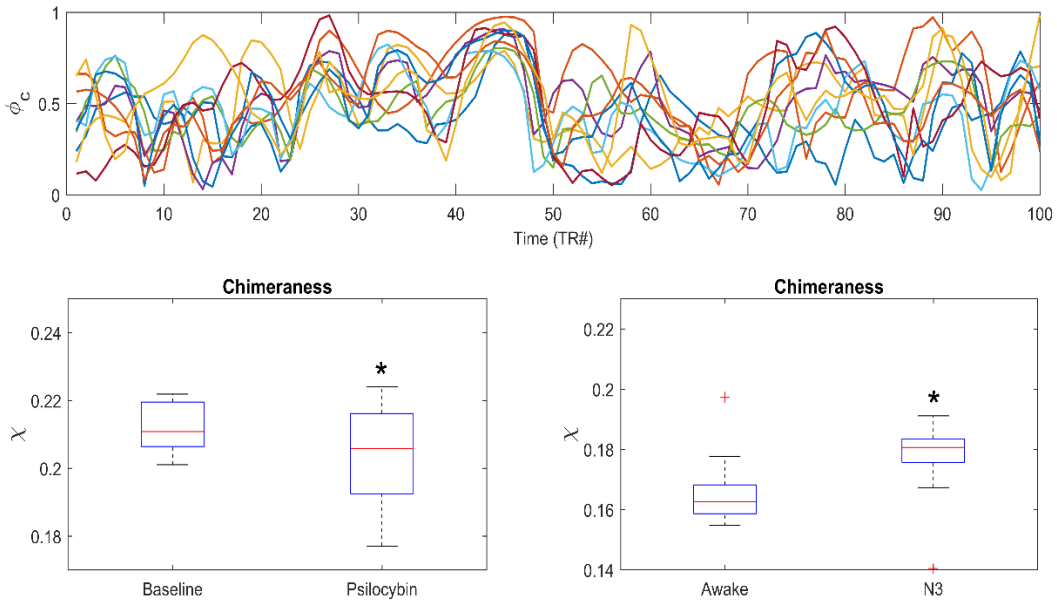


Figure 3.3. Chimeraness index estimated from fMRI data in altered states of consciousness. Top: *Plot of the internal synchrony over time for each of 10 network communities for a single study participant at baseline (resting-state fMRI). The time window between TR's #40-50 is characterized by a low degree of variability of internal synchrony across the network communities, and thus low chimeraness index value. On the other hand, the time window between TR's #75-85 is characterized by high variance in the internal synchrony across communities, which means that synchronization and de-synchronization co-exist, and chimeraness index (χ) is high.* Bottom: *Comparison of χ pre vs post psilocybin (left) and during wakeful rest vs N3 sleep (right). Asterisks denote statistically significant differences between conditions (α = 0.05).*

3.4 Discussion

In this Chapter, I have analyzed global brain dynamics in altered states of consciousness using measures of synchrony, metastability and chimeraness. The results show that global brain synchrony, assessed with the mean of the order parameter (OP) over time is significantly decreased in N3 sleep compared to wakeful rest in the sleep fMRI dataset. On the other hand, global synchrony was increased following the psilocybin infusion relative to the pre-injection baseline the psilocybin study; this increase did not quite meet our statistical significance threshold but indicated a strong trend given the small sample size ($p = 0.11$). Metastability at the whole-brain level, estimated as the standard deviation of OP over time, was significantly increased in following the psilocybin infusion; whereas it was significantly decreased during N3 sleep. Furthermore, the chimeraness index (χ), which reflects the tendency for synchronization and desynchronization to co-occur across network communities at any given time (i.e. prevalence of chimera-states in the system) was significantly decreased in participants under the influence of psilocybin, and significantly increased during N3 sleep.

The increased global metastability following the psilocybin infusion compared to the pre-injection baseline is consistent with a prior fMRI investigation of the same dataset in which a greater diversity of functional connectivity motifs was observed after the psilocybin infusion within a small network consisting of the bilateral hippocampal and ACC regions, thus reflecting increased variability in the collective repertoire of metastable states (Tagliazucchi, Carhart-Harris et al. 2014). This prior analysis had purposely limited the number of regions included in the analysis in order to perform an exhaustive counting of all possible FC states. Here I used a complementary analytical approach to demonstrate that increased metastability of dynamic FC under psilocybin is generalizable to the whole-brain scale. Our findings are also consistent with a recent MEG study of psilocybin in which increased neural signal diversity was observed relative to placebo. Signal diversity was computed by using the Lempel-Ziv complexity of single MEG channels (LZ_S), which quantifies the number of distinct patterns present in the data (i.e. compressibility of a signal) (Schartner, Carhart-Harris et al. 2017). The increased metastability of FC dynamics under psilocybin may be interpreted in the context of the "entropic brain" theory of conscious states according to which more variable brain activity and dynamics reflect more a variable and dynamic conscious experience (Carhart-Harris 2018). The trend towards increased global synchrony under psilocybin is consistent with the results from previous time-averaged functional connectivity analyses of the same dataset showing stronger correlations between resting-state networks following the psilocybin injection, as well as increased cross-modular integration (Petri, Expert et al. 2014, Roseman, Leech et al. 2014). This result is also in agreement with the finding that LSD, a synthetic psychedelic compound pharmacologically similar to psilocybin (i.e. LSD is also a 5-HT_{2A} receptor agonist), expands global connectivity in the brain as measured with resting-state fMRI (Tagliazucchi, Roseman et al. 2016) (see Introduction 1.3.2).

Our analysis of the slow-wave-sleep (N3) fMRI data on the other hand revealed that the brain dynamics become significantly less metastable during N3 than during wakeful rest. This is in agreement with prior analyses of EEG recordings that showed decreased LZ_S during slow-wave-sleep, indicating that loss of consciousness during sleep is associated with a lowering of the brain's dynamical complexity (Andrillon, Poulsen et al. 2016, Schartner, Pigorini et al. 2017). A recent whole-brain computational modelling study also revealed that the brain's global dynamical working point transitions from the edge of a bifurcation between noisy and sustained oscillatory behavior during wakefulness to a noisy regime

characterized by increased dynamical stability during N3 sleep (Jobst, Hindriks et al. 2017). Furthermore**,** the finding of a reduction in global brain synchrony during N3 sleep is in agreement with the reported breakdown of time-averaged FC in whole-brain networks during slow-wave sleep compared to wakeful rest (Spoormaker, Schröter et al. 2010) reflecting reduced activity correlations between spatially remote brain regions (see Introduction 1.4.2).

To our knowledge, the present analysis was the first application of the chimeraness index to empirical functional neuroimaging data. Earlier studies had applied this measure to characterize the simulated dynamics of community-structured oscillator network models (Shanahan 2010). Here I report a significant decrease in the chimeraness index following the psilocybin infusion relative to the pre-injection baseline. There are two theoretical scenarios in which the chimeraness can be *minimized* at any given time point: *i)* the internal synchrony of all communities is nearly equal (i.e. the communities are highly synchronized with each other) in which case the variance $\sigma_{chi}(t)$ of the internal synchronies will be near-zero; or *ii)* the internal synchrony of every community approaches zero and, as such, the communities are fully desynchronized with one another at a given time. The latter scenario is not plausible here since, as reported above, an *increase* in the global synchrony under the influence of the drug in fact occurs, rather than global de-synchronization. I therefore attribute the decrease in the chimeraness index following the psilocybin infusion to a higher level of synchrony across the network communities induced by the drug, which effectively diminishes the prevalence of chimera-like states over time. Conversely, I reported an increase in the chimeraness index for the N3 sleep condition relative to wakeful rest. I attribute this finding to to a lower level of synchrony across the communities which maximizes $\sigma_{chi}(t)$ and promotes the emergence of chimera states at any given time. In other words, during slow-wave sleep it becomes "harder" for different communities to align their internal frequencies, yet a reasonable degree of within-module synchrony is, on average, maintained throughout the recording interval ($\varphi_c(t) > 0$). This is broadly consistent with earlier results demonstrating that the modularity of functional brain networks increases during NREM sleep relative to wakeful rest, which signals a breakdown of integration between functional modules (see Introduction 1.4.2).

A limitation of the present analyses is inherent to the use of fMRI to study brain dynamics. It is important to bear in mind that the BOLD signal is an indirect measure of neural activity (as described in Introduction 1.1.1), which can complicate functional

interpretations. Since the BOLD response depends upon neurovascular coupling, it is important to account for potential effects of psilocybin on the vascular system. This is especially critical in light of psilocybin's documented tendency to cause headache, the severity of which is dose-dependent (Johnson, Sewell et al. 2012), as well as the fact that psilocybin may enhance nitric oxide release *in vitro* (a potent vasodilator) through via gene regulatory mechanisms (Reuter, Chiarugi et al. 2003, Johnson, Sewell et al. 2012). Carhart-Harris and colleagues addressed this potential confound by including a breath-hold paradigm at the end of each BOLD scan (Carhart-Harris, Erritzoe et al. 2012). The accumulation of CO_2 in the bloodstream (hypercapnia) is known to significantly increase the BOLD signal via CO_2 mediated vasodilation (Murphy, Harris et al. 2011), and therefore a direct effect of psilocybin on the neurovasculature would cause an enhanced BOLD response to breath hold. However, no difference was found between psilocybin and placebo during the breath-hold part the scan. Whilst the results from this control experiments were reassuring, the potential confounding neurovascular effects of psilocybin on the BOLD signal cannot be completely eliminated.

Another limitation is the relatively small number of subjects included in the psilocybin study (n = 9). The small sample size, combined with the fact that relatively short fMRI timeseries (100 TR's) were collected in each experimental condition, limits the sensitivity of between-condition comparisons. Statistically significant effects were nevertheless detected for the chimeraness and metastability measures. Also note that significant correlations were not found between the global brain activity measures of interest in this Chapter, and subjective reports of psilocybin effects. This may be due to the small sample size, and/or the fact that the subjective reports of the psychedelic experience were not assessed using a structured psychological instrument at the time of scanning. As stated above, DTI data were not collected as part of neither the psilocybin or sleep study. I therefore used the group-averaged anatomical connectome from a different cohort of healthy subjects to define the network communities used in the chimeraness index analysis. While deriving the structural connectome from the same group of study participants would have been ideal, it is common practice to recourse to structural data from a different cohort when necessary; at least when studying aged-matched, normal populations. Finally, the analyses conducted here were, by design, used to investigate strictly global changes in brain dynamics in altered states of consciousness, rather than functional changes in specific regions and/or networks. These equally important investigations will instead be covered in the next Chapters.

To our knowledge, this is the first study investigating brain dynamical changes in consciousness level in "opposite directions" relative to wakeful rest by employing the same neuroimaging modality and analysis methods. The results suggest that the brain dynamical regime induced by a psilocybin infusion is characterized by an increase in global synchrony, enhanced metastability and a higher probability for spatially remote brain modules to synchronize over time. Such a dynamical regime would therefore promote integration at the expense of segregation in the psychedelic state; a finding consistent not only with prior neuroimaging studies of the psychedelic state, as discussed above, but also with subjective reports of hyper-associative cognition and synesthesia reported by several study participants injected with psilocybin (Carhart-Harris, Erritzoe et al. 2012). Contrastingly, in deep (N3) sleep, metastability is overall reduced and the system's behavior is characterized by a tendency for both individual brain areas, as well as network communities, to become desynchronized over time. This would indeed bias the dynamical integration/segregation balance in favor of the segregation of information and contribute to the loss of consciousness and behavioral responsiveness experienced during slow-wave sleep, in agreement with the integrated information theory of consciousness and dynamic core theory (IIT) (see Introduction 1.2.1 & 1.2.2). The application of these same measures to relevant clinical datasets (i.e. coma, anesthesia) would represent an interesting next step experimentally, and could perhaps help contribute to patient monitoring in these areas (Owen, Coleman et al. 2006, Mhuircheartaigh, Warnaby et al. 2013).

3.5 Chapter Summary

In this Chapter, I have investigated global brain dynamical changes in altered states of consciousness with a focus on the segregation and integration balance in whole-brain networks. I computed measures of global synchrony, metastability and chimeraness based on the instantaneous phase coherence matrix and its order parameter. I emphasize the *dynamic* aspect of these analyses because the vast majority of network-based analyses of fMRI data in slow-wave sleep and psychedelics conducted to date have instead employed *time-averaged* functional connectivity measures. The results revealed, for the first time in a whole-brain network, that the psychedelic state induced by a psilocybin infusion enhanced global synchrony and metastability relative to baseline, whilst slow-wave sleep was characterized by significant reductions on these same measures compared to wakefulness. I also showed that the network communities' internal synchronies were on average more homogenous *in space* at any given time point in the psychedelic state compared to baseline,

and more variable during deep sleep. The brain dynamical changes reported here are therefore broadly consistent with those of increased modularity in slow-wave sleep and enhanced cross-modular integration under psychedelics from prior static functional connectivity analyses of these same datasets.

Chapter 4: Altered Trajectories in the Dynamical Repertoire of Functional Network States under Psilocybin

4.1 Introduction

In the previous Chapter, we began our exploration of the integration/segregation balance in altered states of consciousness by investigating global brain dynamics. Let us now turn our attention to the system-level and investigate the dynamical exploration of functional connectivity "states" over time. High-order mental processes involve the coordinated integration of information over spatially-distributed networks of specialized brain areas, and a robust repertoire of large-scale functional networks has been consistently detected across individuals and neuroimaging modalities. Accordingly, brain dynamics can be described in terms of spontaneous transitions within a repertoire of discrete metastable states of functional connectivity (FC), or "FC states", which underlie different mental processes (Tononi and Edelman 1998, Hansen, Battaglia et al. 2015, Cabral, Kringelbach et al. 2017, Cabral, Vidaurre et al. 2017, Cavanna, Vilas et al. 2017).

How changes in the brain's dynamical landscape relate to changes in behavior and cognition remains unclear, however. In the present Chapter, I investigated changes in the brain's dynamical repertoire in fMRI data from healthy participants intravenously injected with the psychedelic compound psilocybin (the same fMRI dataset analyzed in Chapter 3). The phenomenology of psilocybin includes a sense of 'unconstrained' consciousness characterized by hyper-association and profound alterations in the perception of time, space and selfhood (see Introduction 1.3.1).

In light of these subjective effects of psilocybin, one would expect the brain's dynamical landscape to become altered under the influence of the drug. This may be characterized by a combination of: 1) the emergence of atypical FC states, comparatively unexplored during normal wakefulness; 2) the suppression of common FC states that are normally highly visited at baseline; and 3) changes in the transition patterns between FC states. Preliminary support for these ideas first appeared in a fMRI study which found increased metastability in several canonical resting-state networks under psilocybin (Carhart-Harris, Leech et al. 2014). A dynamical FC analysis of this same fMRI data using windowed correlations revealed both a larger repertoire of FC motifs within a small subnetwork of four brain regions comprising the bilateral hippocampus and ACC under

psilocybin compared to placebo as well as greater entropy of the motif sequence (Tagliazucchi, Carhart-Harris et al. 2014). Furthermore, a recent fMRI study based on a graph signal analysis investigated the dynamical changes in brain states in healthy participants under the influence of the synthetic psychedelic LSD. It was found that the drug, which is pharmacodynamically similar to psilocybin, leads to an expansion of the repertoire of active brain states in healthy participants (Atasoy, Roseman et al. 2017).

These prior results call for a detailed investigation into the dynamics of anatomically specific functional networks in the psychedelic state. An improved understanding of the neural correlates underlying the experience of unconstrained cognition and enhanced mind-wandering reported by subjects under the influence of psilocybin may provide insights into the drug's action at the system level and perhaps inform on its demonstrated therapeutic potential for the treatment of neuropsychiatric disorders, such as depression (Carhart-Harris, Erritzoe et al. 2012, Carhart-Harris, Bolstridge et al. 2016). Toward this aim, the present study employed a novel data-driven approach to study brain dynamics in the psychedelic state, which focuses on the dominant FC pattern captured by the leading eigenvector of dynamic FC matrices, and enables the identification of recurrent FC patterns over time ("FC-states") (Cabral, Vidaurre et al. 2017). This approach enabled us to investigate the probability of occurrence of and transition profiles between FC-states extracted from fMRI data in healthy participants under the influence of psilocybin.

4.2 Methods

4.2.1 Participants, Experimental Protocol, Neuroimaging Data Acquisition & Processing

These subsections of Methods are as previously described in Sections 3.2.1, 3.2.2 and 3.2.3, respectively.

4.2.2 Dynamic Functional Connectivity Analysis & FC Leading Eigenvector

The dynamic functional connectivity analysis was carried out exactly as outlined previously in Section 3.2.4, yielding a phase coherence matrix $\mathrm{dFC}(n, p, t)$ between brain areas n and p at time t for each subject, and in each of the four experimental conditions mentioned above. Then, to characterize the evolution of the dFC matrix over time, I employed a method termed Leading Eigenvector Dynamics Analysis (LEiDA) focusing solely on the evolution of the dominant patterns of functional connectivity, which is the partition of the ROIs into two modules/communities and captures most of the coherence-based connectivity of the system (Cabral, Vidaurre et al. 2017). The leading eigenvector

$V_1(t)$, is a Nx1 vector that captures the dominant connectivity pattern of the $dFC(t)$ at each time t, given in matrix format by its outer product $V_1 \cdot V_1^T$. This approach substantially reduces the dimensionality of the data when compared to more traditional approaches considering all the values in the connectivity matrix (Hansen, Battaglia et al. 2015, Preti, Bolton et al. 2017).

To confirm the robustness of this approach, I examined the proportion of the phase coherence explained by the leading eigenvector for each $dFC(t)$. To do so, the coherence matrix B at time t is defined as:

$$B_{ij}(t) = \cos\left(\theta_i(t) - \theta_j(t)\right)$$

Note that $B(t)$ is equivalent to $dFC(t)$ expression used in the rest of the text, and simply used here to improve the readability of the equations. As $B_{ij}(t)$ it is a symmetric, real valued matrix, the spectral theorem applies and thus, for each time t, there exists an eigenbasis $\{v_i\}_{i=1}^N$, with associated eigenvalues $\{\lambda_i\}_{i=1}^N$:

$$B(t) = \sum_i \lambda_i v_i v_i' = \sum_i \lambda_i P_i = V \Lambda V'$$

where N is the number of ROIs ,the columns of V are the eigenvectors of B, Λ is the diagonal matrix of eigenvalues and P_i is the projector onto the subspace spanned by v_i. The eigenvalues are ordered in decreasing order : $\lambda_1 \geq \cdots \geq \lambda_N$. Then, using Principal Component Analysis (PCA), we can quantify the variance explained by each eigenspace of B, and thus the proportion of the signal explained by the leading eigenvector. The entries of the i^{th} column of B are the similarities between the phase of the region i and the others regions in the AAL parcellation. The phases of B are centered by removing the mean, and refer to quantities related to the centered similiarities with a subscript c :

$$B_c = B - \mathbf{1}B_{mc}'$$

where B_{mc} is the vector of the mean of the columns of B. Thus $B_c' B_c$ is the covariance matrix of the centered similarities between each pair of phases. Using standard PCA, we have :

$$B_c' B_c(i) = V_c \Lambda_c V_c' V_c \Lambda_c V_c' = V_c \Lambda_c^2 V_c' \Leftrightarrow V_c' B_c' B_c V_c = \Lambda_c^2$$

The ratio $\lambda_{c,i}^2 / \sum_j \lambda_{c,i}^2$ is then the proportion of the total variance in the similarities of the phases captured by the i^{th} eigenspace. As the eigenvalues are ordered in decreasing order,

the space associated with $\lambda_{c,1}$ will explain the most variance, and if $\lambda_{c,1}^2 > \sum_{i>1} \lambda_{c,i}^2$, it explains most of the variance in the similarities between phases.

Using this approach, I have found that $V_1(t)$ consistently explains > 0.5 of the variance in the similarities between phases at all time points in each experimental condition; with the distributions centering around 0.7 (Figure 4.1). The leading eigenvector therefore consistently explains most of the variance in the phase coherence matrix, and is thus representative of the dominant dynamical functional connectivity pattern at a given time point.

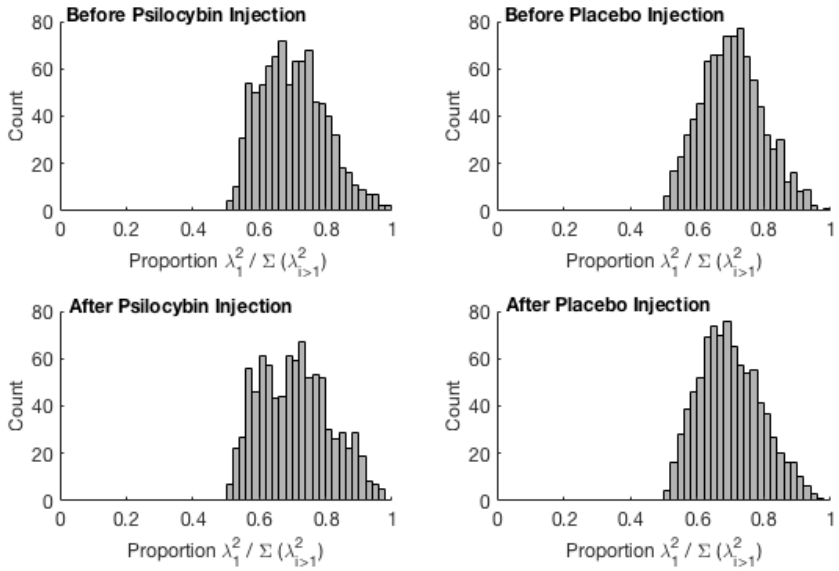


Figure 4.1. The leading eigenvector captures most of the variance in the similarities between phases at all time points. *Histograms of the ratio of the leading eigenvalue with respect to the sum of all eigenvalues at each time point, for all subjects in each of the 4 experimental conditions. The leading eigenvalue consistently represents more than 50% of all eigenvalues.*

4.2.3 Identification of FC states from the leading eigenvectors of phase coherence matrices

Upon computing the leading eigenvector $V_1(t)$ of the phase coherence matrix $dFC(t)$ for each TR, the next step in our analysis was to identify recurrent FC patterns in the data ("FC states"). A discrete number of FC patterns was detected by clustering the leading eigenvectors from the pooled pre/post psilocybin fMRI data (2 conditions) including all 100 TR's of all 9 subjects, which corresponded to a combined total of 1800 $V_1(t)$. The *k*-means clustering algorithm was run with *k* from 2 to 20. Clustering solutions output a *k* number of cluster centroids in the shape of Nx1 V_c vectors for each cluster *c*, which represent

averaged recurrent FC states. The outer product of each cluster centroid vector $V_c V_c^T$ is a NxN rank one matrix representing the dominant connectivity pattern, and the elements of V_c weigh the contribution of each brain area to the community structure established by the signs of the corresponding vector elements. To facilitate the neuroanatomical visualization and interpretation of FC-states, the cluster centroid vectors V_c were rendered onto a cortical surface using HCP Workbench. For the analysis of FC states in the placebo condition, I ran the *k*-means clustering using the same cluster centroids obtained from the pre- and post-psilocybin injection.

4.2.4 Probability of Occurrence and Switching Matrix of FC States

Upon identifying FC states, I computed the probability of occurrence of each FC state in each condition (i.e. pre/post psilocybin and pre/post placebo). The probability of occurrence (or fractional occupancy) is simply the ratio of the number of epochs assigned to a given cluster centroid V_c divided by the total number of epochs (TRs) in each experimental condition (which is the same in all four experimental conditions, i.e. 100 TRs). The probabilities were calculated for each subject, in each experimental condition and for the whole range of clustering solutions explored. In addition, I computed the switching matrix, which captures the trajectories of FC dynamics in a directional manner. It indicates the probability of, being in a given FC state, transitioning to any of the other FC states.

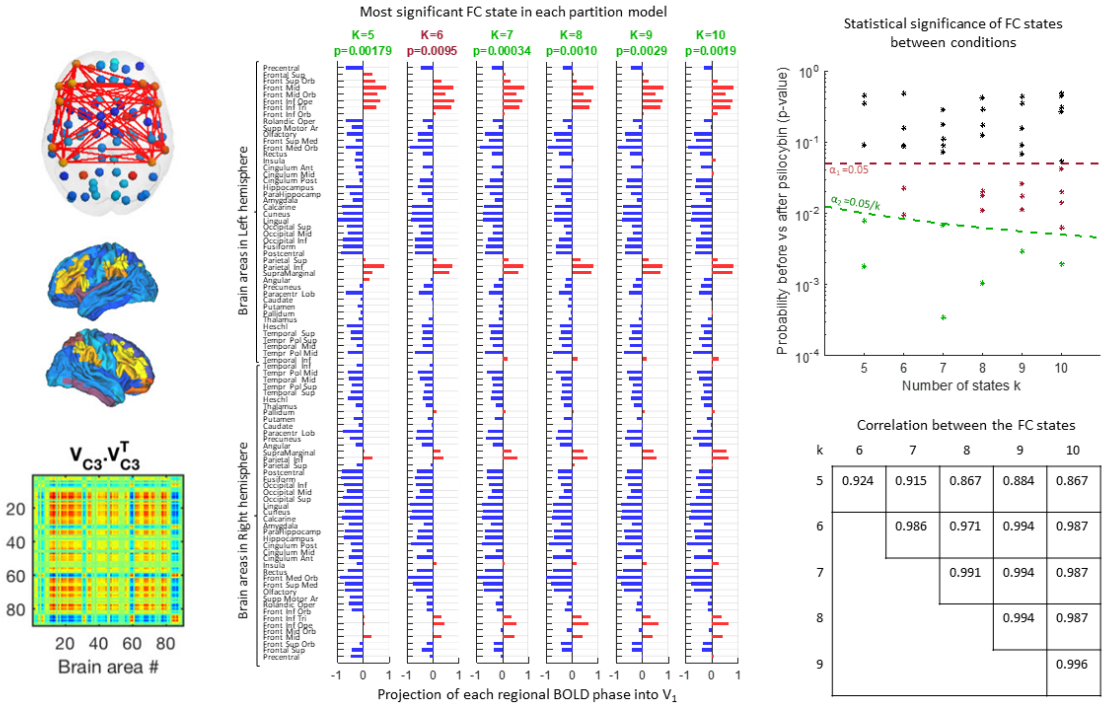
Differences in the probabilities of occurrence, and in the transition probabilities for the different states in the switching matrix were statistically assessed between each pair of experimental conditions using a permutation-based paired t-test. This non-parametric test uses permutations of group labels to estimate the null distribution. The null distribution is computed independently for each experimental condition. For each of 1000 permutations a t-test is applied to compare experimental conditions and the significance threshold of $\alpha = 0.05/k$ was used, in order to take into account the *k* number of states compared in each solution. In a follow-up analysis, I compared the number of occurrences of specific FC states at the subject level in the pre vs post-psilocybin injection conditions using a paired t-test.

4.3 Results

4.3.1 Dynamical repertoire of FC states is altered by psilocybin

A highly consistent FC pattern comprising bilateral frontal and parietal areas that had a significantly reduced probability of occurrence following the psilocybin injection was found, with $p<0.05/k$ for clustering solutions in the k = 5 to k = 10 range (Figure 4.2). Over

the aforementioned range of clustering solutions, this is the only FC state that reaches statistical significance at each *k*-value between conditions upon applying the Bonferroni correction for multiple comparisons. The strongest statistical effect was observed for $k = 7$. Also across $k = 5$ to $k = 10$ range of clustering solutions, the fractional occupancy of a globally coherent FC state was significantly higher post-psilocybin injection and survived the Bonferroni correction for multiple comparisons for $k = 5$, $k = 7$ and was borderline significant for $k = 10$ (Figure 4.2). In contrast, the probability of occurrence of all other FC states remained statistically similar before and after the psilocybin injection (all corrected p-values > 0.05).



k	6	7	8	9	10
5	0.924	0.915	0.867	0.884	0.867
6		0.986	0.971	0.994	0.987
7			0.991	0.994	0.987
8				0.994	0.987
9					0.996

Figure 4.2. Significant differences in FC state probability as a function of k. Left: *The most different FC state between groups for each partition model is a functional network consisting of lateral fronto-parietal areas.* Middle: *For all partition models, the probability of occurrence of FC states between conditions survived both the standard significance threshold of 0.05, fewer survived the more conservative significance threshold α_2 correcting by the number of states within each partition model.* Top right: *For each partition of the sample into k=5 to k=10 FC states, we plot the p-values associated to the comparison between FC state probability before and after psilocybin injection. We find that, although most FC states do not show significant differences between groups (black dots falling above the α_1=0.05 threshold), some FC states show significant differences in probability between groups, falling below (or very near for k=6) the corrected threshold by the number of clusters (α_2=0.05/k, green dashed line).* Bottom right: *The cluster centroid eigenvectors of the FC states representing the fronto-parietal network in different partition models are highly correlated with one another.*

In the partition with seven clusters, it can be seen that the fractional occupancy of the fronto-parietal state of interest significantly decreased from 14.3 ± 2.4% pre-injection (third most visited state) to 4.1 ± 1.2% following the psilocybin administration (p = 0.0003 uncorrected, p = 0.0021 after Bonferroni correction for the number of FC states compared)

(Figure 4.3). Conversely, a significant increase in the probability of occurrence of FC state I (dark blue) post-psilocybin injection was also observed with a fractional occupancy of 26.7 ± 4.5% pre-psilocybin injection and 37.2 ± 6.0% post-psilocybin injection (p = 0.0068 uncorrected, p = 0.047 after Bonferroni correction for multiple comparisons). This corresponds to a highly integrated FC state as it is the only state which does not present a natural bipartition. It is also the most prevalent state across all experimental conditions, in agreement with a prior study employing this same methodology on a different fMRI dataset (Cabral, Vidaurre et al. 2017) (Figure 4.3).

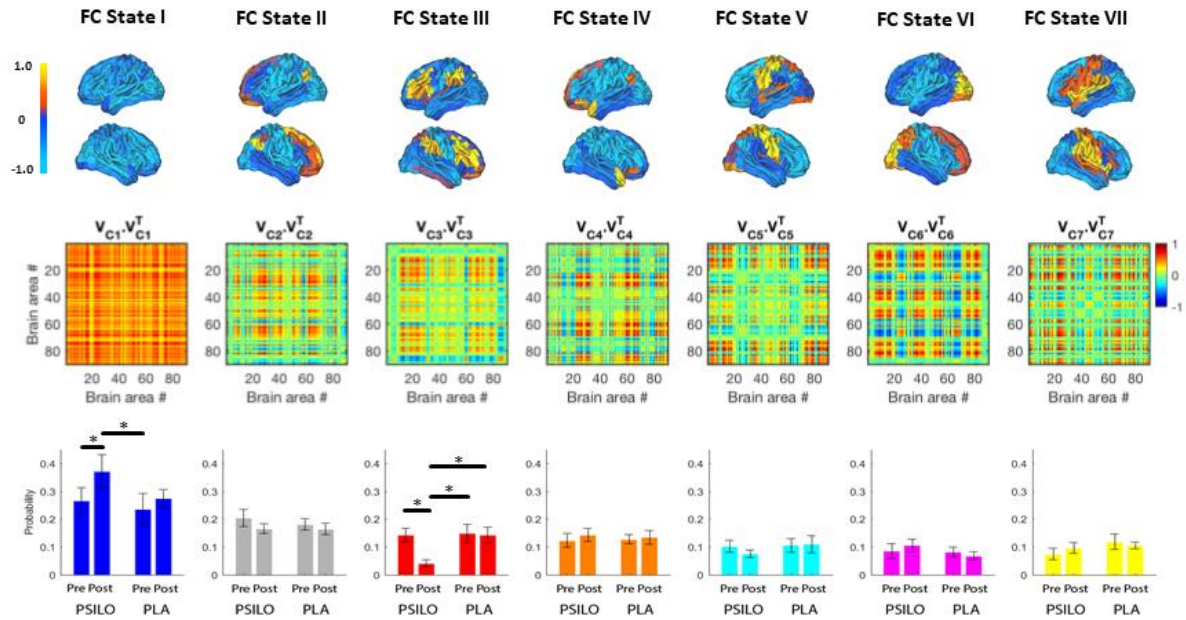


Figure 4.3. Dynamical exploration of the repertoire of FC states altered by psilocybin. *Seven recurrent FC states were obtained from unsupervised clustering of the eigenvectors of the dynamic functional connectivity, sorted (left to right) according to decreasing probability of occurrence before injection. Each FC state is represented as;* Top: *cortical renderings in AAL space of regional contributions to the respective V_C;* Middle: *a matrix obtained by calculating the outer product of V_C, where positive values are the product of V_C elements with the same sign, be they positive or negative;* Bottom*: Probability of occurrence (mean ± standard error of the mean across subjects) of each FC state in each of the four experimental conditions (pre/post psilocybin and pre/post placebo injection). One FC state (here FC state III, red bars) significantly decreases in probability from 14.3% before injection to 4.1% after the injection of psilocybin (p = 0.00034). Conversely, the probability of occurrence of FC state I increased after psilocybin injection (p = 0.0068). All other FC states did not change in probability with psilocybin. Asterisks denote the presence of a statistically significant differences upon correcting for multiple comparisons, surviving the significance threshold $\alpha_2 = 0.05/k$.*

Comparing with the separate fMRI session when a placebo solution was injected, the probability of occurrence of all seven FC states both before and after placebo injection did not differ significantly from the pre-psilocybin condition (all p-values > 0.05), indicating that the dynamical exploration of FC states assessed with LEiDA remained stable across subjects under normal conditions across different scanning sessions. These FC states show

spatial overlap with well-known resting-state networks, namely the default mode network (FC states II and IV), the fronto-parietal control network (FC state III), the somatosensory network (FC state V), the visual network (FC state VI) and the auditory network (FC state VII) (Figure 4.3). Corroborating our previous findings, the fractional occupancy of FC state III remained within normal levels both before (15.0 ± 3.3%) and after (14.3 ± 2.9%) placebo injection ($p = 0.49$; uncorrected), and was in each case significantly higher than the probability found during the psychedelic state (4.1 ± 1.2%, $p = 0.004$ and $p = 0.001$ respectively, Bonferroni corrected). Moreover, the fractional occupancy of FC state I, which was significantly increased after the psilocybin injection as stated above, remained unchanged before (23.6 ± 5.6%) and after the placebo injection (27.4 ± 3.1%) ($p = 0.38$; uncorrected). When compared to the post-psilocybin fractional occupancy of FC State I (37.2 ± 6.0%), the aforementioned pre-placebo value was also significantly higher ($p = 0.006$; Bonferroni corrected) while the post-placebo comparison was borderline significant after correction for multiple comparisons ($p = 0.07$; Bonferroni corrected) (Figure 4.3).Please note that the FC state whose probability of occurrence was significantly reduced following the psilocybin injection closely overlaps with the fronto-parietal network involved in executive control originally reported by Vincent and colleagues (Vincent, Kahn et al. 2008), which includes many regions identified as supporting cognitive control and decision-making processes such as the lateral prefrontal cortex and inferior parietal lobule (Figure 4.4).

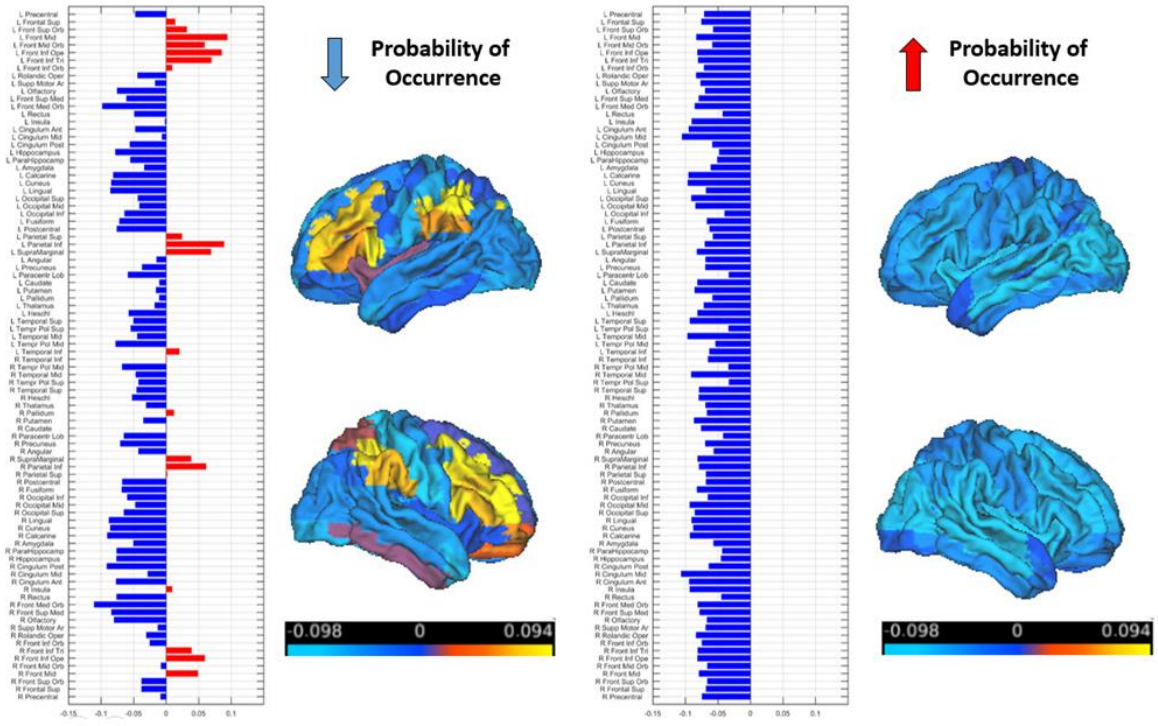


Figure 4.4. Characterization of the FC states whose probability of occurrence are altered by psilocybin. Left: *Bar chart representing contributions of each of the N=90 AAL brain areas to the FC state III cluster centroid vector whose probability of occurrence is significantly decreased after the psilocybin infusion ($V_c(n)>0$ in red, blue otherwise), and rendition of the relevant cluster centroid vector V_c onto a cortical surface, highlighting the symmetry of the network of interest across both hemispheres. This particular FC state shows a strong overlap with the fronto-parietal control system (Vincent, Kahn et al. 2008)* Right: *Bar chart representing contributions of each of the N=90 AAL brain areas to the FC state I whose probability of occurrence is significantly increased after the psilocybin infusion, and rendition of the relevant cluster centroid vector V_c onto a cortical surface. It can be observed that FC state I corresponds to a globally coherent functional network state in which most brain areas are in phase with each other.*

The non-stationary dynamics of the leading eigenvector over time revealed a constant exploration of a repertoire of FC configurations. In order to visualize this repertoire in a 3-dimensional space, a PCA reduction was applied to all leading eigenvectors across conditions and subjects (90x36000) to their first 3 Principal Components (3x36000). Then, the leading eigenvectors $V_1(t)$ obtained in each of the four experimental conditions were plotted as dots in this 3D space and coloured according to the label assigned by the clustering algorithm. As can be seen in Figure 4.5 there is little overlap between clusters, and all clusters are distributed around the state of global integration (blue dots). By construction, the *k*-means clustering algorithm produces compact clusters (i.e. non-overlapping and well separated). However these clusters originally exist in the 90 dimensional space where the leading eigenvectors live. Retaining only the first 3 principal components is, however, sufficient to conserve well-defined clusters.

This visual rendition of the data highlights the disruption of the fronto-parietal FC state (red cluster), which is clearly prevalent in the three non-psychedelic conditions (before psilocybin and before/after placebo injection), but nearly disappears after the psilocybin injection. It can also be seen that the blue cluster corresponding to a globally coherent FC state becomes denser after the psilocybin injection, but unchanged in the placebo condition.

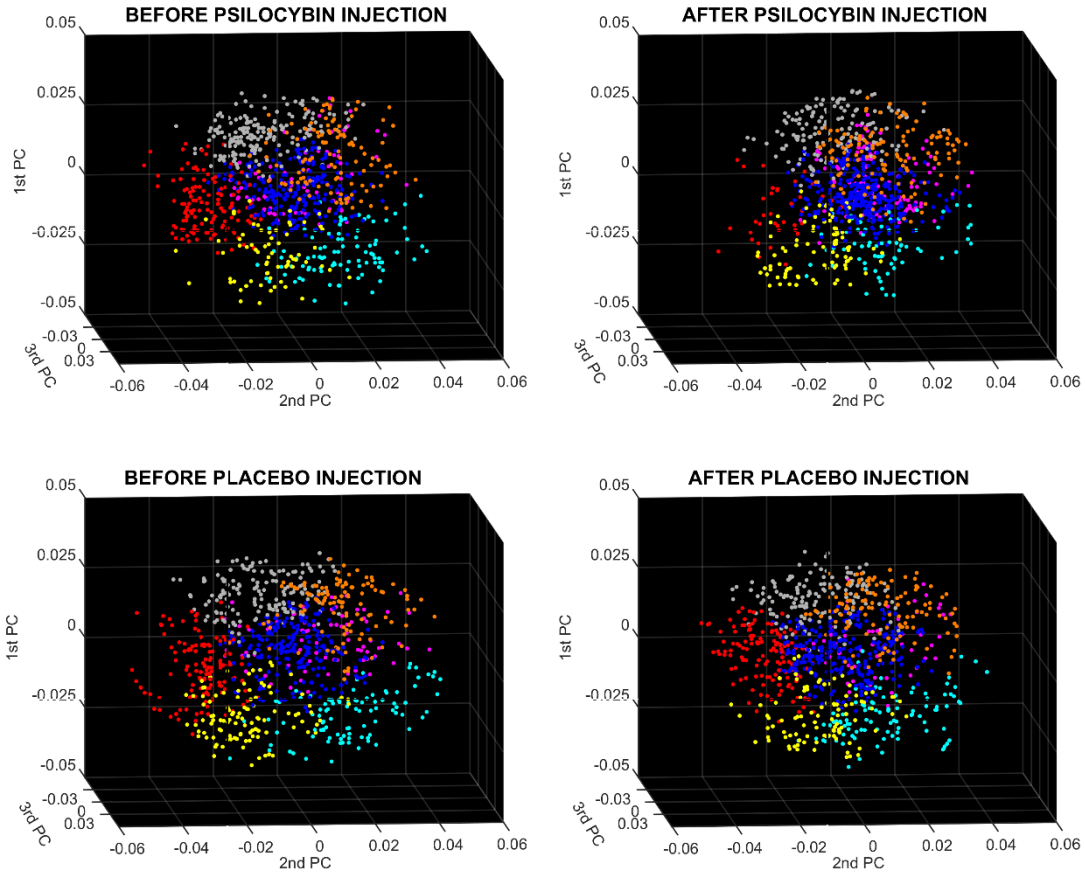


Figure 4.5. 3D embedding of FC patterns. *In each scatter plot, each dot represents an FC pattern, V_1(t), occurring during the corresponding scanning session (before/after psilocybin & placebo, with 900 dots per subplot), projected onto the first 3 principal components of all eigenvectors across sessions (PCA-reduced from 90x3600 to 3x3600). Dots are coloured according to the* k*-means clustering solution obtained before, using the same color code as in Figure 4.2. It can be clearly observed that after the psilocybin injection the number of red dots is reduced indicating a lower occurrence of the frontal-parietal network (FC state III). Meanwhile, the network in the center of the 3D scatter plots which corresponds to a globally coherent state (FC state I in blue) becomes more prominently expressed following the psilocybin injection. The fractional occupancy of the other FC states remains stable across all conditions.*

4.3.2 Psilocybin modulates the temporal expression of FC States

I then plotted, for each subject, the evolution of the order parameter (OP) of the system at each of the 100 time points pre/post-psilocybin injection, as calculated in the previous Chapter (Section 3.2.5), as well as the corresponding leading eigenvector $V_1(t)$ color-coded according to their respective cluster assignment (Figure 4.6). In all subjects,

the eigenvector corresponding to the globally coherent state (first state from top; blue coloured) is the most frequently expressed both before and after the psilocybin injection, and its fractional occupancy is particularly elevated in subjects with the highest average order parameter (OP) values over time. I further found that, with the exception of subject *s1*, the fronto-parietal FC state (3rd state from top; red-coloured) was approximately evenly expressed in all subjects in the pre-injection phase. Following the psilocybin injection, the fractional occupancy of this state was reduced in all subjects. In the case of subjects *s4* and *s9*, not a single $V_1(t)$ in the post-psilocybin injection condition belonged to the fronto-parietal FC state. This was indeed the only FC state where a fractional occupancy of zero was found amongst all subjects and experimental conditions in this analysis. A paired t-test revealed that, at the individual subject level, the mean number of occurrences of FC state III (fronto-parietal network) was significantly decreased following the psilocybin injection (4.1 ± 1.2) relative to the pre-injection baseline (14.3 ± 2.5); $t(8) = 3.88$, $p = 0.005$). Conversely, a paired-sample t-test showed a significant *increase* in the mean number of occurrences of FC state I (globally integrated state) following the psilocybin injection (37.2 ± 6.0) relative to the pre-injection baseline (26.7 ± 4.5); $t(8) = 2.75$, $p = 0.01$.

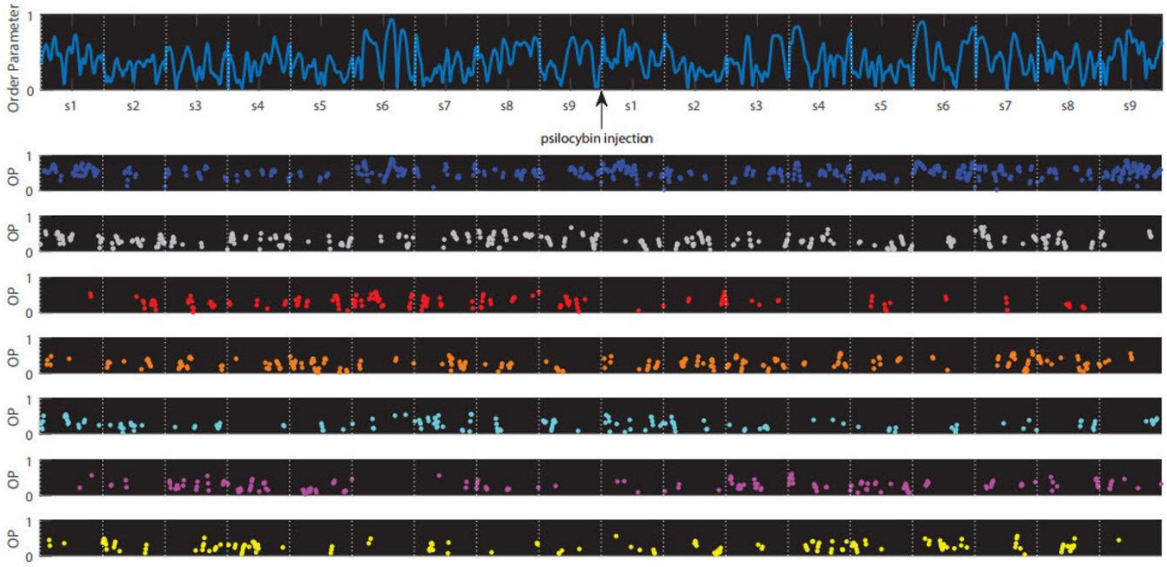


Figure 4.6. Psilocybin modulates the temporal expression of FC States. Top: *For each of the 9 subjects (*s1, s2… s9*), the order parameter (OP) of the system over time pre/post-psilocybin injection (100 TR/ subject/condition) separated by the vertical dashed white lines. The panel immediately below shows the order parameter when each of the seven FC states in ON (same color-code as Figure 4.2, sorted vertically by decreasing probability pre-injection). In all subjects, the FC state corresponding to the globally synchronized state (blue coloured) is the most frequently expressed at baseline, and the order parameter is particularly high when this state is ON. On the other hand, less frequently visited states, namely the light blue, purple, or yellow, correspond to epochs of lower OP values. Following the psilocybin injection, the red-coloured fronto-parietal FC state of interest (3rd most prevalent state pre-injection) exhibits a large decrease in fractional occupancy in nearly all subjects. Conversely, the occurrence of FC state I, which is already the most prominent at baseline, increases even more following the psilocybin injection in most subjects.*

4.3.3 State-to-State switching profiles are significantly different under psilocybin

The switching matrices shown in Figure 4.7 (top) display the probability of: 1) being in a given FC state (rows), and 2) transitioning to any of the other states (columns) both before and after the psilocybin injection. An illustration of pre- vs post-injection changes in the transitions probabilities between FC-states rendered on the cortical surface is also provided to facilitate the neuroanatomical interpretation of FC state switching (Figure 4.7, bottom). The probability of transitioning from any given FC state to the fronto-parietal FC state of interest is consistently reduced post-psilocybin injection compared to the pre-injection condition. Conversely, all FC states except for one were more likely to transition toward the FC state corresponding to the global signal following the psilocybin injection. The *p*-values for each state-to-state transition in the switching matrix are provided in Table 4.1.

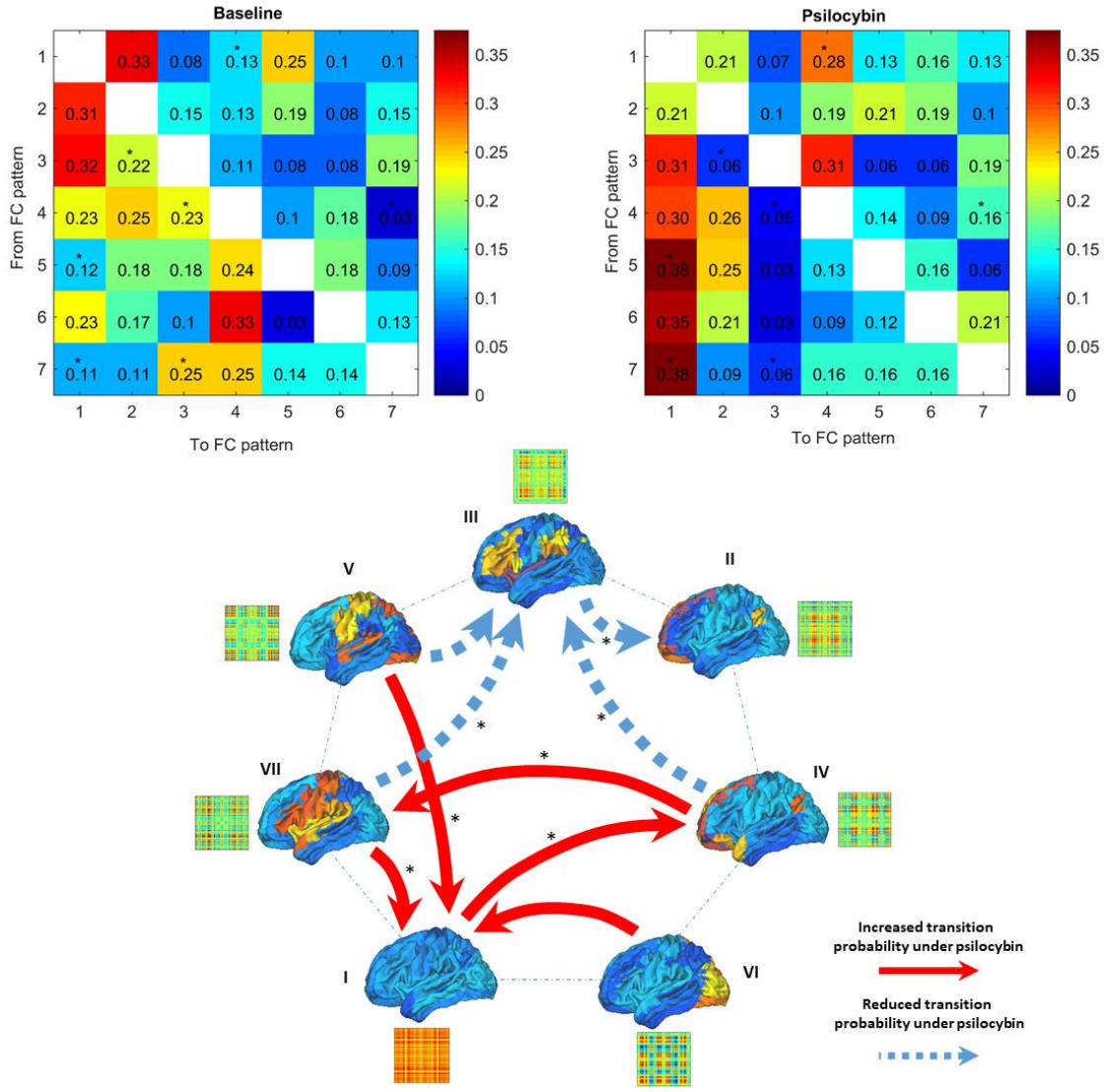


Figure 4.7. Psilocybin modifies the switching patterns between FC-states. Top: *Switching matrices showing the probability of, being in a given FC state (rows), transitioning to any of the other states (columns) both before (left) and after the psilocybin injection (right). Significant between-condition differences assessed via a permutation test are indicated by asterisks (*) for the significance threshold α = 0.05.* Bottom: *Pre vs post-injection changes in the transition probabilities between FC-states rendered on the cortical surface, and numbered according to the transition matrices above. Each arrow represents a state-to-state transition probability ± 1 SD from the mean change in transition probability seen post-injection; red/filled arrows represent a higher probability of transition post-injection, while blue/dashed arrows show reduced transition probabilities between states post-injection. It can be observed that the probability of transitioning from several FC states (*IV, V, VII*) to the frontoparietal FC state of interest is reduced post-psilocybin injection. Conversely, most FC states (*IV, V, VI, VII*) were more likely to transition toward the globally integrated FC state I following the psilocybin injection.*

	I	II	III	IV	V	VI	VII
I		0.399	0.408	0.000	0.285	0.095	0.146
II	0.082		0.216	0.261	0.499	0.114	0.095
III	0.184	0.006		0.355	0.069	0.079	0.069
IV	0.217	0.426	0.002		0.247	0.077	0.041
V	0.006	0.171	0.038	0.145		0.366	0.380
VI	0.173	0.285	0.250	0.055	0.116		0.198
VII	0.042	0.494	0.040	0.176	0.397	0.388	

Table 4.1. Statistical testing results. *The p-values for each entry of the switching matrix between FC states shown in Figure 4.7.*

4.4 Discussion

The present results provide the first experimental evidence that the brain's dynamical landscape is altered by the psychedelic compound psilocybin. The probability of occurrence of functional connectivity networks at rest (described as "FC states"), and the transitions between them, are significantly changed by the drug. Notably, the strongly reduced fractional occupancy of a FC state overlapping with the previously described fronto-parietal control system suggests that this particular functional network becomes destabilized under psilocybin (Vincent, Kahn et al. 2008). Conversely, transitions toward a globally integrated FC state were enhanced under the influence of the drug. The joint destabilization of a frontoparietal FC state supporting executive function, and increased transitions toward a highly integrated brain state provide a novel mechanistic perspective into psilocybin's effects at the system level. Indeed, these differences between brain state trajectories in normal waking consciousness and the psychedelic state suggest that the drug may induce an alternative type of functional integration at the expense of locally segregated activity in specialized networks.

The decreased probability of occurrence of a FC state closely overlapping with the fronto-parietal control system is consistent with prior human neuroimaging studies of psilocybin. An fMRI study of the same dataset notably revealed that the psilocybin infusion modified the BOLD spectral content in a distributed fronto-parietal network. Specifically, the fronto-parietal system of interest showed significantly decreased low frequency power and power spectrum scaling exponent following the psilocybin infusion (Tagliazucchi, Carhart-Harris et al. 2014). Similarly, a MEG study reported decreased oscillatory power following a psilocybin injection in a bilateral fronto-parietal network derived from beta-

band activity (Muthukumaraswamy, Carhart-Harris et al. 2013). Findings from these prior studies indicate a desynchronization of the fronto-parietal control system under psilocybin and are thus consistent with the present results. Furthermore, the disengagement of the fronto-parietal system can be interpreted in light of the cognitive and behavioral effects of psilocybin reported by study participants. Previous studies suggested that the fronto-parietal system plays a key role in cognitive control by focusing attention on goal-relevant information through top-down mechanisms (Cole and Schneider 2007, Dosenbach, Fair et al. 2008, Xin and Lei 2015). Declines in fronto-parietal FC have been associated with difficulty suppressing goal-irrelevant information, and greater distractibility (Smallwood, Brown et al. 2012). These observations are therefore broadly consistent with the reports of increased mind-wandering and unconstrained cognition reported by participants in the present fMRI experiment (Carhart-Harris, Erritzoe et al. 2012).

The present study also found increased FC state transitions toward a globally synchronized functional network following the psilocybin injection. Previous time-averaged functional connectivity analyses of the same fMRI dataset have shown that psilocybin induces an alternative type of functional integration, characterized by greater global integration (Petri, Expert et al. 2014, Roseman, Leech et al. 2014) as well as increases in the entropy or metastability of brain states (Carhart-Harris, Leech et al. 2014). The results presented here not only align with these prior findings but also shed further light on their functional significance. A globally integrated state, i.e. FC state I, increased its predominance under psilocybin, not only statistically over time, but also dynamically, as was evident from the structure of the state-to-state switching matrix, where it became the "state of choice" for inter-state transitions. In other words, under psilocybin the brain spent more time in globally coherent, highly integrated state. This state therefore served as an attractor, absorbing the majority of inter-state transitions. As was implied by previous analyses, this effect may enable atypical patterns of interregional communication to arise in the psychedelic state (Petri, Expert et al. 2014) alongside the breakdown of within-network integrity in favor of globally integrated brain dynamics (Muthukumaraswamy, Carhart-Harris et al. 2013, Carhart-Harris, Leech et al. 2014, Petri, Expert et al. 2014, Roseman, Leech et al. 2014, Tagliazucchi, Roseman et al. 2016).

A limitation of the present study is the relatively small number of subjects (n=9) included in this fMRI dataset. The present findings are nevertheless strongly validated by the replication of results in placebo conditions across two separate scanning days (i.e. no

changes in the distribution of network states in the placebo scanning session vs pre-psilocybin infusion). The preserved sensitivity of the analysis in this small sample of subjects may be attributed to the fact that LEiDA compares the statistics between whole-brain FC patterns rather than individual functional links, and therefore the dimensionality is reduced from N(N-1)/2 (number of unique links in a NxN symmetric matrix) to the number of networks *k*, which overcomes several of the statistical limitations associated with multiple comparisons. Moreover, the LEiDA analysis strictly considers the leading eigenvector of the dFC matrix which likely has a de-noising effect, whilst consistently explaining most of the variance in the phase coherence matrix, as demonstrated above (Figure 4.1). Finally, given the instantaneous nature of LEiDA, our dynamic FC analysis revealed significant between-condition differences despite the fact that each experimental condition consisted only of 100 fMRI volumes, which would likely not have been sufficient for conventional sliding-window analysis (Hindriks, Adhikari et al. 2015).

Since the BOLD signal indirectly measures low frequency neural oscillations (typically < 0.1Hz), the present analysis cannot capture the fast dynamics of functional networks which are believed to have lifetimes of approximately 200ms as suggested by MEG studies (Baker, Brookes et al. 2014, Vidaurre, Quinn et al. 2016), but still captures changes in their probability of occurrence over slower time scales. Indeed the methodological limitations inherent to the use of the BOLD signal to estimate brain dynamics previously discussed in Section 3.4 also apply here. A final limitation of the LEiDA method is the reliance of the *k*-means clustering algorithm on inputting a desired number of clusters *a priori*. To avoid biasing the analysis by considering a unique *k*-value, I scanned a large number of *k* parameter values as described above ($k = 2$ to $k = 20$), and looked for FC-patterns (i.e. cluster centroid eigenvectors) that reached a statistically significant difference in their probability of occurrence in the pre/post-psilocybin conditions after the correction for multiple comparisons for a given *k*. Using this approach I found the strongest statistical effects for the decrease in fractional occupancy of FC State III and increase fractional occupancy of FC State I for the clustering solution with 7 clusters. I then also examined the cluster centroid eigenvectors for neighboring *k*-values ($k = 6$ to $k = 10$ range) and found that statistically significant differences pre/post psilocybin infusion were also observed for closely matching FC-patterns. Moreover, the regional contributions to the corresponding cluster centroid eigenvectors were remarkably consistent in this parameter range for the FC states of interest despite the different numbers of states being detected by

the clustering algorithm (see Supplementary Figures 2 and 3). I am therefore highly confident that the present results are generalizable beyond a fixed number FC states.

4.5 Chapter Summary

In summary, I have applied a data-driven dynamical functional connectivity analysis (LEiDA) to fMRI data to help uncover the dynamics between FC states under the influence of the classical serotonergic psychedelic psilocybin. FC states were extracted by applying unsupervised clustering to the set of leading eigenvectors of dynamic FC matrices, defined here as the instantaneous phase coherence matrix at individual TRs. A FC state closely corresponding to the fronto-parietal control system was acutely destabilized by the drug, while transitions toward a globally synchronized FC state were enhanced. This supports the idea that changes in the brain's dynamical landscape underlie the psychedelic experience in a manner which biases global integration at the expense of segregated dynamics in functionally specialized networks, such as the fronto-parietal control system.

Chapter 5: Local vs Global Integration in Altered States of Consciousness: System-wide consequences of intrinsic perturbations

5.1 Introduction

A potentially promising experimental strategy for investigating the integration/segregation balance is to examine how external inputs are processed dynamically at the whole-brain scale, either *in vivo* or *in silico*. As discussed earlier (see Introduction 1.2.3), cleverly designed experiments in which a TMS pulse (i.e. an exogenous perturbation) is applied to the cortex and the stimulus-evoked EEG responses are then measured have provided experimental evidence that both the range of the elicited patterns of activation across the brain, and the complexity of the resulting electrocortical responses are reduced in slow-wave sleep and anesthesia compared to wakefulness (Massimini, Ferrarelli et al. 2005, Casali, Gosseries et al. 2013).

That extrinsic perturbations lead to disrupted patterns of information propagation in behavioral states characterized by diminished consciousness raises the interesting possibility that naturally occurring *intrinsic* perturbations within the system may be similarly affected. Accordingly, the propagation of local activity signals across the system may be different in N3 sleep and/or the psychedelic state relative to baseline. To characterize the broadcasting of information from a local node through the rest of the network, (i.e. local vs global integration), I used a novel "intrinsic ignition" framework developed by Deco & Kringelbach, which refers to the capability of a given local node (brain area) to propagate neuronal activity to other nodes in the network, hence describing the whole-brain integration elicited from the propagation of both feedforward and recurrent activity in a particular brain state (Deco and Kringelbach 2017). As described further below, such "ignition events" at a given node may be defined in a binary fashion when the regional activity signal peaks above a certain threshold. The elicited propagation of the local signal across the network giving rise to different levels of integration may then be quantified and referred to as the "ignition-driven integration" (IDI). The mean of the IDI (averaged across all ignition events for a node) would reflect the amount of integration that is typically elicited by intrinsic ignition events; whilst the standard deviation of this same quantity would reflect the computational spatiotemporal diversity of a network node over time.

This Chapter investigated the intrinsic ignition profiles of brain areas in two altered states of consciousness: slow-wave sleep, and the psychedelic state. I analyzed separate fMRI datasets from healthy participants collected during a resting-state baseline and subsequently during: i) N3 sleep and ii) a psychedelic experience experimentally induced by a psilocybin infusion. In light of the aforementioned results from perturbational studies in sleep and anesthesia, I hypothesized that the intrinsic ignition events detected during N3 sleep would, on average, elicit less integration across the network compared to wakeful rest. Conversely, I expected that individual brain regions would, on average, be more likely to propagate local signals globally in the psychedelic state, consistent with previous neuroimaging results indicative of enhanced global and cross-modular integration (Petri, Expert et al. 2014, Roseman, Leech et al. 2014, Tagliazucchi, Roseman et al. 2016) (See Introduction 1.3.2).

5.2 Methods

5.2.1 Participants, Experimental Protocol, Neuroimaging Data Acquisition & Processing

These subsections of Methods for both the sleep and psychedelic fMRI studies were previously described in Sections: 3.2.1, 3.2.2 and 3.2.3 respectively.

5.2.2 Integration-Driven Integration (IDI) and Integration-Driven Variability (IDI-variability)

An intrinsic ignition event for a given brain region r is defined by binarizing the transformed BOLD fMRI time series into z-scores $z_r(t)$ and imposing a threshold θ such that the binary sequence $\sigma_r(t) = 1$ if $z_r(t) > \theta$ and is crossing the threshold from below; and $\sigma_r(t) = 0$ otherwise. In this case, I used the mean over regional signal values as the threshold (θ), consistent with previous functional neuroimaging studies using point processes (Schartner, Carhart-Harris et al. 2017). This outcome of this thresholding procedure is represented graphically in Figure 5.1 where I show the binarized presence (or absence) of driving events over time at each node in different experimental conditions for a single subject. I then constructed an "events matrix" for the integration time-window of width $T = 3 * TR$ which immediately follows each driving event. For each time point T_i within this time window, I computed the number of coinciding events $N_r(T)$ across the entire network where $\sigma_i(t) = 1$. The selection of this window width was determined by the time that takes the integration to return to basal values in a previous study (Deco, Tagliazucchi et al. 2017). The maximum value within this set is then considered as the Ignition-Driven-Integration (IDI) of a particular event:

$$IDI(r,T) = \{N_r\}_{i=1}^{T}$$

To compute the *IDI* of a given brain area *for the entire recording interval*, we simply take the mean of the $IDI(r,T)$ across all the driving events $\sigma_i(t) = 1$ detected for that node. The procedure is summarized graphically in Figure 5.2. Similarly, the *variability* of the IDI for a given node can be computed by taking the standard deviation of $IDI(r,T)$ over time. Finally, whole-brain measures of *IDI* and *IDI-variability* can be intuitively derived by averaging the above regional measures across all the network nodes for a given subject.

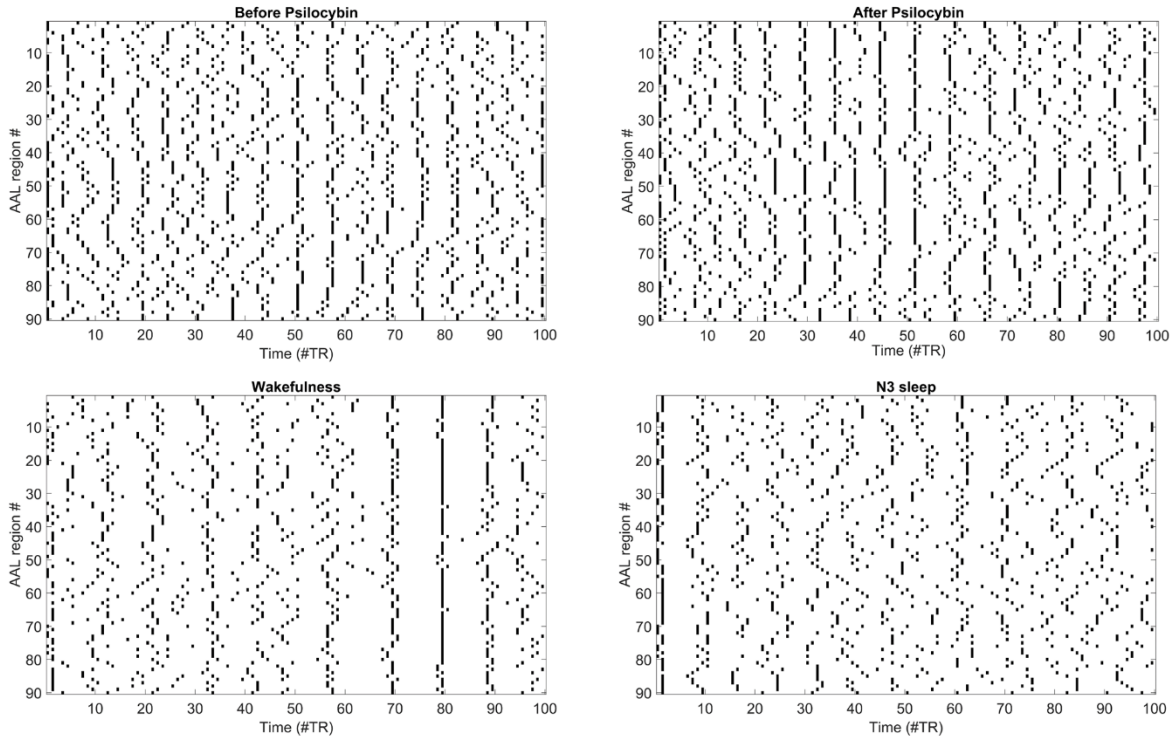


Figure 5.1. Graphical representations of ignition events resulting from the binarization of BOLD signals. Top: *Representative plot of ignition events across regions (y-axis) and over time (x-axis) for a single study participant before (left) and after (right) the psilocybin injection.* Bottom*: Same as above, but depicting the ignition events during wakefulness (left) vs N3 sleep (right). It can be qualitatively observed that "cascades" of coinciding ignition events covering most of the brain are observed more frequency in the psychedelic state than the resting-state baseline. Conversely, coinciding ignition events are less frequently observed in N3 sleep than wakeful rest in this subject, and ignition events appear more scattered over time in N3 sleep upon visual inspection of the data.*

5.2.3 Surrogate Analysis

In order to assess the validity of our method, I tested whether the IDI and IDI-variability values were smaller than in the empirical data when derived from timeseries with randomly shuffled driving events. To create the surrogate data, the spontaneous events are changed to random temporal locations (random permutation) and then computed the IDI and IDI variability values associated to them. This procedure is then repeated 50 times, and I

compared the average of the values derived from the scrambled events to those values after spontaneous events in the original data using a paired t-test.

5.2.4 Between-Condition comparisons:

Whole-brain IDI and IDI-variability scores were computed as indicated above at the single subject level. For the sleep study, I used a paired t-test to assess changes on each measure in wakeful rest vs N3 sleep ($\alpha = 0.05$). For the psilocybin study, I used a paired t-test to compare these measures in the pre/post psilocybin condition, and separately in the pre/post-placebo condition. *Regional* IDI and IDI-variability were computed at the single-subject level and compared on a region-by-region basis (n = 90) across conditions using paired t-tests and correcting for multiple comparisons using the FDR procedure (Benjamini and Hochberg 1995).

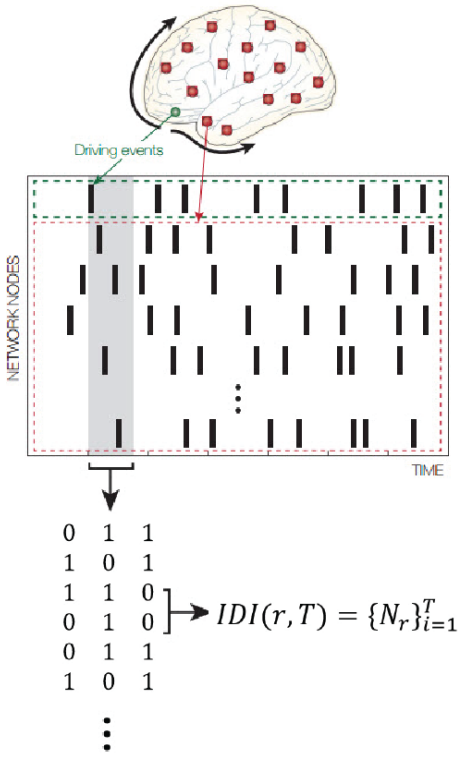


Figure 5.2. Schematic of the intrinsic-driven-integration (IDI) calculation. *The spiking activity of a given brain region (green square) is scanned for driving events meeting the thresholding criteria described above. Following each driving event, the activity is measured in the rest of the network (red squares) in the gray time window of length T = 3TRs. This can be summarized in a binary "events matrix" (ROI# x T). For each time point T_i within this time window, we compute the number of coinciding events $N_r(T_i)$ across the entire network where $\sigma_i(t) = 1$ and the largest values within this set, $\{N_r\}_{i=1}^{T}$ corresponds to the IDI for the driving event. We then simply take the mean or standard deviation of $IDI(r,T)$ across all the driving events $\sigma_i(t) = 1$ detected for that node over the recording interval to compute the regional IDI and regional IDI-variability respectively.*

5.3 Results

5.3.1 Psilocybin Study

5.3.1.1 Global measures:

The global IDI (i.e. IDI averaged across all nodes) was significantly increased (+6.6%) following the psilocybin infusion relative to the pre-injection baseline; t(8) = 2.68, p = 0.028. This indicates that, on average, $IDI(r,T)$ is higher across the network and larger numbers of coinciding regional activity "peaks" occur following an ignition event under the psilocybin condition within an integration time window T. An even larger increase in global IDI-variability (+17.5%) was also observed after the injection relative to baseline, suggesting that the size of the integration cascades following ignition events become more variable under psilocybin; t(8) = 4.51, p = 0.002. Conversely, no significant difference was observed pre/post placebo injection on either the global IDI (t(8) = 0.43, p = 0.68) or global IDI-variability measures; t(8) = 0.05, p = 0.96. Finally, as anticipated the IDI and IDI variability measures computed from the surrogate (scrambled) timecourses were significantly lower than those measures calculated from the experimental data in each condition under study (all p-vals < 10^{-5}). These results are shown graphically in Figure 5.3 (top panel).

5.3.1.2 Regional measures:

Let us now consider between-condition differences in *regional* IDI and IDI variability averaged across subjects. Whilst IDI was consistently higher in most regions in the post-psilocybin condition relative to the pre-injection baseline (as reflected by the significant increase on the *global* IDI measure post-psilocybin infusion), significant regional IDI increases surviving the FDR correction for multiple comparisons were observed in only two AAL regions; the right anterior cingulate gyrus (AAL #32) and right inferior frontal gyrus (AAL #16). The regional IDI-variability measure was more strongly affected by the psilocybin manipulation where 15 nodes showed a significant increase surviving the correction for multiple comparisons (Figure 5.3). As shown graphically in Figure 5.4, nodes showing significantly increased IDI-variability were mostly found in the frontal and temporal cortices and notably included the bilateral insula, bilateral anterior cingulate and bilateral fusiform gyrus. On the other hand, no significant difference in regional IDI or IDI-variability were observed pre/post placebo infusion (Figure 5.3, bottom panel). The p-values for regional comparisons of IDI and IDI-variability in each experimental condition are included in Supplementary Table 2.

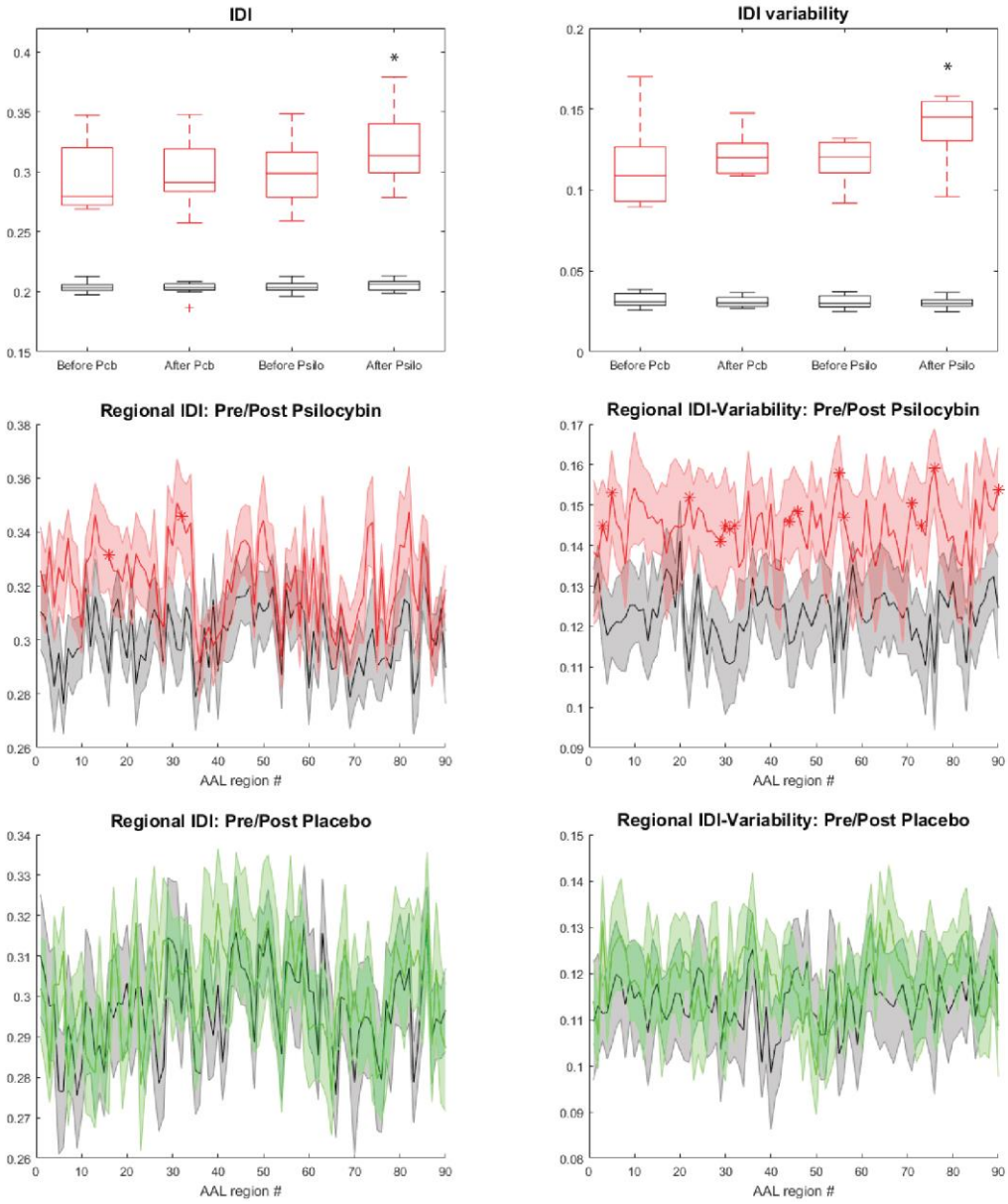


Figure 5.3. Global and Regional IDI & IDI-variability: Psilocybin study. Top: *Between-condition comparisons on the global IDI (left) and IDI-variability (right) measures. IDI and IDI-variability are each significantly increased post-psilocybin infusion relative to the pre-injection baseline (*denotes $p < 0.05$), but no significant change on these global measures is seen pre vs post-placebo infusion.* Middle*: Regional IDI (left) and IDI-variability (right). The black line represents pre-psilocybin injection scores and the red line post-psilocybin scores ± standard deviation (shaded area). Regional IDI is increased across most brain regions post-psilocybin, but the between-condition comparison only survives the FDR correction for multiple comparisons for the right anterior cingulate gyrus and right inferior frontal gyrus (AAL# 16 and #32, respectively). A stronger effect is observed post-psilocybin infusion on the IDI-variability measure, where a clear separation between the two lines can be seen. The increase is statistically significant for 15 brain regions, mostly located in the frontal and temporal cortices (see Figure 5.4).* Bottom*: Same as middle but here the black line represents the pre-placebo injection condition and the green line shows the post-placebo injection regional scores. Both IDI and IDI-variability are unaffected in the placebo injection condition relative to baseline, as the clear overlap between the lines reflects. No statistically significant regional difference on IDI or IDI-variability were found pre vs post-placebo injection.*

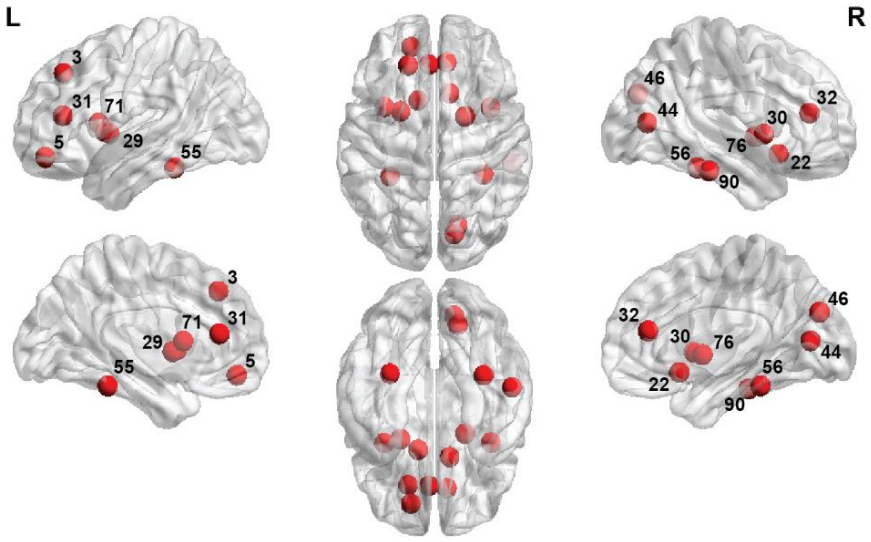


Figure 5.4. Nodes showing significant increases in IDI-variability under psilocybin. *Fifteen nodes showed a statistically significant increase on the IDI-variability measure after the psilocybin infusion relative to baseline, surviving the FDR correction for multiple comparisons. These were mostly found in the frontal and temporal cortices and notably included the bilateral insula (#29, #30), bilateral anterior cingulate (#31, #32) and bilateral fusiform gyrus (#55, #56). This indicates that the broadcasting of local signals from these areas becomes more variable over time following the psilocybin infusion. Corresponding AAL region labels are included in Supplementary Table 1.*

5.3.2 Sleep Study

5.3.2.1 Global measures:

In contrast with the psilocybin results, the global IDI was significant *decreased* in N3 sleep relative to wakeful rest (-19.5%); $t(17) = 3.84$, $p = 0.0013$. Similarly, the global IDI-variability was also significantly decreased (-25.3%) during the slow-wave sleep condition; $t(17) = 3.92$, $p = 0.0011$. The IDI and IDI-variability measures calculated from surrogate data for both the wakeful rest and N3 sleep conditions were significantly lower than those measured in the empirical data (both p-vals $< 10^{-6}$) (Figure 5.5, top panel).

5.3.2.2 Regional measures:

For every network node, the IDI was significantly lower in N3 sleep than the wakeful rest condition and survived the FDR correction for multiple comparisons (all p-vals < 0.04). Similarly, the regional IDI-variability was significantly reduced in N3 sleep relative to baseline in all the nodes (all p-vals < 0.03). This indicates that, on average, integration cascades following a driving event cover less of the network in slow-wave sleep than wakefulness and their size is also less variable over time (Figure 5.5, bottom panel). The p-

values for each regional comparison between experimental conditions are listed in Supplementary Table 3.

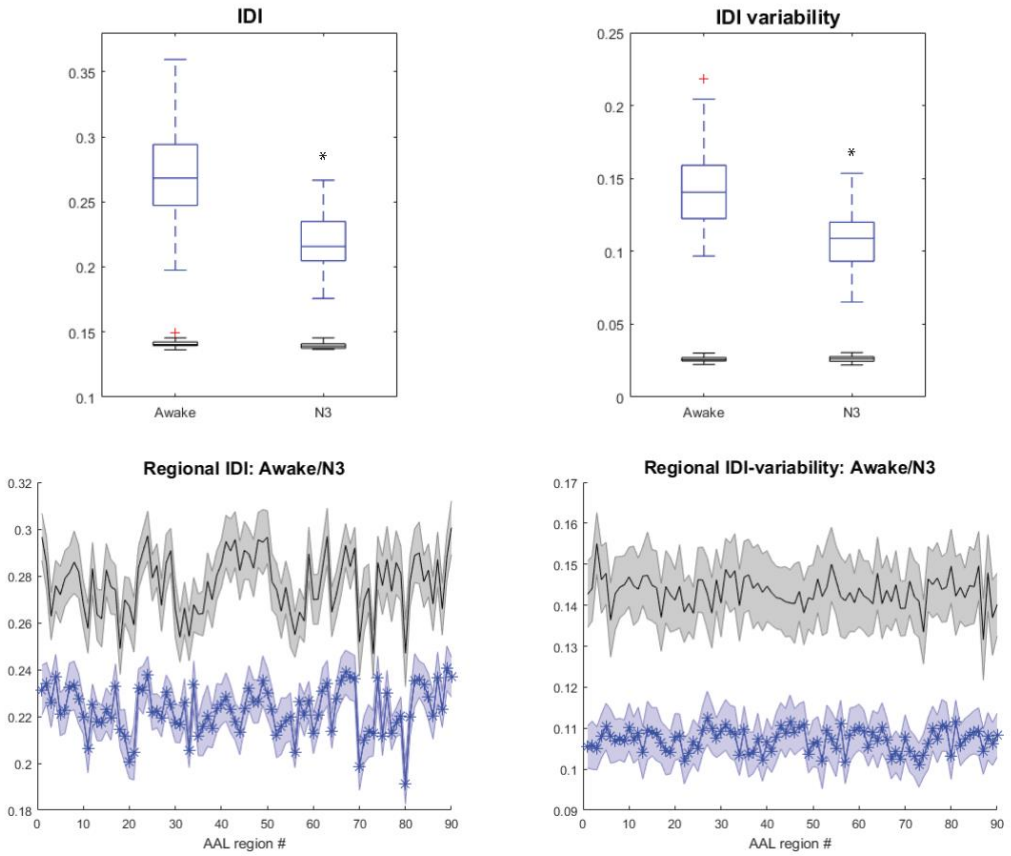


Figure 5.5. Global and Regional IDI and IDI-variability results: Sleep study. Top: *Between-condition comparisons on the global IDI (left) and IDI-variability (right) measures. Global IDI and IDI-variability are each significantly decreased in N3 sleep relative to wakeful rest (statistical significance denoted by *).* Bottom*: Regional IDI (left) and IDI-variability (right) ± standard deviation as shaded area. The black line represents the wakeful rest baseline and the blue line N3 sleep scores. Regional IDI and IDI-variability are both significantly decreased across every brain region in N3 sleep relative to wakeful rest. This suggests that, during slow-wave sleep, the broadcasting of regional signals tends to remain more local, and a less flexible functional architecture is also observed.*

5.4 Discussion

In this Chapter, I have used a novel "intrinsic ignition" method for characterizing brain information propagation patterns in two altered states of consciousness: slow-wave sleep and the psychedelic state. I have shown that differences between the intrinsic ignition profiles of the network nodes provide a sensitive marker for these brain states, differentiating each of them from wakeful rest. Specifically, intrinsic ignition events lead to greater propagation of local signals across the rest of the network under psilocybin relative to the pre-injection baseline, as estimated by the ignition-driven integration (IDI) averaged over

time. Conversely, the global integration elicited by local ignition events is decreased in N3 sleep relative to wakefulness. I also considered the variance in the propagation of local signals across the network elicited by ignition events as an estimate of the dynamical complexity of a given brain state. A global increase on the IDI-variability measure in the psychedelic state relative to baseline was found and, by contrast, a decrease in N3 sleep compared to wakeful rest.

Whilst the most precise spatiotemporal information about brain dynamics arguably comes from recording the spiking activity of individual neurons, the definition of a "brain state" must almost certainly consider the relationship between local and non-local interactions, as individual neurons maintain sophisticated connection patterns giving rise to structural and functional networks. The intrinsic ignition framework introduces a definition of a brain state based on the system's dynamical complexity and broadness of communication, which in turn enables different levels of integration and segregation of information processing at the whole-brain scale. The intrinsic ignition framework thus characterizes the dynamical integration/segregation balance by describing how activity in a local region shapes global activity, and the way in which the broadness of communication is elicited and distributed over time (Deco, Tagliazucchi et al. 2017). This is complementary to the methods used in the preceding chapters which respectively leveraged on the topological analysis of time-averaged connectivity data (Chapter 1), global and mesoscopic dynamical measures (Chapter 2), and the clustering of specific functional networks states over time (Chapter 3). Indeed, unlike the intrinsic ignition methodology employed here, none of these approaches directly considered the contributions of local signals towards the integration/segregation balance (i.e. how regional activity dynamics help shape global brain integration).

The finding of globally increased ignition-driven integration (IDI) following the psilocybin infusion suggests that ignition events from individual brain areas are, on average, more likely to propagate to the rest of the network than during the pre-injection baseline, hence promoting global integration. Despite reaching significance at the whole-brain scale (i.e. by averaging the IDI across all 90 brain regions), the regional differences in IDI only survived the FDR correction for multiple comparisons for only two brain areas: the anterior cingulate gyrus and right inferior frontal gyrus. Nevertheless, the IDI was consistently higher (albeit non-significantly) post-psilocybin than in the pre-injection baseline for almost every brain area (Figure 5.3), which explains the presence of a significant difference when

averaging regional IDI scores to obtain a whole-brain measure. I suspect the small sample of subjects (n=9) may have contributed to this discrepancy between the significant global effect of psilocybin and small proportion of significant regional effects in the between-condition comparison. The enhanced broadcasting of local signals is in broad agreement with time-averaged functional connectivity analyses of psilocybin and LSD showing increases in global integration and a reduction of within-network integrity at the expense of enhanced cross-modular communication, and sheds light on the possible underlying mechanisms (See Introduction 1.3.2). Indeed, the tendency of individual brain areas to broadcast local signals more globally would lead to a blurring of the functional boundaries between brain modules and promote system-wide integration. At the phenomenological level, this observation is also consistent with the subjective reports of synesthesia and hyper-associative cognition in the psychedelic state.

The variability in the amount of propagation of local signals following ignition events (IDI-variability) also increased in the psilocybin condition relative to baseline, both globally and for 15 individual brain regions including the bilateral anterior cingulate gyrus, bilateral insula, and bilateral fusiform gyrus (Figures 5.3 and 5.4). The enhanced variability of the IDI may be interpreted as a measure of regional computational complexity whereby a given brain area becomes increasingly capable of flexibly broadcasting information both globally and locally over time. This could represent a regional substrate for the expansion of the dynamical repertoire of functional network states by serotonergic psychedelics, which has been reported via the analysis of dynamical functional connectivity states (Tagliazucchi, Carhart-Harris et al. 2014) and the connectome harmonic decomposition of brain activity (Atasoy, Roseman et al. 2017). Although somewhat speculative, I noted that regions showing significant bilateral increases in IDI-variability (anterior cingulate and insula) make up the "salience network" (Seeley, Menon et al. 2007). The salience network has been postulated to detect and evaluate the relevance of environmental stimuli (i.e. *what* needs to be dealt with in the environment), bias processing accordingly, and allow us to feel the consequences as affective states (Lebedev, Lövdén et al. 2015). Hence, the increased diversity of computation within the salience network regions found in this analysis may lead to the dissolution of embodied self and manifest psychologically as a sense of connection and boundlessness with the environment (coined "ego-dissolution") which is frequently reported in the psychedelic state (Lebedev, Lövdén et al. 2015, Letheby and Gerrans 2017).

In slow-wave sleep (N3), I found a strong and statistically significant reduction in both the mean integration elicited by driving events (IDI), as well as their IDI variability in every region under study (Figure 5.5). These results suggest that deep sleep drastically disrupts the propagation of local intrinsic perturbations globally, consistent with the previously discussed TMS/EEG experiments employing exogenous perturbations (Massimini, Ferrarelli et al. 2005, Casali, Gosseries et al. 2013). The present findings also agree with prior fMRI studies demonstrating an increase in network modularity (i.e. a measure of functional segregation) in slow-wave sleep relative to wakeful rest (Spoormaker, Schröter et al. 2010, Boly, Perlbarg et al. 2012, Tagliazucchi, Von Wegner et al. 2013). Notably, Boly and colleagues showed that the "functional clustering ratio" (defined by the ratio of between- and within-subsystems integration) was significantly increased in slow-wave sleep in several canonical resting-state networks (Boly, Perlbarg et al. 2012). Here I provide a possible *regional-level* explanation for this finding as local driving events become less likely to elicit global integration in N3 sleep than wakeful rest. Furthermore, the reduction in IDI-variability at every node suggests a generalized loss of local computational complexity in slow-wave sleep. That is, network nodes lose the ability to flexibly propagate information both locally and globally over time, instead settling into a more rigid dynamical regime tipped strongly in favor of local integration. Consistent with this idea, prior studies have shown a loss of temporal complexity of brain signals during sleep and anesthesia. The temporal complexity of local BOLD signals decreases during NREM sleep, as indicated by a significant shift of the Hurst exponent towards short-range temporal correlations relative to wakeful rest (Tagliazucchi, von Wegner et al. 2013); and Lempel-Ziv complexity (a measure of the number of distinct patterns present in the data) reveals a loss signal diversity in slow-wave sleep when applied to electrophysiological recordings (Schartner, Pigorini et al. 2017).

A limitation of the present analysis is the relatively small number of subjects included in the psilocybin fMRI dataset. This may notably have contributed to higher sample variance in the regional IDI scores and explain the failure of most regions to survive the multiple comparisons correction when comparing the pre vs post-psilocybin conditions, despite the presence of a significant global effect. I am nevertheless confident that the reported regional and global increases on the IDI and IDI variability post-psilocybin infusion are non-trivial, as a conservative statistical procedure was used for multiple comparison correction and, importantly, the placebo injection induced no significant change in IDI or

IDI variability in these same subjects, neither at the local or global levels (Figure 5.3, bottom panel). It should also be noted that while the current analysis employed a threshold crossing method for extracting ignition events, as performed in previous studies (Tagliazucchi, Carhart-Harris et al. 2014, Schartner, Carhart-Harris et al. 2017), alternative mathematical methods for extracting point processes also exist (Caballero Gaudes, Petridou et al. 2013). Another consideration is the width of the window size following ignition events used in this analysis. Here I reported the results of the analysis using a time window of 3*TR, but I have replicated these findings (i.e. significant between-condition differences) for both the psilocybin and sleep data by using time windows of width: 2*TR and 4*TR respectively; with the only exception that the post-psilocybin mean IDI no longer reaches statistical significance relative to baseline with the window of width 2*TR (although the IDI-variability results remain significant). Moreover, because the TR parameter itself was different in the sleep (TR = 2.2s) and psilocybin (TR = 3s) fMRI datasets. The corresponding time windows of integration are therefore of 9 seconds for the psilocybin study and 6.6 seconds for the sleep study. This would need to be accounted for if directly comparing the psilocybin and sleep measures; however I only considered within-groups statistical comparisons in the present study, as different study participants, scanning equipment and sample sizes were involved. Finally, the general methodological limitations inherent to the use of fMRI to study brain dynamics in these particular cohorts discussed earlier also apply to the results presented in this Chapter (see Section 3.4).

5.5 Chapter Summary

In summary, I have used a novel intrinsic ignition framework to study the local vs global broadcasting of information of individual brain regions in altered states of consciousness. The computation of intrinsic ignition relies on measuring the size of the integration cascades across the whole network which follow a regional driving-event in binarized fMRI time courses, using a windowed approach. I have found that slow-wave sleep and the psychedelic state have opposite effects on the capacity of driving events at local nodes to propagate to the rest of the network, as reflected by corresponding changes in the ignition-driven-integration (IDI) measure. Psilocybin increases, on average, the system-wide integration elicited by local driving events, as well as the computational complexity in several local nodes, estimated by the IDI-variability. Slow-wave sleep, on the other hand, strongly favors the local propagation of driving events and nodal dynamics become less metastable than in the awake state. These results may thus provide a regional substrate for

the changes in functional network modularity and neural signal complexity reported in prior neuroimaging investigations of slow-wave sleep and the psychedelic state.

Chapter 6: Conclusion

The integration/segregation balance is intrinsically linked to some of the most complex and fascinating phenomena of modern neuroscience; from the spontaneous emergence of resting-state networks to higher cognition and, as outlined in this Thesis, consciousness level and/or contents. The major aim of the research programme I have pursued during my time in Oxford was to provide novel insights about the principles of integration and segregation of information in the human brain from neuroimaging data. A strong focus was placed on the investigating the *dynamical* properties of whole-brain networks in altered states of consciousness, as it pertains to the integration/segregation balance (Chapters 3,4,5). Such questions had remained virtually unexplored and I rationaled that addressing them could contribute to a system-level understanding of the dynamical brain changes associated with markedly different consciousness levels and/or contents, and their links to established neuropharmacological/neurochemical mechanisms. I conclude this Thesis by recapitulating specifically how the present body of work has made significant original contributions to the field (Section 6.1). The implications of these findings are then discussed from broader theoretical and conceptual perspectives (Section 6.2).

6.1 Original Contributions

In Chapter 2, I studied the integration/segregation balance by extracting persistent homological scaffolds from resting-state fMRI data. At the time of publishing these results (Lord, Expert et al. 2016), only one other study had investigated homological holes in neuroimaging data (Petri, Expert et al. 2014). Since then, a small number of additional studies have been conducted in this area, including the localization topological cavities of different dimensions in the structural connectome (Sizemore, Giusti et al. 2018). The findings presented in Chapter 2 however remain, to our knowledge, the first and only analysis of the topological properties of homological scaffolds of human brain networks from a *node-level* perspective, as well as the first direct comparison of persistent homology data with standard graph theoretical measures. I found that topologically central nodes in the homological scaffolds were well positioned to support the global integration of information processing in the human brain, hence demonstrating that the study of functional connectivity networks from a non-dyadic perspective based on the homology of the data can provide useful insights into the brain's functional architecture.

In Chapters 3 and 4, I explored the dynamical properties of the integration/segregation balance in whole-brain networks in altered states of consciousness. Previous network-based analyses of sleep and psychedelics neuroimaging datasets had employed, almost exclusively, *time-averaged* functional connectivity measures to characterize the brain's functional architecture in these states. As a whole, prior studies in this area had provided convincing evidence for the enhancement of cross-modular communication by serotonergic psychedelics (see Introduction 1.3.2) and, conversely, increases in the modularity of FC networks during deep sleep (see Introduction 1.4.2). However, static network representations of brain activity involve significant methodological and conceptual limitations, especially since the typical FC matrix calculation ignores the importance of time. I therefore expanded upon these findings and analyzed the spatiotemporal properties of whole-brain networks in these altered states of consciousness from a dynamical perspective. To do so, I methodologically leveraged on the instantaneous FC matrix derivation from fMRI data, and the dynamical evolution its properties.

In Chapter 3, I considered "global" properties of whole-brain networks; in the sense that I was not (yet) interested in clustering the dynamic FC matrices into specific subsystems. I quantified the extent to which a network of 90 brain areas (comprising both cortical and subcortical structures) synchronized and/or de-synchronized over time. I revealed, for the first time in a whole-brain network, that the psychedelic "trip" induced by a psilocybin administration increased global synchrony and metastability relative to baseline, whilst slow-wave sleep was characterized by significant reductions on these same measures compared to wakeful rest. I also applied the "chimeraness index" to these same data to quantify the co-occurrence of synchronous and asynchronous behavior across network modules. This was the first application of the chimeraness index on empirical neuroimaging data as it had only been previously implemented to study the dynamics of synthetic network models (Shanahan 2010). I showed that the network communities' internal synchronies were on average more homogenous *in space* at any given time point in the psychedelic state compared to baseline, whilst they were more variable during deep sleep.

Chapter 4 built upon these dynamical functional connectivity findings from a systems-level perspective, as I used a novel analytical approach based on the unsupervised clustering of the leading eigenvectors of FC matrices to characterize the temporal expression patterns of different FC states (i.e. anatomically localized networks) in the psychedelic state. The findings from this Chapter represented the first experimental evidence that the brain's

dynamical landscape (defined here as the structured exploration of FC states over time) was altered by the classical psychedelic drug psilocybin. Notably, the fractional occupancy of a FC state overlapping with the fronto-parietal control system was strongly reduced, suggesting that this particular functional network becomes destabilized under psilocybin. Conversely, transitions toward a globally integrated FC state were enhanced, suggesting that the drug may induce an alternative type of functional integration at the expense of locally segregated activity in specialized networks.

Taken together the results Chapter 3 and 4 not only align with, but help explain from a dynamical viewpoint the results of previous time-averaged functional connectivity studies in the psychedelic state and slow-wave sleep, especially as it pertains to changes in network modularity. The new lines of evidence presented in this Thesis indicate that the brain is, at any given time, more likely to be found in a highly synchronized state (both in terms of inter-areal and inter-modular connectivity) in the psychedelic state than at baseline, and that the opposite holds true during slow-wave sleep. The findings from Chapter 4 further suggest that, at least in the case of psilocybin, this may in turn be due to changes in the brain's attractor landscape in which: *i)* transitions towards a globally coherent FC state are favored; and *ii)* the dynamics are less likely to visit a subset of functionally specialized networks, including networks associated with cognitive control. It is noteworthy that, since global metastability is also significantly increased in the psychedelic alongside the observed increase in global synchrony, the system by no means permanently settles into globally coherent state under the drug, and still spends most of the time exploring the rest of its dynamical repertoire, albeit following different trajectories than it would at baseline.

Finally, in Chapter 5 I used a novel framework of "intrinsic ignition" to characterize the tendency of brain areas to dynamically broadcast regional activity signals either locally or globally in both slow-wave sleep and in the psychedelic state. Prior neuroimaging analyses of local activity signals during slow-wave sleep and psychedelic experiences had notably used measures of signal variability and complexity (i.e. Lempel-Ziv complexity, Hurst exponent) to characterize brain dynamics, and generally found these metrics to be increased following the administration of classical psychedelics, and decreased in behavioral states characterized by reductions in vigilance level including deep sleep and general anesthesia (see Introduction 1.3.2 & 1.4.2). However these measures are, by definition, strictly local and do not account for the possible consequences of regional activity dynamics on the rest of the network. By contrast the intrinsic ignition framework characterizes the

dynamical integration/segregation balance by describing how activity in a local region shapes global activity, and the way in which the broadness of communication is elicited and distributed over time. Psilocybin increased, on average, the system-wide integration elicited by local driving events, as well as the temporal variability in the elicited integration in several local nodes. Slow-wave sleep, on the other hand, strongly favored the local propagation of driving events and nodal dynamics became less metastable than in the awake state. These results were broadly consistent with those presented in Chapters 3 and 4, and thus provided a regional substrate that might help explain the changes in the integration/segregation balance and metastability observable both at the whole-brain scale and at the system-level.

6.2 Perspectives

The novel experimental results presented in this Thesis are consistent with an understanding of brain function as a dynamical system which transitions between metastable activity states (i.e. functional network configurations) over time (Figure 6.1). Our findings notably indicate that the brain's dynamical landscape can be *reversibly* modulated by the known neurochemical changes underlying the psychedelic state and slow-wave sleep. They further suggests that a *modified* dynamical landscape (i.e. relative to wakeful rest) in which brain state trajectories become biased towards either functional network integration or segregation can drastically alter one's subjective experience (i.e. sleeping greatly differs, from a first person perspective, from the experience of "everyday consciousness", as does a psychedelic trip).

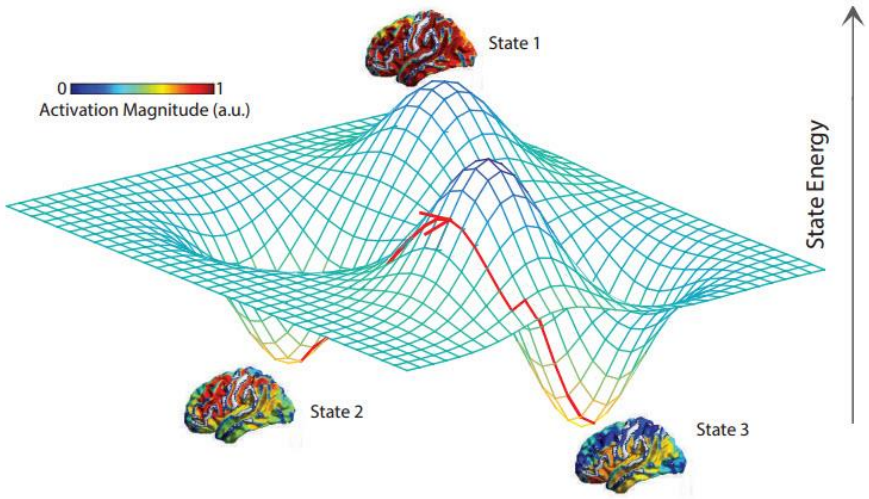


Figure 6.1. Conceptual schematic of the brain's dynamical landscape. *Brain states are more or less likely to be visited by the dynamics (red trace) over time depending on their relative energy / stability. Different possible operational definitions of a "brain state" and of their energies are described below. These may notably be based on: regional activation values, dynamic functional connectivity, or the spatial power spectrum at any given time point. Adapted from Gu, Cieslak et al. 2018.*

A fascinating consideration is that such drastic changes in the brain's dynamical landscape (and corresponding behavioral outputs) over relatively short time intervals can be sustained by the same structural connectome. Indeed, the brain activity changes measured in both the sleep and psilocybin fMRI datasets occur on far too rapid timescales to allow for any macroscopic rearrangement of the anatomical connectome detectable with diffusion tensor imaging. The results from this Thesis therefore reinforce the view that, whilst the anatomical connectome makes a significant contribution towards shaping the brain's dynamical landscape and associated behavioral outputs, it is not its sole determinant.

Another interesting discussion point in the context the exploration of the brain's dynamical landscape concerns the operational definition of a "brain state". A simple definition used by some authors is to consider a brain state as a vector of regional activation values (Gu, Cieslak et al. 2018); however this definition only implicitly considers the brain's network connectivity, which may be limiting. By contrast, in Chapter 4, I have used a definition of brain state as an instantaneous pattern of synchronous activity between specific brain regions, which re-occurs over time, thus explicitly accounting for the brain's functional network connectivity. Closely related definitions had been used by other authors (Allen, Damaraju et al. 2014, Hansen, Battaglia et al. 2015, Shine, Koyejo et al. 2016, Cabral, Vidaurre et al. 2017) albeit based on slightly different variations of the clustering of FC matrices and in the computation of the FC matrix itself. A third possibility is to define a brain state as the relative contributions of a set of distinct spatial frequencies (i.e.

connectome Laplacian eigenvectors) towards explaining brain activity (Atasoy, Donnelly et al. 2016, Damestani 2017), which can be thought of as the "spatial power spectrum" at a given time point.

In order to map out the brain's dynamical landscape, the operational definition of a brain state must be accompanied by a measure of its stability, since the respective energies/stabilities of brain states will shape how brain activity unfolds over time (i.e. the dynamical trajectories). Such definitions will of course depend on how brain states are defined in the first place. For example, the energy of a brain state defined as vector of regional activation values could simply be considered as the sum of these activations across the brain. More complex definitions are however needed when considering definitions of brain states based on either dynamical functional network connectivity or spatial power spectra. From a functional connectivity perspective, it could be argued that an energetic cost is attributed to momentarily synchronizing brain activity within a specific system, rather than remaining in an undifferentiated state where the entire system is either fully synchronized (but at a lower intensity) or desynchronized. Supporting this view, it is well known that cognitive task demands are characterized by joint regional increases in cerebral metabolism *and* increased functional connectivity in specific functional networks. The relative stability of a brain state (even in the absence of task demands) may therefore be defined as the transient difference between the metabolic demands of those regions contained within the subsystem achieving differentiation (i.e. becoming internally synchronized), and the mean energy of the undifferentiated 'ground' state. According to the same reasoning, a brain state defined by high spatial frequencies, which reflect anatomical segregation of the activity, would be less stable than those characterized by low frequency connectome eigenvectors. The spatial power spectrum of a given brain state could therefore serve as a basis to estimate its relative stability. These open questions represent important future steps towards an understanding of global brain dynamics, and associated changes in consciousness levels and/or contents.

Whole-brain computational models (see Introduction 1.1.3) might play an important role towards mapping brain dynamical landscapes, especially should they eventually capture with accuracy the rich repertoire of FC states observed in empirical data (Hansen, Battaglia et al. 2015, Lord, Stevner et al. 2017). Whole-brain models can indeed simulate very long timecourses of neural activity *in silico* which cannot realistically be collected in traditional neuroimaging experiments. The data-rich, multimodal datasets provided by whole-brain

models may thereby facilitate the characterization of brain states and of the mechanisms underlying inter-state transitions. Furthermore, as recently demonstrated, whole-brain modelling informed by additional biological parameters (i.e. receptor density mapping) may help explain the nonlinear effects of neuromodulators on brain dynamics (Deco, Cruzat et al. 2018), and corresponding changes in the brain's dynamical landscape.

A final point concerns the potential clinical relevance of a dynamical systems perspective on brain function. Whilst neuropsychiatric syndromes are most often characterized on the basis of stable brain differences (i.e. grey or white matter changes), this contrasts with the reality that a patient's symptoms can substantially vary over time. For example, individuals with mood disorders are not always 'equally' depressed or anxious; and schizophrenia patients do not permanently experience psychotic episodes. A perspective on brain function based on a landscape of attractors and associated dynamical trajectories is indeed compatible with such behavioral observations. A patient's energy landscape may be altered in ways that promote the dynamical exploration of brain states underlying their symptoms (i.e. low mood, hallucinations) whilst still preserving several aspects of normal brain function. Whether state transitions leading to clinical manifestations result from the emergence of 'new' pathological brain states in the patients, and/or substantial changes in the probabilities of occurrence of states theoretically accessible to a healthy brain remains an open question. In either scenario, patients' energy landscape would be expected to differ from those of matched controls. Identifying the contributions of genetic (Meyer-Lindenberg and Weinberger 2006), environmental (Kendler, Prescott et al. 2003), stress and neuroendocrine factors (Cerqueira, Mailliet et al. 2007, Lucassen, Pruessner et al. 2014) towards the progressive shaping of a pathological dynamical repertoire represents an exciting avenue of research. Such investigations could indeed provide an exciting bridge between the computational and clinical neurosciences.

References

Alexander-Bloch, A. F., N. Gogtay, D. Meunier, R. Birn, L. Clasen, F. Lalonde, R. Lenroot, J. Giedd and E. T. Bullmore (2010). "Disrupted modularity and local connectivity of brain functional networks in childhood-onset schizophrenia." Frontiers in systems neuroscience **4**: 147.

Allen, E. A., E. Damaraju, S. M. Plis, E. B. Erhardt, T. Eichele and V. D. Calhoun (2014). "Tracking Whole-Brain Connectivity Dynamics in the Resting State." Cerebral Cortex **24**(3): 663-676.

Andrade, R. (2011). "Serotonergic regulation of neuronal excitability in the prefrontal cortex." Neuropharmacology **61**(3): 382-386.

Andrillon, T., A. T. Poulsen, L. K. Hansen, D. Leger and S. Kouider (2016). "Neural Markers of Responsiveness to the Environment in Human Sleep." J Neurosci **36**(24): 6583-6596.

Arslan, S., S. I. Ktena, A. Makropoulos, E. C. Robinson, D. Rueckert and S. Parisot (2018). "Human brain mapping: A systematic comparison of parcellation methods for the human cerebral cortex." Neuroimage **170**: 5-30.

Aserinsky, E. and N. Kleitman (1953). "Regularly occurring periods of eye motility, and concomitant phenomena, during sleep." Science **118**(3062): 273-274.

Atasoy, S., G. Deco, M. L. Kringelbach and J. Pearson (2018). "Harmonic brain modes: a unifying framework for linking space and time in brain dynamics." The Neuroscientist **24**(3): 277-293.

Atasoy, S., I. Donnelly and J. Pearson (2016). "Human brain networks function in connectome-specific harmonic waves." Nature communications **7**: 10340.

Atasoy, S., L. Roseman, M. Kaelen, M. L. Kringelbach, G. Deco and R. L. Carhart-Harris (2017). "Connectome-harmonic decomposition of human brain activity reveals dynamical repertoire re-organization under LSD." Scientific reports **7**(1): 17661.

Baars, B. J. (2005). "Global workspace theory of consciousness: toward a cognitive neuroscience of human experience." Progress in brain research **150**: 45-53.

Bak, P. (2013). How nature works: the science of self-organized criticality, Springer Science & Business Media.

Baker, A. P., M. J. Brookes, I. A. Rezek, S. M. Smith, T. Behrens, P. J. P. Smith and M. Woolrich (2014). "Fast transient networks in spontaneous human brain activity." eLife **3**(e0187).

Ball, G., P. R. Stokes, R. A. Rhodes, S. K. Bose, I. Rezek, A.-M. Wink, L.-D. Lord, M. A. Mehta, P. M. Grasby and F. E. Turkheimer (2011). "Executive functions and prefrontal cortex: a matter of persistence?" Frontiers in systems neuroscience **5**: 3.

Bassett, D. S. and E. Bullmore (2006). "Small-world brain networks." The neuroscientist **12**(6): 512-523.

Beckmann, C. F. and S. M. Smith (2004). "Probabilistic independent component analysis for functional magnetic resonance imaging." IEEE transactions on medical imaging **23**(2): 137-152.

Beggs, J. M. (2008). "The criticality hypothesis: how local cortical networks might optimize information processing." Philosophical Transactions of the Royal Society of London A: Mathematical, Physical and Engineering Sciences **366**(1864): 329-343.

Beggs, J. M. and D. Plenz (2003). "Neuronal avalanches in neocortical circuits." Journal of neuroscience **23**(35): 11167-11177.

Beliveau, V., M. Ganz, L. Feng, B. Ozenne, L. Højgaard, P. M. Fisher, C. Svarer, D. N. Greve and G. M. Knudsen (2017). "A high-resolution in vivo atlas of the human brain's serotonin system." Journal of Neuroscience **37**(1): 120-128.

Benjamini, Y. and Y. Hochberg (1995). "Controlling the false discovery rate: a practical and powerful approach to multiple testing." Journal of the royal statistical society. Series B (Methodological): 289-300.

Berry, R. B., R. Brooks, C. E. Gamaldo, S. M. Harding, C. Marcus and B. Vaughn (2012). "The AASM manual for the scoring of sleep and associated events." Rules, Terminology and Technical Specifications, Darien, Illinois, American Academy of Sleep Medicine.

Bertolero, M. A., B. T. Yeo and M. D'Esposito (2015). "The modular and integrative functional architecture of the human brain." Proceedings of the National Academy of Sciences **112**(49): E6798-E6807.

Betzel, R. F., M. Fukushima, Y. He, X.-N. Zuo and O. Sporns (2016). "Dynamic fluctuations coincide with periods of high and low modularity in resting-state functional brain networks." NeuroImage **127**: 287-297.
Blondel, V. D., J.-L. Guillaume, R. Lambiotte and E. Lefebvre (2008). "Fast unfolding of communities in large networks." Journal of statistical mechanics: theory and experiment **2008**(10): P10008.
Boly, M., V. Perlbarg, G. Marrelec, M. Schabus, S. Laureys, J. Doyon, M. Pélégrini-Issac, P. Maquet and H. Benali (2012). "Hierarchical clustering of brain activity during human nonrapid eye movement sleep." Proceedings of the National Academy of Sciences **109**(15): 5856-5861.
Braun, A. R., T. Balkin, N. Wesenten, R. Carson, M. Varga, P. Baldwin, S. Selbie, G. Belenky and P. Herscovitch (1997). "Regional cerebral blood flow throughout the sleep-wake cycle. An H2 (15) O PET study." Brain: a journal of neurology **120**(7): 1173-1197.
Bullmore, E. and O. Sporns (2009). "Complex brain networks: graph theoretical analysis of structural and functional systems." Nature Reviews Neuroscience **10**(3): 186.
Bullmore, E. and O. Sporns (2012). "The economy of brain network organization." Nature Reviews Neuroscience **13**(5): 336.
Caballero Gaudes, C., N. Petridou, S. T. Francis, I. L. Dryden and P. A. Gowland (2013). "Paradigm free mapping with sparse regression automatically detects single-trial functional magnetic resonance imaging blood oxygenation level dependent responses." Human brain mapping **34**(3): 501-518.
Cabral, J., E. Hugues, M. L. Kringelbach and G. Deco (2012). "Modeling the outcome of structural disconnection on resting-state functional connectivity." Neuroimage **62**(3): 1342-1353.
Cabral, J., E. Hugues, O. Sporns and G. Deco (2011). "Role of local network oscillations in resting-state functional connectivity." Neuroimage **57**(1): 130-139.
Cabral, J., M. L. Kringelbach and G. Deco (2014). "Exploring the network dynamics underlying brain activity during rest." Progress in neurobiology **114**: 102-131.
Cabral, J., D. Vidaurre, P. Marques, R. Magalhães, P. S. Moreira, J. M. Soares, G. Deco, N. Sousa and M. L. Kringelbach (2017). "Cognitive performance in healthy older adults relates to spontaneous switching between states of functional connectivity during rest." Scientific Reports **7**(1): 5135.
Calhoun, V. D., R. Miller, G. Pearlson and T. Adalı (2014). "The chronnectome: time-varying connectivity networks as the next frontier in fMRI data discovery." Neuron **84**(2): 262-274.
Carhart-Harris, R. L. (2018). "The entropic brain-revisited." Neuropharmacology.
Carhart-Harris, R. L., M. Bolstridge, J. Rucker, C. M. Day, D. Erritzoe, M. Kaelen, M. Bloomfield, J. A. Rickard, B. Forbes and A. Feilding (2016). "Psilocybin with psychological support for treatment-resistant depression: an open-label feasibility study." The Lancet Psychiatry **3**(7): 619-627.
Carhart-Harris, R. L., D. Erritzoe, T. Williams, J. M. Stone, L. J. Reed, A. Colasanti, R. J. Tyacke, R. Leech, A. L. Malizia and K. Murphy (2012). "Neural correlates of the psychedelic state as determined by fMRI studies with psilocybin." Proceedings of the National Academy of Sciences **109**(6): 2138-2143.
Carhart-Harris, R. L., R. Leech, P. J. Hellyer, M. Shanahan, A. Feilding, E. Tagliazucchi, D. R. Chialvo and D. Nutt (2014). "The entropic brain: a theory of conscious states informed by neuroimaging research with psychedelic drugs." Frontiers in human neuroscience **8**(20).
Carskadon, M. A. and W. C. Dement (2005). "Normal human sleep: an overview." Principles and practice of sleep medicine **4**: 13-23.
Casali, A. G., O. Gosseries, M. Rosanova, M. Boly, S. Sarasso, K. R. Casali, S. Casarotto, M.-A. Bruno, S. Laureys and G. Tononi (2013). "A theoretically based index of consciousness independent of sensory processing and behavior." Science translational medicine **5**(198).
Cavanna, F., M. G. Vilas, M. Palmucci and E. Tagliazucchi (2017). "Dynamic functional connectivity and brain metastability during altered states of consciousness." NeuroImage.
Cerqueira, J. J., F. Mailliet, O. F. Almeida, T. M. Jay and N. Sousa (2007). "The prefrontal cortex as a key target of the maladaptive response to stress." Journal of Neuroscience **27**(11): 2781-2787.
Chialvo, D. R. (2010). "Emergent complex neural dynamics." Nature physics **6**(10): 744.
Cleeremans, A. E. (2003). The unity of consciousness: Binding, integration, and dissociation, Oxford University Press.

Clune, J., J.-B. Mouret and H. Lipson (2013). "The evolutionary origins of modularity." Proc. R. Soc. B **280**(1755).
Cohen-Steiner, D., H. Edelsbrunner and J. Harer (2005). Stability of persistence diagrams. Proceedings of the twenty-first annual symposium on Computational geometry, ACM.
Cole, M. W. and W. Schneider (2007). "The cognitive control network: integrated cortical regions with dissociable functions." Neuroimage **37**(1): 343-360.
Crick, F. and C. Koch (1990). Towards a neurobiological theory of consciousness. Seminars in the Neurosciences, Saunders Scientific Publications.
Damestani, N. (2017). Spectral Analysis of the fMRI Signal: Exploring the Dynamics, Stability and Organisation of the Spatial Scales of Brain Function during Tasks and Rest. MSc Neuroimaging Master's Thesis, King's College London.
Deco, G., J. Cruzat, J. Cabral, G. M. Knudsen, R. L. Carhart-Harris, P. C. Whybrow, N. K. Logothetis and M. L. Kringelbach (2018). "Whole-brain multimodal neuroimaging model using serotonin receptor maps explains non-linear functional effects of LSD." Current biology **28**(19): 3065-3074. e3066.
Deco, G., V. K. Jirsa and A. R. McIntosh (2013). "Resting brains never rest: computational insights into potential cognitive architectures." Trends in neurosciences **36**(5): 268-274.
Deco, G. and M. Kringelbach (2016). "Metastability and Coherence: Extending the Communication through Coherence Hypothesis Using a Whole-Brain Computational Perspective." Trends Neurosci **39**(6): 432.
Deco, G. and M. L. Kringelbach (2014). "Great expectations: using whole-brain computational connectomics for understanding neuropsychiatric disorders." Neuron **84**(5): 892-905.
Deco, G. and M. L. Kringelbach (2017). "Hierarchy of information processing in the brain: a novel 'intrinsic ignition'framework." Neuron **94**(5): 961-968.
Deco, G., E. Tagliazucchi, H. Laufs, A. Sanjuán and M. L. Kringelbach (2017). "Novel Intrinsic Ignition Method Measuring Local-Global Integration Characterises Wakefulness and Deep Sleep." Eneuro: ENEURO. 0106-0117.2017.
Deco, G., G. Tononi, M. Boly and M. L. Kringelbach (2015). "Rethinking segregation and integration: contributions of whole-brain modelling." Nature Reviews Neuroscience **16**(7): 430-439.
Dey, T. K., A. N. Hirani and B. Krishnamoorthy (2011). "Optimal homologous cycles, total unimodularity, and linear programming." SIAM Journal on Computing **40**(4): 1026-1044.
Dosenbach, N. U., D. A. Fair, A. L. Cohen, B. L. Schlaggar and S. E. Petersen (2008). "A dual-networks architecture of top-down control." Trends in cognitive sciences **12**(3): 99-105.
Expert, P., R. Lambiotte, D. R. Chialvo, K. Christensen, H. J. Jensen, D. J. Sharp and F. Turkheimer (2011). "Self-similar correlation function in brain resting-state functional magnetic resonance imaging." Journal of The Royal Society Interface **8**(57): 472-479.
Fornito, A., A. Zalesky and M. Breakspear (2015). "The connectomics of brain disorders." Nature Reviews Neuroscience **16**(3): 159.
Friston, K. J. (1994). "Functional and effective connectivity in neuroimaging: a synthesis." Human brain mapping **2**(1-2): 56-78.
Garrison, K. A., D. Scheinost, E. S. Finn, X. Shen and R. T. Constable (2015). "The (in) stability of functional brain network measures across thresholds." Neuroimage **118**: 651-661.
Glover, G. H., T. Q. Li and D. Ress (2000). "Image-based method for retrospective correction of physiological motion effects in fMRI: RETROICOR." Magnetic resonance in medicine **44**(1): 162-167.
Goodman, L. S. (1996). Goodman and Gilman's the pharmacological basis of therapeutics, McGraw-Hill New York.
Granovetter, M. S. (1977). The strength of weak ties. Social networks, Elsevier**:** 347-367.
Gu, S., M. Cieslak, B. Baird, S. F. Muldoon, S. T. Grafton, F. Pasqualetti and D. S. Bassett (2018). "The energy landscape of neurophysiological activity implicit in brain network structure." Scientific reports **8**(1): 2507.
Haider, B., A. Duque, A. R. Hasenstaub and D. A. McCormick (2006). "Neocortical network activity in vivo is generated through a dynamic balance of excitation and inhibition." Journal of Neuroscience **26**(17): 4535-4545.

Hansen, E. C., D. Battaglia, A. Spiegler, G. Deco and V. K. Jirsa (2015). "Functional connectivity dynamics: modeling the switching behavior of the resting state." Neuroimage **105**: 525-535.
Hansen, E. C., D. Battaglia, A. Spiegler, G. Deco and V. K. Jirsa (2015). "Functional connectivity dynamics: modeling the switching behavior of the resting state." Neuroimage **105**: 525-535.
He, B. J. and M. E. Raichle (2009). "The fMRI signal, slow cortical potential and consciousness." Trends in cognitive sciences **13**(7): 302-309.
Hindriks, R., M. H. Adhikari, Y. Murayama, M. Ganzetti, D. Mantini, N. K. Logothetis and G. Deco (2015). "Can sliding-window correlations reveal dynamic functional connectivity in resting-state fMRI?" Neuroimage **127**: 242-256.
Honey, C., O. Sporns, L. Cammoun, X. Gigandet, J.-P. Thiran, R. Meuli and P. Hagmann (2009). "Predicting human resting-state functional connectivity from structural connectivity." Proceedings of the National Academy of Sciences **106**(6): 2035-2040.
Jenkinson, M., P. Bannister, M. Brady and S. Smith (2002). "Improved optimization for the robust and accurate linear registration and motion correction of brain images." Neuroimage **17**(2): 825-841.
Jobst, B. M., R. Hindriks, H. Laufs, E. Tagliazucchi, G. Hahn, A. Ponce-Alvarez, A. B. Stevner, M. L. Kringelbach and G. Deco (2017). "Increased stability and breakdown of brain effective connectivity during slow-wave sleep: mechanistic insights from whole-brain computational modelling." Scientific reports **7**(1): 4634.
Johnson, M. W., R. A. Sewell and R. R. Griffiths (2012). "Psilocybin dose-dependently causes delayed, transient headaches in healthy volunteers." Drug and alcohol dependence **123**(1-3): 132-140.
Kelso, J. S. (2012). "Multistability and metastability: understanding dynamic coordination in the brain." Phil. Trans. R. Soc. B **367**(1591): 906-918.
Kendler, K. S., C. A. Prescott, J. Myers and M. C. Neale (2003). "The structure of genetic and environmental risk factors for common psychiatric and substance use disorders in men and women." Archives of general psychiatry **60**(9): 929-937.
Kometer, M., A. Schmidt, R. Bachmann, E. Studerus, E. Seifritz and F. X. Vollenweider (2012). "Psilocybin biases facial recognition, goal-directed behavior, and mood state toward positive relative to negative emotions through different serotonergic subreceptors." Biological psychiatry **72**(11): 898-906.
Kometer, M., A. Schmidt, L. Jäncke and F. X. Vollenweider (2013). "Activation of serotonin 2A receptors underlies the psilocybin-induced effects on α oscillations, N170 visual-evoked potentials, and visual hallucinations." Journal of Neuroscience **33**(25): 10544-10551.
Kuramoto, Y. (1975). Self-entrainment of a population of coupled non-linear oscillators. International symposium on mathematical problems in theoretical physics, Springer.
Larson-Prior, L. J., J. M. Zempel, T. S. Nolan, F. W. Prior, A. Z. Snyder and M. E. Raichle (2009). "Cortical network functional connectivity in the descent to sleep." Proceedings of the National Academy of Sciences **106**(11): 4489-4494.
Lebedev, A. V., M. Lövdén, G. Rosenthal, A. Feilding, D. J. Nutt and R. L. Carhart-Harris (2015). "Finding the self by losing the self: Neural correlates of ego-dissolution under psilocybin." Human brain mapping **36**(8): 3137-3153.
Letheby, C. and P. Gerrans (2017). "Self unbound: ego dissolution in psychedelic experience." Neuroscience of Consciousness **2017**(1): nix016.
Logothetis, N. K., J. Pauls, M. Augath, T. Trinath and A. Oeltermann (2001). "Neurophysiological investigation of the basis of the fMRI signal." Nature **412**(6843): 150.
Logothetis, N. K. and B. A. Wandell (2004). "Interpreting the BOLD signal." Annu. Rev. Physiol. **66**: 735-769.
Lord, L.-D., P. Allen, P. Expert, O. Howes, M. Broome, R. Lambiotte, P. Fusar-Poli, I. Valli, P. McGuire and F. E. Turkheimer (2012). "Functional brain networks before the onset of psychosis: a prospective fMRI study with graph theoretical analysis." NeuroImage: Clinical **1**(1): 91-98.
Lord, L.-D., P. Allen, P. Expert, O. Howes, R. Lambiotte, P. McGuire, S. K. Bose, S. Hyde and F. E. Turkheimer (2011). "Characterization of the anterior cingulate's role in the at-risk mental state using graph theory." Neuroimage **56**(3): 1531-1539.

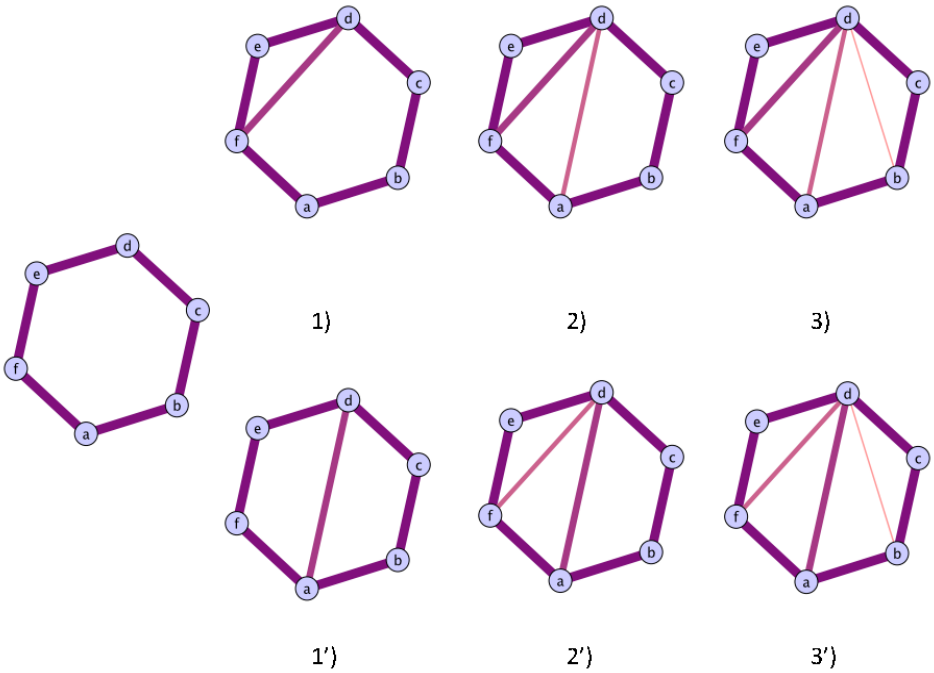
Lord, L.-D., P. Expert, H. M. Fernandes, G. Petri, T. J. Van Hartevelt, F. Vaccarino, G. Deco, F. Turkheimer and M. L. Kringelbach (2016). "Insights into brain architectures from the homological scaffolds of functional connectivity networks." Frontiers in systems neuroscience **10**: 85.
Lord, L. D., A. B. Stevner, G. Deco and M. L. Kringelbach (2017). "Understanding principles of integration and segregation using whole-brain computational connectomics: implications for neuropsychiatric disorders." Philos Trans A Math Phys Eng Sci **375**(2096).
Lucassen, P. J., J. Pruessner, N. Sousa, O. F. Almeida, A. M. Van Dam, G. Rajkowska, D. F. Swaab and B. Czéh (2014). "Neuropathology of stress." Acta neuropathologica **127**(1): 109-135.
Lynall, M.-E., D. S. Bassett, R. Kerwin, P. J. McKenna, M. Kitzbichler, U. Muller and E. Bullmore (2010). "Functional connectivity and brain networks in schizophrenia." Journal of Neuroscience **30**(28): 9477-9487.
Maquet, P., C. Degueldre, G. Delfiore, J. Aerts, J.-M. Péters, A. Luxen and G. Franck (1997). "Functional neuroanatomy of human slow wave sleep." Journal of Neuroscience **17**(8): 2807-2812.
Markov, N. T., M. Ercsey-Ravasz, D. C. Van Essen, K. Knoblauch, Z. Toroczkai and H. Kennedy (2013). "Cortical high-density counterstream architectures." Science **342**(6158): 1238406.
Massimini, M., F. Ferrarelli, R. Huber, S. K. Esser, H. Singh and G. Tononi (2005). "Breakdown of cortical effective connectivity during sleep." Science **309**(5744): 2228-2232.
Meyer-Lindenberg, A. and D. R. Weinberger (2006). "Intermediate phenotypes and genetic mechanisms of psychiatric disorders." Nature Reviews Neuroscience **7**(10): 818.
Mhuircheartaigh, R. N., C. Warnaby, R. Rogers, S. Jbabdi and I. Tracey (2013). "Slow-wave activity saturation and thalamocortical isolation during propofol anesthesia in humans." Science Translational Medicine **5**(208): 208ra148-208ra148.
Monti, J., S. R. Pandi-Perumal and C. M. Sinton (2008). Neurochemistry of sleep and wakefulness, Cambridge University Press.
Munkres, J. R. (1984). Elements of Algebraic Topology, Addinson, Wesley Publishing Company, Inc.
Murphy, K., A. D. Harris and R. G. Wise (2011). "Robustly measuring vascular reactivity differences with breath-hold: normalising stimulus-evoked and resting state BOLD fMRI data." Neuroimage **54**(1): 369-379.
Muthukumaraswamy, S. D., R. L. Carhart-Harris, R. J. Moran, M. J. Brookes, T. M. Williams, D. Errtizoe, B. Sessa, A. Papadopoulos, M. Bolstridge and K. D. Singh (2013). "Broadband cortical desynchronization underlies the human psychedelic state." Journal of Neuroscience **33**(38): 15171-15183.
Newman, M. E. (2000). "Models of the small world." Journal of Statistical Physics **101**(3-4): 819-841.
Newman, M. E. (2006). "Modularity and community structure in networks." Proceedings of the national academy of sciences **103**(23): 8577-8582.
Nichols, D. E. (2016). "Psychedelics." Pharmacological reviews **68**(2): 264-355.
Nir, Y., M. Massimini, M. Boly and G. Tononi (2013). Sleep and consciousness. Neuroimaging of consciousness, Springer**:** 133-182.
Okun, M. and I. Lampl (2008). "Instantaneous correlation of excitation and inhibition during ongoing and sensory-evoked activities." Nature neuroscience **11**(5): 535.
Ott, J. (1976). Hallucinogenic plants of North America, Wingbow Press.
Owen, A. M., M. R. Coleman, M. Boly, M. H. Davis, S. Laureys and J. D. Pickard (2006). "Detecting awareness in the vegetative state." science **313**(5792): 1402-1402.
Pace-Schott, E. F. and J. A. Hobson (2002). "The neurobiology of sleep: genetics, cellular physiology and subcortical networks." Nature Reviews Neuroscience **3**(8): 591.
Pandit, A. S., P. Expert, R. Lambiotte, V. Bonnelle, R. Leech, F. E. Turkheimer and D. J. Sharp (2013). "Traumatic brain injury impairs small-world topology." Neurology **80**(20): 1826-1833.
Passie, T., J. Seifert, U. Schneider and H. M. Emrich (2002). "The pharmacology of psilocybin." Addiction biology **7**(4): 357-364.
Petri, G., P. Expert, F. Turkheimer, R. Carhart-Harris, D. Nutt, P. J. Hellyer and F. Vaccarino (2014). "Homological scaffolds of brain functional networks." Journal of The Royal Society Interface **11**(101): 20140873.

Petri, G., M. Scolamiero, I. Donato and F. Vaccarino (2013). "Topological strata of weighted complex networks." PloS one **8**(6): e66506.
Power, J. D., A. L. Cohen, S. M. Nelson, G. S. Wig, K. A. Barnes, J. A. Church, A. C. Vogel, T. O. Laumann, F. M. Miezin and B. L. Schlaggar (2011). "Functional network organization of the human brain." Neuron **72**(4): 665-678.
Preti, M. G., T. A. Bolton and D. Van De Ville (2017). "The dynamic functional connectome: State-of-the-art and perspectives." Neuroimage **160**: 41-54.
Rechtschaffen, A. (1968). "A manual for standardized terminology, techniques and scoring system for sleep stages in human subjects." Brain information service.
Reuter, U., A. Chiarugi, H. Bolay and M. Moskowitz (2003). "Nuclear factor-kappaB as a molecular target for migraine therapy." Headache: The Journal of Head and Face Pain **43**(4): 426-427.
Roseman, L., R. Leech, A. Feilding, D. J. Nutt and R. L. Carhart-Harris (2014). "The effects of psilocybin and MDMA on between-network resting state functional connectivity in healthy volunteers." Frontiers in human neuroscience **8**: 204.
Rubinov, M. and O. Sporns (2010). "Complex network measures of brain connectivity: uses and interpretations." Neuroimage **52**(3): 1059-1069.
Rucker, J. J., J. Iliff and D. J. Nutt (2018). "Psychiatry & the psychedelic drugs. Past, present & future." Neuropharmacology **142**: 200-218.
Saper, C. B., P. M. Fuller, N. P. Pedersen, J. Lu and T. E. Scammell (2010). "Sleep state switching." Neuron **68**(6): 1023-1042.
Schartner, M. M., R. L. Carhart-Harris, A. B. Barrett, A. K. Seth and S. D. Muthukumaraswamy (2017). "Increased spontaneous MEG signal diversity for psychoactive doses of ketamine, LSD and psilocybin." Scientific reports **7**: 46421.
Schartner, M. M., A. Pigorini, S. A. Gibbs, G. Arnulfo, S. Sarasso, L. Barnett, L. Nobili, M. Massimini, A. K. Seth and A. B. Barrett (2017). "Global and local complexity of intracranial EEG decreases during NREM sleep." Neuroscience of Consciousness **3**(1).
Seeley, W. W., V. Menon, A. F. Schatzberg, J. Keller, G. H. Glover, H. Kenna, A. L. Reiss and M. D. Greicius (2007). "Dissociable intrinsic connectivity networks for salience processing and executive control." Journal of Neuroscience **27**(9): 2349-2356.
Shanahan, M. (2010). "Metastable chimera states in community-structured oscillator networks." Chaos: An Interdisciplinary Journal of Nonlinear Science **20**(1): 013108.
Shannon, C. E., W. Weaver and A. W. Burks (1951). "The mathematical theory of communication."
Shew, W. L., H. Yang, S. Yu, R. Roy and D. Plenz (2011). "Information capacity and transmission are maximized in balanced cortical networks with neuronal avalanches." Journal of neuroscience **31**(1): 55-63.
Shine, J. M., O. Koyejo and R. A. Poldrack (2016). "Temporal metastates are associated with differential patterns of time-resolved connectivity, network topology, and attention." Proceedings of the National Academy of Sciences **113**(35): 9888-9891.
Siclari, F., J. J. LaRocque, B. R. Postle and G. Tononi (2013). "Assessing sleep consciousness within subjects using a serial awakening paradigm." Frontiers in psychology **4**: 542.
Sizemore, A. E., C. Giusti, A. Kahn, J. M. Vettel, R. F. Betzel and D. S. Bassett (2018). "Cliques and cavities in the human connectome." Journal of computational neuroscience **44**(1): 115-145.
Smallwood, J., K. Brown, B. Baird and J. W. Schooler (2012). "Cooperation between the default mode network and the frontal–parietal network in the production of an internal train of thought." Brain research **1428**: 60-70.
Smith, S. M. (2002). "Fast robust automated brain extraction." Human brain mapping **17**(3): 143-155.
Smith, S. M., M. Jenkinson, M. W. Woolrich, C. F. Beckmann, T. E. Behrens, H. Johansen-Berg, P. R. Bannister, M. De Luca, I. Drobnjak and D. E. Flitney (2004). "Advances in functional and structural MR image analysis and implementation as FSL." Neuroimage **23**: S208-S219.
Spoormaker, V. I., M. S. Schröter, P. M. Gleiser, K. C. Andrade, M. Dresler, R. Wehrle, P. G. Sämann and M. Czisch (2010). "Development of a large-scale functional brain network during human non-rapid eye movement sleep." Journal of Neuroscience **30**(34): 11379-11387.
Sporns, O. (2013). "Network attributes for segregation and integration in the human brain." Current opinion in neurobiology **23**(2): 162-171.

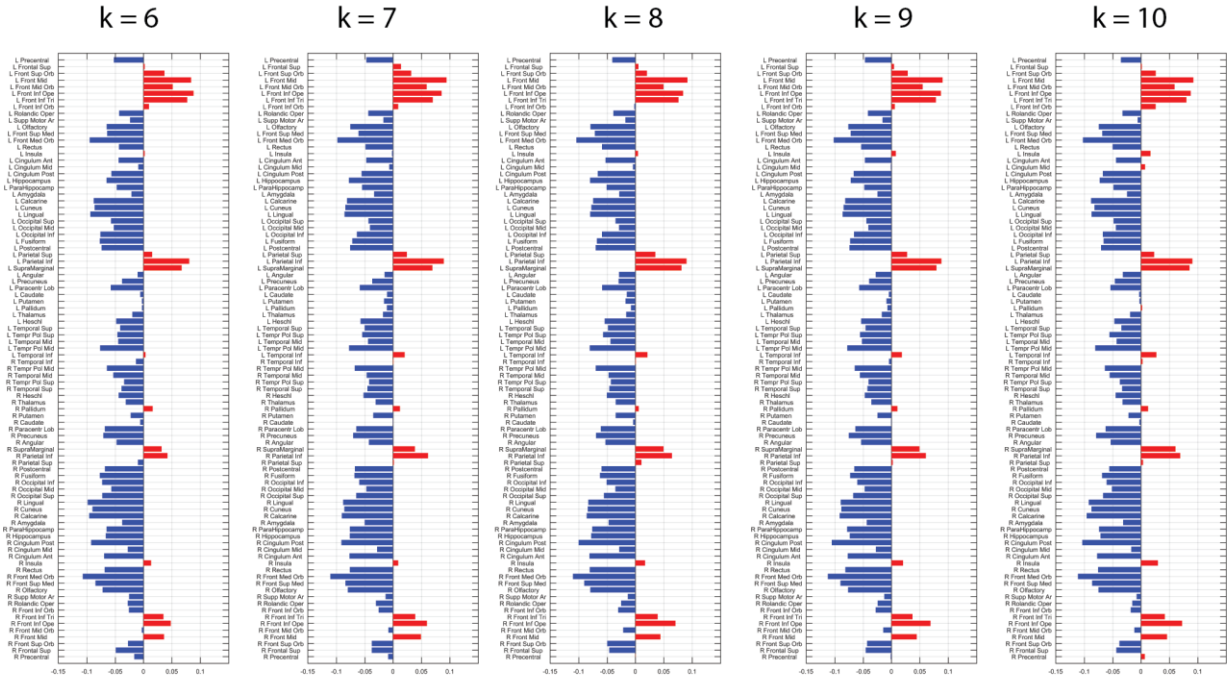
Sporns, O. and R. F. Betzel (2016). "Modular brain networks." Annual review of psychology **67**: 613-640.
Stedman, T. L. (1949). "Stedman's medical dictionary."
Stevner, A. B. (2017). Whole-brain spatiotemporal characteristics of functional connectivity in transitions between wakefulness and sleep. Doctoral Thesis, University of Oxford.
Tagliazucchi, E., M. Behrens and H. Laufs (2013). "Sleep neuroimaging and models of consciousness." Frontiers in psychology **4**: 256.
Tagliazucchi, E., R. Carhart-Harris, R. Leech, D. Nutt and D. R. Chialvo (2014). "Enhanced repertoire of brain dynamical states during the psychedelic experience." Human brain mapping **35**(11): 5442-5456.
Tagliazucchi, E. and D. R. Chialvo (2013). Brain complexity born out of criticality. AIP Conference Proceedings, AIP.
Tagliazucchi, E. and H. Laufs (2014). "Decoding wakefulness levels from typical fMRI resting-state data reveals reliable drifts between wakefulness and sleep." Neuron **82**(3): 695-708.
Tagliazucchi, E., L. Roseman, M. Kaelen, C. Orban, S. D. Muthukumaraswamy, K. Murphy, H. Laufs, R. Leech, J. McGonigle and N. Crossley (2016). "Increased global functional connectivity correlates with LSD-induced ego dissolution." Current Biology **26**(8): 1043-1050.
Tagliazucchi, E., F. Von Wegner, A. Morzelewski, V. Brodbeck, S. Borisov, K. Jahnke and H. Laufs (2013). "Large-scale brain functional modularity is reflected in slow electroencephalographic rhythms across the human non-rapid eye movement sleep cycle." Neuroimage **70**: 327-339.
Tagliazucchi, E., F. von Wegner, A. Morzelewski, V. Brodbeck, K. Jahnke and H. Laufs (2013). "Breakdown of long-range temporal dependence in default mode and attention networks during deep sleep." Proceedings of the National Academy of Sciences **110**(38): 15419-15424.
Tononi, G. (2004). "An information integration theory of consciousness." BMC neuroscience **5**(1): 42.
Tononi, G. and G. M. Edelman (1998). "Consciousness and complexity." science **282**(5395): 1846-1851.
Turkheimer, F. E., R. Leech, P. Expert, L.-D. Lord and A. C. Vernon (2015). "The brain's code and its canonical computational motifs. From sensory cortex to the default mode network: A multi-scale model of brain function in health and disease." Neuroscience & Biobehavioral Reviews **55**: 211-222.
Turton, S., D. Nutt and R. Carhart-Harris (2014). "A qualitative report on the subjective experience of intravenous psilocybin administered in an FMRI environment." Current drug abuse reviews **7**(2): 117-127.
Tzourio-Mazoyer, N., B. Landeau, D. Papathanassiou, F. Crivello, O. Etard, N. Delcroix, B. Mazoyer and M. Joliot (2002). "Automated anatomical labeling of activations in SPM using a macroscopic anatomical parcellation of the MNI MRI single-subject brain." Neuroimage **15**(1): 273-289.
Van Den Heuvel, M. P. and O. Sporns (2011). "Rich-club organization of the human connectome." Journal of Neuroscience **31**(44): 15775-15786.
Varela, F., J.-P. Lachaux, E. Rodriguez and J. Martinerie (2001). "The brainweb: phase synchronization and large-scale integration." Nature reviews neuroscience **2**(4): 229.
Vezoli, J., A. Falchier, B. Jouve, K. Knoblauch, M. Young and H. Kennedy (2004). "Quantitative analysis of connectivity in the visual cortex: extracting function from structure." The Neuroscientist **10**(5): 476-482.
Vidaurre, D., A. J. Quinn, A. P. Baker, D. Dupret, A. Tejero-Cantero and M. W. Woolrich (2016). "Spectrally resolved fast transient brain states in electrophysiological data." Neuroimage **126**: 81-95.
Vincent, J. L., I. Kahn, A. Z. Snyder, M. E. Raichle and R. L. Buckner (2008). "Evidence for a frontoparietal control system revealed by intrinsic functional connectivity." Journal of neurophysiology **100**(6): 3328-3342.
Vollenweider, F. X., M. F. Vollenweider-Scherpenhuyzen, A. Bäbler, H. Vogel and D. Hell (1998). "Psilocybin induces schizophrenia-like psychosis in humans via a serotonin-2 agonist action." Neuroreport **9**(17): 3897-3902.
Watts, D. J. and S. H. Strogatz (1998). "Collective dynamics of 'small-world'networks." Nature **393**(6684): 440.

Xin, F. and X. Lei (2015). "Competition between frontoparietal control and default networks supports social working memory and empathy." Social cognitive and affective neuroscience **10**(8): 1144-1152.
Xue, M., B. V. Atallah and M. Scanziani (2014). "Equalizing excitation–inhibition ratios across visual cortical neurons." Nature **511**(7511): 596.
Yamaguti, Y. and I. Tsuda (2015). "Mathematical modeling for evolution of heterogeneous modules in the brain." Neural Networks **62**: 3-10.
Zalesky, A., A. Fornito, L. Cocchi, L. L. Gollo and M. Breakspear (2014). "Time-resolved resting-state brain networks." Proceedings of the National Academy of Sciences: 201400181.
Zomorodian, A. and G. Carlsson (2005). "Computing persistent homology." Discrete & Computational Geometry **33**(2): 249-274.

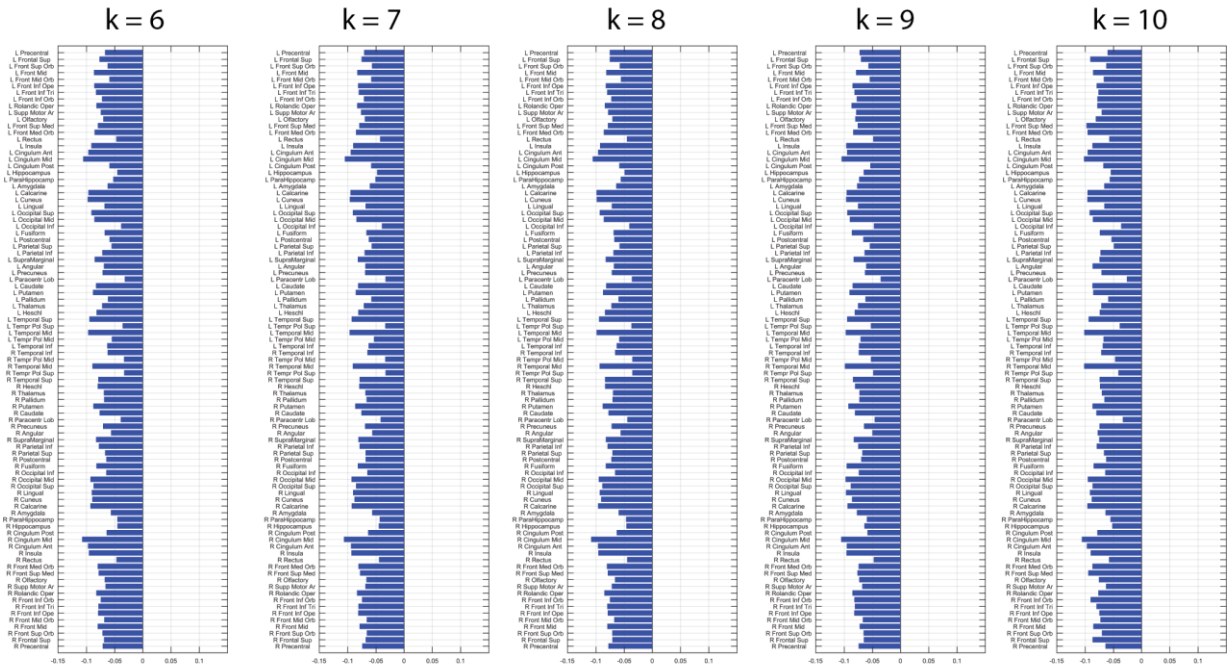
Supplementary Materials



Supplementary Figure 1. *During the filtration process, a cycle will potentially shrink due to the addition of an edge. The evolution of any cycle representative is a combination of two possible situations: i) the cycle shrinks by triadic closure; or ii) the cycle is split into 2 smaller cycles.* Top: *The cycles closes with the addition of triangles where the cycle representative will be the original cycle ⟨abcdef⟩, irrespective of the life time of the sub cycles that are partially closed.* Bottom: *The original cycle is split into smaller cycles that are eventually closed by the mechanism illustrated in the top route. The two cycles that will be represented in the original cycle ⟨abcdef⟩ and the subcycle ⟨abcd⟩, as the cycle ⟨adef⟩ can be obtained as a linear combination of the first two. In our implementation of persistent homology, we choose a representative for a cycle and identify it with the entire lifetime of the cycle. This means that a unique set of edges will represent a cycle, regardless of its possible contraction. This has a direct implication on the scaffolds, and means they are not well-defined. This does not mean they are not informative, but rather that care has to be taken when interpreting the meaning of the particular edges weight forming the scaffolds.*



Supplementary Figure 2. *Bar chart representing contributions of each of the 90 AAL brain areas to the fronto-parietal FC state of interest ($V_c(n)>0$ in red, blue otherwise) across clustering solutions k = 6 through k = 10. In each clustering solution, the probability of occurrence of this state was significantly reduced following the psilocybin injection. The Bonferroni-corrected p-values (i.e. p-val * k) were: 0.022 (k = 6); 0.002 (k = 7); 0.008 (k = 8); 0.026 (k = 9) and 0.019 (k = 10). Regional contributions to the cluster centroid of interest show a high level of consistency across the clustering solutions.*



Supplementary Figure 3. *Bar chart representing contributions of each of the 90 AAL brain areas to the globally coherent state of interest ($V_c(n)>0$ in red, blue otherwise) across clustering solutions k = 6 through k = 10. In each clustering solution, the probability of occurrence of this state was higher following the psilocybin injection, surviving the Bonferroni correction for k = 7 and k = 10. Note that prior to the Bonferroni correction, all the p-values were significant (α = 0.05). The Bonferroni-corrected p-values (i.e. p-val * k) were: 0.13 (k = 6); 0.047 (k = 7); 0.14 (k = 8); 0.10 (k = 9); 0.032 (k = 10). Regional contributions to the cluster centroid of interest show a high level of consistency across the clustering solutions.*

AAL region	Left	Right
Precentral gyrus	1	2
Superior frontal gyrus, dorsolateral	3	4
Superior frontal gyrus, orbital part	5	6
Middle frontal gyrus	7	8
Middle frontal gyrus, orbital part	9	10
Inferior frontal gyrus, opercular part	11	12
Inferior frontal gyrus, triangular part	13	14
Inferior frontal gyrus, orbital part	15	16
Rolandic operculum	17	18
Supplementary motor area	19	20
Olfactory cortex	21	22
Superior frontal gyrus, medial	23	24
Superior frontal gyrus, medial orbital	25	26
Gyrus rectus	27	28
Insula	29	30
Anterior cingulate and paracingulate gyri	31	32
Middle cingulate and paracingulate gyri	33	34
Posterior cingulate gyrus	35	36
Hippocampus	37	38
Parahippocampal gyrus	39	40
Amygdala	41	42
Calcarine fissure	43	44
Cuneus	45	46
Lingual gyrus	47	48
Superior occipital gyrus	49	50
Middle occipital gyrus	51	52
Inferior occipital gyrus	53	54
Fusiform gyrus	55	56
Postcentral gyrus	57	58
Superior parietal gyrus	59	60
Inferior parietal gyri	61	62
Supramarginal gyrus	63	64
Angular gyrus	65	66
Precuneus	67	68

Supplementary Table 1. *Corresponding numerical labels of AAL brain regions used in Figure 2.5 and Figure 5.4.*

	IDI	IDI-stdev		IDI	IDI-stdev
AAL#	Pre/Post Pcb	Pre/Post Psilo	AAL#	Pre/Post Pcb	Pre/Post Psilo
1	0.786	0.432	**46**	0.624	0.009
2	0.624	0.455	**47**	0.439	0.327
3	0.078	0.004	**48**	0.626	0.645
4	0.918	0.121	**49**	0.507	0.036
5	0.577	0.015	**50**	0.406	0.060
6	0.651	0.002	**51**	0.586	0.029
7	0.540	0.007	**52**	0.850	0.658
8	0.453	0.121	**53**	0.509	0.421
9	0.938	0.022	**54**	0.616	0.510
10	0.814	0.369	**55**	0.134	0.835
11	0.936	0.536	**56**	0.696	0.531
12	0.981	0.039	**57**	0.986	0.258
13	0.354	0.071	**58**	0.915	0.378
14	0.926	0.062	**59**	0.292	0.147
15	0.668	0.096	**60**	0.997	0.115
16	0.807	0.000	**61**	0.867	0.064
17	0.848	0.383	**62**	0.515	0.527
18	0.526	0.520	**63**	0.818	0.252
19	0.653	0.075	**64**	0.381	0.310
20	0.796	0.003	**65**	0.391	0.474
21	0.328	0.727	**66**	0.170	0.609
22	0.231	0.004	**67**	0.319	0.463
23	0.648	0.014	**68**	0.592	0.529
24	0.798	0.004	**69**	0.814	0.190
25	0.474	0.350	**70**	0.706	0.235
26	0.996	0.252	**71**	0.464	0.360
27	0.198	0.908	**72**	0.997	0.183
28	0.283	0.267	**73**	0.701	0.050
29	0.673	0.104	**74**	0.998	0.094
30	0.695	0.061	**75**	0.371	0.651
31	0.338	0.009	**76**	0.614	0.038
32	0.926	0.000	**77**	0.681	0.557
33	0.353	0.107	**78**	0.758	0.243
34	0.334	0.038	**79**	0.326	0.521
35	0.785	0.051	**80**	0.384	0.120
36	0.450	0.712	**81**	0.768	0.322
37	0.324	0.839	**82**	0.479	0.024
38	0.093	0.318	**83**	0.267	0.025
39	0.345	0.407	**84**	0.692	0.250
40	0.168	0.530	**85**	0.520	0.231
41	0.086	0.940	**86**	0.598	0.409
42	0.452	0.136	**87**	0.379	0.550
43	0.709	0.592	**88**	0.429	0.711
44	0.655	0.341	**89**	0.729	0.713
45	0.806	0.119	**90**	0.525	0.054

Supplementary Table 2. *The p-values of paired t-tests comparing the IDI and IDI variability of individual brain regions across experimental conditions (pre/post psilocybin & pre/post placebo).*

	IDI	IDI-stdev		IDI	IDI-stdev
AAL#	Awake/N3	Awake/N3	AAL#	Awake/N3	Awake/N3
1	0.001	0.002	**46**	0.002	0.019
2	0.005	0.001	**47**	0.004	0.015
3	0.036	0.000	**48**	0.001	0.002
4	0.026	0.001	**49**	0.006	0.007
5	0.007	0.001	**50**	0.002	0.000
6	0.002	0.017	**51**	0.002	0.002
7	0.006	0.001	**52**	0.001	0.001
8	0.012	0.000	**53**	0.019	0.006
9	0.002	0.000	**54**	0.005	0.023
10	0.002	0.000	**55**	0.010	0.004
11	0.005	0.002	**56**	0.002	0.003
12	0.002	0.001	**57**	0.011	0.017
13	0.005	0.001	**58**	0.011	0.001
14	0.012	0.007	**59**	0.000	0.007
15	0.001	0.002	**60**	0.002	0.002
16	0.002	0.005	**61**	0.003	0.003
17	0.020	0.006	**62**	0.003	0.003
18	0.020	0.002	**63**	0.002	0.004
19	0.001	0.001	**64**	0.001	0.002
20	0.000	0.002	**65**	0.004	0.001
21	0.004	0.001	**66**	0.006	0.011
22	0.002	0.001	**67**	0.002	0.002
23	0.002	0.001	**68**	0.004	0.000
24	0.001	0.002	**69**	0.002	0.001
25	0.001	0.000	**70**	0.008	0.000
26	0.000	0.001	**71**	0.003	0.002
27	0.004	0.007	**72**	0.001	0.000
28	0.002	0.017	**73**	0.031	0.002
29	0.000	0.001	**74**	0.008	0.003
30	0.005	0.004	**75**	0.000	0.006
31	0.015	0.001	**76**	0.007	0.001
32	0.016	0.004	**77**	0.002	0.002
33	0.003	0.002	**78**	0.001	0.002
34	0.037	0.001	**79**	0.001	0.003
35	0.002	0.001	**80**	0.001	0.001
36	0.011	0.001	**81**	0.002	0.000
37	0.007	0.002	**82**	0.005	0.012
38	0.003	0.004	**83**	0.005	0.001
39	0.002	0.001	**84**	0.011	0.000
40	0.001	0.002	**85**	0.003	0.004
41	0.001	0.000	**86**	0.012	0.003
42	0.001	0.002	**87**	0.020	0.002
43	0.000	0.005	**88**	0.006	0.034
44	0.000	0.009	**89**	0.005	0.004
45	0.000	0.019	**90**	0.001	0.007

Supplementary Table 3. *The p-values of paired t-tests comparing the IDI and IDI variability of individual brain regions between N3 sleep and wakefulness.*